Multi-jet Production in High Q^2 Neutral Current Deeply Inelastic Scattering at HERA and Determination of Alpha s

Paul David Prideaux

Ph.D. 2007

Multi-jet Production in High Q^2 Neutral Current Deeply Inelastic Scattering at HERA and Determination of α_s

Thesis submitted in accordance with the requirements of The University of Liverpool for the degree of Doctor in Philosophy.

by

Paul David Prideaux

2007

This thesis is dedicated to the memory of A. Prideaux

"Ecce nunc patiemur philosophantem nobis asinum?" - Apuleius

Contents

List of Figures

Introduction

This document consists of a description of the research carried out by the author between October 2003 and July 2006. It aims to be a self-contained summary of the work undertaken, with attention paid to relevant background information that is essential to understand the purpose and conclusions of this research. This is preceded by a brief, rather philosophical, discussion of the current position of physics today. A full description of the relevant components of the H1 experiment is presented.

Contribution

The author has contributed to this work all data analysis and software implementation required to produce the final results. The author also periodically held responsibility for the running and maintenance of the forward track and forward muon detectors at the H1 experiment where the data used in this research were collected. The author made several contributions to the collection of data by H1 as part of a shift crew. All statements and conclusions are contributed by the author unless otherwise credited.

All results quoted within this thesis have been approved for release by the H1 Collaboration to at least a preliminary standard.

Units

All units quoted in this work use the natural units convention in which $c = \hbar = 1$.

Thanks

The author would like to thank the following people for their part in helping this work through to completion. First, my wife Anna whose constant support helped me immeasurably over the course of this work. The H1 group at the University of Liverpool, but most particularly my supervisor Prof. Tim Greenshaw as well as Prof. John Dainton and Dr. Steve Maxfield for their advice and support. Drs. Andy Mehta, Girish Patel, Paul Laycock and Barry King also provided much illumination on many areas of this work. My student colleagues at H1 were invaluable in helping me get to grips with the research environment and for many useful discussions, so for this I thank Andy Rimmer, Aweys Mohamed, Christian Veelken, Carl Gwilliam, Olĭver Henshaw and AJ Rahmat. This work would simply not be if it were not for the tireless assistance of the hadronic final state and QCD group at H1. Eternal thanks are thus bestowed upon Drs. Dan Traynor, Thomas Kluge and Günter Grindhammer. A special thank-you goes to Dr. Dave Milstead who not only supervised the first year of my work, but pointed me in the direction of QCD research to start with.

I am grateful to the HERA machine group whose outstanding efforts have made and continue to make the H1 experiment possible. I thank the engineers and technicians for their work in constructing and now maintaining the H1 detector, the DESY technical staff for continual assistance, and the DESY directorate for the hospitality which they extend to the non DESY members of the collaboration. I am particularly grateful to the particle physics and astronomy research council (PPARC) for their generous financial support.

Overview

Deeply inelastic lepton-proton scattering (DIS) experiments have been vital to our understanding of the nature of the strong force. This has resulted in Quantum Chromodynamics (QCD) becoming established as the leading theory to describe the strong force in terms of interactions between quarks and gluons that carry different *colour* charges. QCD contains two free parameters, one of which is the strong coupling α_s. The value of this coupling is known to run with the interaction energy scale and so α_s is usually quoted as its value at a scale that is very precisely known - the mass of the Z^0 boson. There are numerous experimental methods for the determination of α_s, for example by the consideration of fragmentation functions or by studying violations of Björken scaling. Furthermore, the production rates of DIS events containing more than one hard (high E_T) jet are directly sensitive to α_s[1]. By measuring the ratio of three and two jet cross-sections ($R_{3/2}$), a value for α_s can be determined[2]. For this method of measuring α_s, precise values for both the inclusive dijet and trijet cross-sections are required. This document presents a measurement of the inclusive dijet and trijet cross-sections, as well as an extraction of α_s from a study of $R_{3/2}$.

The HERA *ep* collider has a centre-of-mass energy $\sqrt{s} \sim 319$ GeV, which allows the study of multi-jet production in DIS over a large region of phase space. The phasespace region specified constrains the analysis to consider only events with high values of virtuality ($Q^2 > 150\text{GeV}^2$) for the exchanged boson. The data are compared to next-to-leading order (NLO) perturbative QCD (pQCD) predictions that are $\mathcal{O}(\alpha_s^2)$ for dijets and $\mathcal{O}(\alpha_s^3)$ for trijets.

Scope

This work makes no claim to truth. Indeed, it appears to the author that modern science does not aim at truth; it does not conceive of truth as possible; it

aims solely at maximum convenience. For example, the idea that the Earth is the immovable centre of the universe can not be contradicted, it merely makes theoretical calculations and predictions more convoluted. Likewise, there are means of describing the physics of the nucleon that are wholly different to QCD, but which require a mathematical structure that is far more complex than that of QCD and are not as broadly applicable. Furthermore, the references to particles in this work are described in terms of the most convenient interpretation, that being, in the language of QCD, quarks and gluons. Such particles are abstract creations of convenience that form just one method of explaining various experimental results and debate as to their physical reality is as invalid as it is fruitless. Indeed, when talking of these objects, the author is reminded of the words of Russell in describing abstract mathematical objects: "nobody knows *what* he is talking about, and it matters to nobody whether he is right or wrong".

Final Words

To students (or anyone else) reading this document, the author's advice for endeavours in research (or anything else) are well summarised by the following words by Coolidge - "Nothing in the world can take the place of persistence. Talent will not; nothing is more common than unsuccessful men with talent. Genius will not; unrewarded genius is almost a proverb. Education will not; the world is full of educated derelicts. Persistence and determination alone are omnipotent."

Jai Guru Deva. Aum.

Chapter 1

The Background

"Und du gehst Rüssel an Schwanz hinterher, trampelpfader hinterman was brauchst du mehr?" - J. Holofernes

This chapter contains the background information required for an understanding of the methods, purpose and historical context of this work. It is a path well trod and there will be no surprises here - there is no new material besides the author's opinions - but it is hoped that these explainations will allow the remainder of this work to be fully understood. There is no doubt in the author's mind that some of today's theoretical problems will one day be understood, but this will likely require innovation as remarkable as that which led to the understanding described in these sections; following in the footsteps of limited successes may be comfortable (and in many cases neccessary) but true progress does not lie therein.

1.1 Physics, Where We Stand

"Daran erkenn' ich den gelehrten Herrn!
Was ihr nicht tastet, steht euch meilenfern,
was ihr nicht fasst, das fehlt euch ganz und gar,
was ihr nicht rechnet, glaubt ihr, sei nicht wahr,
was ihr nicht wägt, hat für euch kein gewicht,
was ihr nicht münzt, das, meint ihr, gelte nicht." - *Goethe*

The first principle of science is classification by measurement. This idea forms the basis of the scientific method, and it enables us to reduce the apparent complexity of the world around us into combinations of relatively few components. This method and its application date back far further than the few hundred years suggested by Feynman[3], to the earliest civilisations of man[1]. The Aristolian[4] idea of four base elements - Earth, Water, Fire and Air - was not a primitive attempt at chemical analysis as often supposed but a method of classifying objects by their properties, both subtle and gross, as determined by investigation (figure 1.1). This procedure is a clear application of scientific method that remains valid today. However, it must be noted that the principle of measurement is not the final word of science. Measurements of a single phenomenon can yield different results under the same conditions, such as the emission of radiation from a nucleus, where only a *statistical* description is possible. This is not due to experimental limitations but, according to our current understanding, a *fundamental* restrictive property of the universe. Similarly, it is also believed that the act of measurement irrevocably alters the state of that which is being observed. The wave and particle-like behaviour of the electron is an example of quite contradictory measurements of the same object. Measurements of length, mass and duration are entirely dependent on the inertial reference frame of the observer. Other phenomena, such as the

[1] A study of the complete works of Feynman indicates that he was aware of this, but chose not to mention it in his famous public lectures.

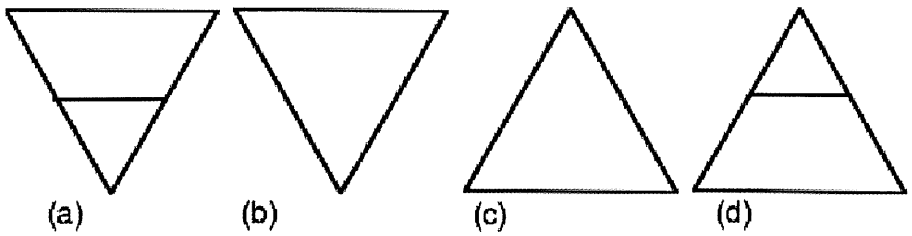

Figure 1.1: *Symbolic representation of principle elements (a) Earth (b) Water (c) Fire and (d) Air. Rather than primitive chemistry these elements were groups into which phenomena were classified and are thus the precursor of the modern scientific method.*

internal properties of the nucleon, can not be measured directly, but only inferred. Many properties of matter, particularly pertaining to surfaces, are in many ways entirely arbitrary.

The phenomena of the universe in which we live can be observationally divided into two groups, those of *Force* and *Form*. This idea of Greek classicism is, perhaps surprisingly, apt in the territory of physics today. The particles of Form are known as *fermions* and are described by the mathematics of Fermi-Dirac statistics. These particles are distinguished as those with half integer intrinsic angular momentum (in units of $\hbar$), known as *spin*[2]. Everyday matter is composed of protons, neutrons and electrons, all of which are fermions. However, any interaction of these particles, including their binding together to form atoms, requires the intervention of *forces*. The most popular theories at the time of writing describe forces in terms of the exchange of force mediating particles. These are known as *bosons* as their collective properties are described by a branch of mathematics known as Bose-Einstein statistics. Bosons are distinguished as those particles with integer unit of intrinsic spin angular momentum. As separate as these concepts may appear, both Force and Form are merely manifestations of the concept of *energy*.

[2]For an introduction to the basics of quantum mechanics see [5].

Force	Mediated by	Example Coupling	Relative Strength
Strong Nuclear	Gluon	Mesons to baryons	~ 1
Electromagnetic	Photon	All electric charges	$\sim 10^{-2}$
Weak Nuclear	$W^{\pm}$, Z^0	Beta decay	$\sim 10^{-5}$
Gravitational	Graviton (?)	All energy	$\sim 10^{-40}$

Table 1.1: *The four known forces and their mediating bosons. An example coupling involving each force is given along with the relative strength of each coupling, normalised to the strong interaction.*

Modern physics is currently based on the postulate that there are four fundamental forces that allow different arrangements of energy to interact with each other; the so-called *strong* nuclear interaction, the gravitational interaction, the so-called *weak* nuclear interaction and the electromagnetic interaction (see table 1.1). These forces are well understood within current experimental limits.

The research documented within this work deals with a category of experiment where information is gathered by studying the effects of scattering particles off each other. This is in an attempt to shed further light upon a particular area of physics known as Quantum Chromodynamics (QCD), which is concerned with describing the strong nuclear interactions that primarily concern the nucleon and its constituents. The following sections deal with scattering experiments and from this progress into an overview of QCD. These sections have been heavily influenced by the works referenced in [5, 9, 10, 11, 14, 15, 16, 21, 24, 25] and no new material, besides the authors opinions, is presented therein.

1.2 Particle Scattering

"It is by studying little things that we attain the great arts" - Samuel Johnson

The theoretical and experimental grounding of scattering experiments has a rich history, mostly based on the pioneering work of Rutherford, Geiger and Marsden. The ideas proposed nearly one-hundred years ago to explain the results of scattering experiments have had to be little changed to deal with modern scattering experiments. This section gives an overview of the foundation of deeply inelastic *ep* scattering, the process with which this work is concerned.

1.2.1 Elastic Scattering of Point Particles

The Rutherford scattering formula gives the cross-section for elastic scattering of two charged, spinless, point-like particles, due to their electromagnetic interaction:

$$(\frac{d\sigma}{d\Omega})_{Rutherford} = \frac{(Z\alpha)^2 E^2}{4p^4 \sin^4(\frac{\theta}{2})}, \tag{1.1}$$

where Z is the target charge, p and E are the incident momentum and energy, θ is the scattering angle and α is the electromagnetic fine structure constant. The target is assumed to be infinitely massive so there is no recoil. This equation provided excellent agreement with the data collected by Rutherford, Geiger and Marsden (see figure 1.2) for the scattering of alpha particles on gold nuclei. The momentum transfers involved in Rutherford's experiment were small enough for the substructure of the target nucleus to remain unprobed.

1.2.2 Elastic Scattering of More General Particles

For high energy *ep* scattering, this formula must be adjusted on account of the following considerations:

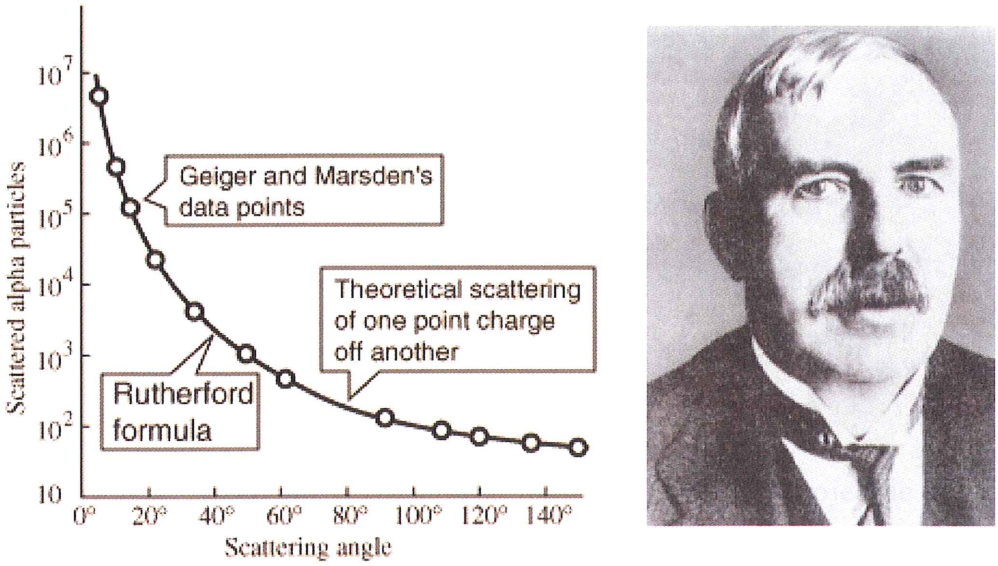

Figure 1.2: *(Left) Rutherford's results for scattering alpha particles on gold nuculei. (Right) Ernest Rutherford.*

- The particles involved are not spinless.
- The magnetic moment of the proton contributes to the cross-section.
- The proton does recoil in the interaction.
- The proton is not a point charge but has a charge distribution.

The cross-section for the point charge can be extended by inclusion of a form factor $F(\mathbf{q})$ such that

$$(\frac{d\sigma}{d\Omega}) = (\frac{d\sigma}{d\Omega})_{point}|F(\mathbf{q})|^2 \quad , \tag{1.2}$$

where $\mathbf{q} = (\mathbf{p_i} - \mathbf{p_f})$ and is the momentum transfer from the projectile to the target. The initial and final momentum of the projectile are denoted i and f respectively. For elastic scattering the form factor is the Fourier transform of the spatial charge distribution such that

$$F(\mathbf{q}) = \int \rho(\mathbf{x}) e^{i(\mathbf{q}\cdot\mathbf{x})} d^3x \quad . \tag{1.3}$$

In total, the elastic scattering cross-section can be written

$$(\frac{d\sigma}{d\Omega})_{lab} = \frac{\alpha^2}{4E^2 sin^4(\frac{\theta}{2})} \frac{E'}{E} [\frac{G_E^2 + \tau G_m^2}{1+\tau} \cos^2(\frac{\theta}{2}) + 2\tau G_m^2 sin^2(\frac{\theta}{2})] \tag{1.4}$$

where $\tau = -(\frac{q^2}{4m^2})$, m is the proton mass and E' is the projectile energy after scattering. G_E and G_m are form factors related to the charge and magnetic moments of the proton, but are not simply the Fourier transforms of these distributions due to the recoil of the target proton. They are instead functions of q^2.

1.2.3 Deeply Inelastic Scattering

Elastic *ep* scattering experiments showed that the proton was not pointlike. It is to be expected that, for scattering experiments with sufficient momentum transfer, the substructure of this particle can be resolved. The constituents of the proton were initially named *partons* and such taxonomy will suffice for the present time; a discussion of the nature of partons is presented in the following section. Neutral current deeply inelastic scattering (NC DIS) is the name given to the *ep* collision process where the incident electron[1] emits a high energy vector boson (either a γ or Z^0) that interacts with a parton within the target proton, causing the proton to *disintegrate* (figure 1.3). An *ep* collision is typically considered to be a DIS event where $-q^2 > 1$ GeV^2 as in this region the virtual photon is of sufficiently small wavelength to resolve sub-structure within the proton[17].

The kinematics for a NC DIS event may be completely specified by any two

[1]In this document, *electron* refers to either an electron or a positron.

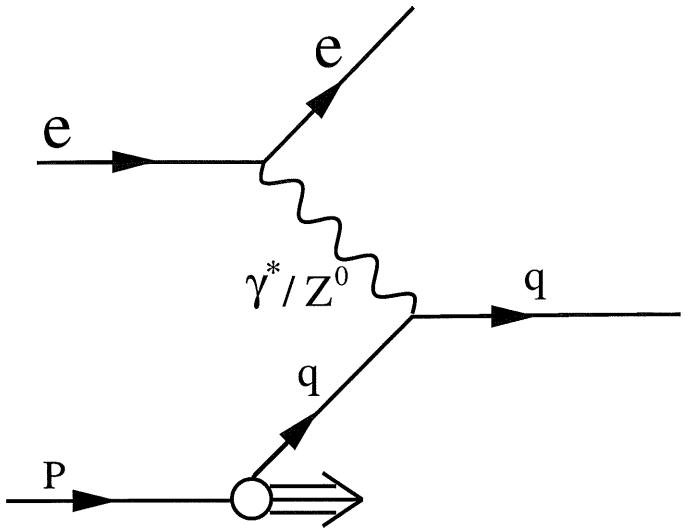

Figure 1.3: *Feynman diagram showing tree-level neutral current DIS.*

of a range of kinematic variables[9, 10]. The simplest DIS event is illustrated in figure 1.3. The incident electron has a four-momentum k^μ and the target proton has a four-momentum P^μ given by:

$$k^\mu = (E_e, \mathbf{p_e}) \quad , \quad P^\mu = (E_p, \mathbf{p_p}) \tag{1.5}$$

where E and $\mathbf{p}$ represent energy and momentum respectively. The four-momentum of the scattered electron is given by:

$$k'^\mu = (E'_e, \mathbf{p'_e}) \tag{1.6}$$

We define the four momentum transfer Q^2, the Björken scaling variable x_{Bj} and the inelasticity y as:

$$Q^2 = -q^2 = -(k^\mu - k'^\mu)^2 \quad , \tag{1.7}$$

$$x_{Bj} = \frac{Q^2}{2P^\mu q_\mu} \quad \text{and} \tag{1.8}$$

$$y = \frac{P^\mu q_\mu}{P^\mu k_\mu} \quad . \tag{1.9}$$

In the limit $\mathbf{p_p} \to \infty$, the variable x_{Bj} corresponds to the fraction of the proton momentum carried by the struck parton. The centre-of-mass energy $\sqrt{s}$ is related to these variables[2] by the equation $Q^2 = sxy$. The wavelength of the exchanged photon is inversely proportional to Q^2 indicating that, as Q^2 increases, smaller structures within the proton are resolved. The relationship between Q^2 and λ is given by $Q = \frac{0.2 \text{ GeV fm}}{\lambda}$.

The cross-section for neutral current DIS can be considered to be composed of a Born cross-section and factors acounting for the effects of QED and weak radiative corrections. These factors will be considered later in this section. The double differential Born cross-sections is:

$$\frac{d^2\sigma_{NC}}{dx_{Bj}dQ^2} = \frac{2\pi\alpha^2}{x_{Bj}Q^4}[Y_+F_2(x_{Bj},Q^2) - Y_-x_{Bj}F_3(x_{Bj},Q^2) - y^2F_L(x_{Bj},Q^2)] \quad , \tag{1.10}$$

where $Y_\pm = 1 \pm (1-y)^2$ and describes the helicity dependences of the electroweak interactions. The structure function F_3 only contains contributions from Z^0 exchange and γ/Z^0 interference and is sensitive to the valence quarks within the proton. For $x_{Bj} < 0.3$ and where $Q^2 < M_Z^2$ these contributions can be considered negligible such that $F_3 \sim 0$ and F_2 is reduced to the electromagnetic structure function. F_2 and F_L are form factors relating to the *transverse* and *longitudinal* polarisation states of the exchanged virtual photon. It is worth noting that a virtual photon may have longitudinal polarisation.

The Rutherford scattering formula (equation 1.1) for the scattering of point-like objects contains no dependence on terms with units of length and so the cross-section *scales* with increasing momentum transfer. Assuming that the

[2]Neglecting electron and proton masses.

virtual photon in a DIS interaction scatters from a point-like object within the proton, it is reasonable to expect similar behaviour for the DIS cross-section. This scale invariance in DIS is known as *Björken Scaling* and was observed in early DIS results from experiments at SLAC[18]. Whilst the breaking of this theoretical scale invariance at low values of x_{Bj} was instrumental in the understanding of the constitution of the proton, the effect is small compared with the *strong* Q^2 dependence of the elastic form factor for *ep* scattering. The *breaking* of scaling occurs at low values of x_{Bj} and must be due to constituents of the proton that introduce additional terms to the structure functions that do not scale such that the overall function no longer scales.

By considering the ratio of the form factors from neutrino- and electron- nucleon scattering, the charge of the point-like scattering centres can be determined. For high values of x_{Bj}, the charges of the scattering centres of the proton are found to be $\frac{2}{3}e$ and $-\frac{1}{3}e$. The spin of these partons has been assumed to be $\frac{1}{2}$ for the description given above. Defining a further structure function $F_1(x_{Bj}) = \frac{F_2(x_{Bj})-F_L(x_{Bj})}{2x_{Bj}}$ we may consider the Callan-Gross relationship[19] $2x_{Bj}F_1(x_{Bj}) = F_2(x_{Bj})$. This relationship has been verified by experiment for values of x_{Bj} greater than about 0.3[20] and confirms that the objects considered are indeed spin $\frac{1}{2}$[3].

It is theorised and proven experimentally that the proton is composed of fractionally charged, spin $\frac{1}{2}$, hard scattering centres that behave as pointlike Dirac particles, with some other, uncharged, constituent that allows for the violation of scaling. These components will be explored in the following section.

1.2.4 QED Radiation

The process of deep-inelastic *ep* scattering is also effected by the emission of real and virtual photons from both the incident and the outgoing electron and

[3]The relationship for spin 0 particles would be $\frac{2x_{Bj}F_1}{F_2} = 0$.

the quarks involved in the interaction. The largest effect on the scattering cross-section is the contribution from real photon emission from the electron. A real photon radiated by the final state electron is likely to result in the electron and photon being reconstructed as a single object and so the effect will be inseparable. The radiated photon may also convert to an e^+e^- pair in the material of the detector (see appendix E, figure E.7). Very hard final state radiation may have the effect of altering the apparent value of Q^2 as reconstructed from the other event kinematics. The transverse momentum of the scattered electron may also be reduced. Real photons radiated from the initial state electron will alter the centre-of-mass energy of the ep collision and so alter the kinematics of the event. This effect may be large in some regions of phase space. It is expected that hard collinear photons tend to be radiated at large values of inelasticity, y. Similarly, soft photon radiation tends to prefer small values of y[15]. The QED corrections associated with the quarks in the interaction are considered to be less important as they do not lead to the mismeasurement of Q^2 when using the electron method of reconstructing the event kinematics (see appendix D).

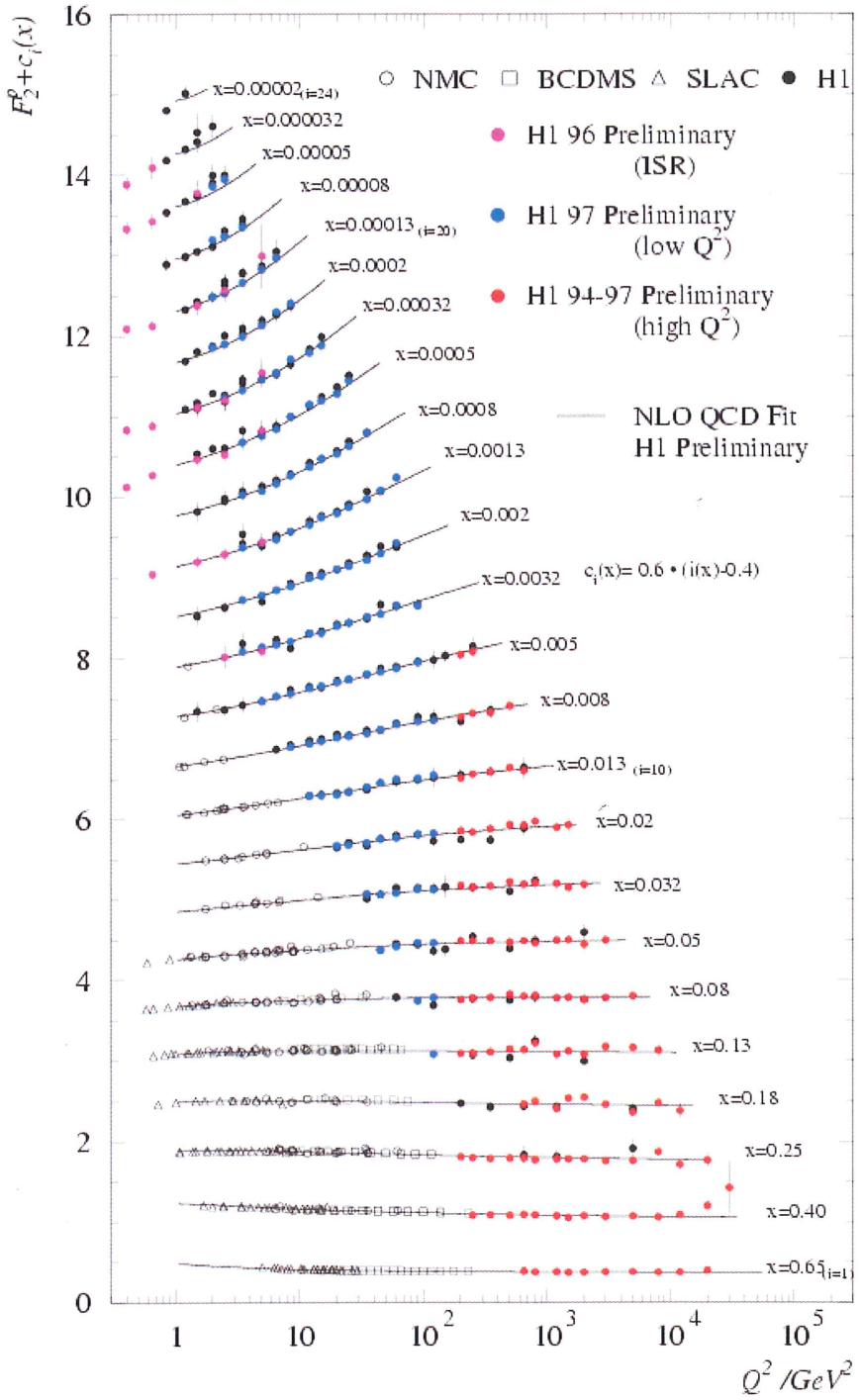

Figure 1.4: *The proton structure function F_2 as determined from data taken by the H1 Collaboration and from fixed target experiments. Data are compared to a next-to-leading order QCD fit. The function $c_i(x)$ is defined in the plot and is used for improved visibility of the distributions. In this plot, x refers to the Björken scaling variable x_{Bj}.*

1.3 Quantum Chromodynamics (QCD)

"Ex nihilo, nihil fit." - A. Crowley

1.3.1 Quarks, Gluons and Colour

As indicated in the previous section, it has been experimentally determined that the nucleon has a substructure. The questions that then confronted physics were, what were these constituent particles and how can their interactions be described? The huge success of gauge theory in describing the electromagnetic interaction encouraged physicists to search for a similar theory for strong interactions. Quantum Chromodynamics is widely acknowledged as being the correct theory of strong interactions[1]. This places a large importance on QCD and the continuation of precision experimental tests of the theory. The degrees of freedom within QCD are thought to represent quarks and gluons (collectively known as *partons*), and there is much experimental evidence to support this idea. There are many similarities between QCD and QED, but also many differences. The QCD equivalent of the electric charge is the *colour* charge. As in QED, the force between objects with this charge is due to the exchange of a spin 1, massless boson - photons[2] in QED, *gluons* in QCD. However, whilst the photon is neutral, the QCD quanta are charged. Also QCD contains three colours and three anti-colours as opposed to the simpler arrangement of positive and negative charges in QED. The gauge group of QCD is the non-abelian SU(3) group.

The concept of a property, now known as *colour*, possessed by quarks was first introduced by Greenberg[22] in an effort to explain the seemingly anomalous breaking of the spin-statistics theorem for some members of the $J^P = \frac{3}{2}^+$ decu-

[1] Correct, in the sense of a low-energy effective theory which is the scope of all physics at the time of writing.

[2] The word photon is derived from *Phaeton* who was the charioteer of the Sun in ancient greek theology.

plet. Two states of this decuplet (the Δ^{++} and the Ω^{--}) are composed of three identicle quarks and the corresponding wave function is entirely symmetrical. On the surface, this appears to contradict the famed Pauli exclusion principle but Greenberg's idea was that there exist hidden degrees of freedom that allowed the quarks to be distinguished and thus the overall wavefunction to be asymmetric. This degree of freedom was called colour and it was proposed that although there should exist three colours, real particles must always be colour singlets in that they contain all three colours or colour-anticolour combinations such that they are colourless. This proposal was popular because it also allowed the experimental results relating to the ratio of the cross-sections for hadron production and muon pair production in e^+e^- collisions to be explained. This property was soon developed into a full theory for the interactions of quarks.

Each colour charge is given the name of an optical colour, although these convenient labels must never be confused with actual colours. These names are *red* (r), *blue* (b) and *green* (g). The eight gluons are made of the following combinations: $r\bar{b}$, $b\bar{r}$, $r\bar{g}$, $b\bar{g}$, $\bar{r}g$, $\bar{b}g$ as well as two orthogonal, antisymmetric octet states $\frac{1}{\sqrt{2}}(b\bar{b}-r\bar{r})$ and $\frac{1}{\sqrt{6}}(r\bar{r}+b\bar{b}-2g\bar{g})$. The singlet $\frac{1}{\sqrt{3}}(r\bar{r}+b\bar{b}+g\bar{g})$ has no colour and does not contribute to the colour force. These colours interact in ways familiar from QED - like colours repel while colour and anticolour attract - and unfamiliar ones, where different colours attract if the quantum state is antisymmetric and repel if the state is symmetric under the exchange of quarks. Considering the three possible pairs red-green, green-blue and blue-red, a third quark will be attracted if its colour is different and if the final quantum state is antisymmetric under pair exchange. This leads to baryons of the form red-green-blue. A further quark will then be repelled by one and attracted by two of the quarks, but only in the antisymmetric combinations, which reduces the attractive force by a factor of two such that the overall force is zero. The hadrons are colourless, but are affected by the strong force due to their coloured constituent particles. This leads to the physics of the nucleus

and the entire field of nuclear physics is devoted to its study; further study of this area is beyond the scope of this work.

1.3.2 QCD Lagrangian

QCD is a non-abelian Yang-Mills gauge theory that describes the interactions of a triplet of spin $\frac{1}{2}$, coloured quarks via an octet of vector gluons. The Lagrangian for QCD is given by

$$\mathcal{L} = -\frac{1}{4}F^{\alpha}_{\mu\nu}F^{\mu\nu}_{\alpha} - \sum_k \bar{q}_k\gamma^{\mu}[\delta_{\mu} - igA^{\alpha}_{\mu}t_{\alpha}]q_k - \sum_k [m_k\bar{q}_k q_k] + \mathcal{L}_{g.f.} \quad , \qquad (1.11)$$

where $F^{\alpha}_{\mu\nu}$ is the field strength tensor derived from the gluon field A^{α}_{μ} such that $F^{\alpha}_{\mu\nu} = \partial_{\mu}A^{\alpha}_{\nu} - \partial_{\nu}A^{\alpha}_{\mu} + gC^{\alpha}_{\beta\gamma}A^{\beta}_{\mu}A^{\gamma}_{\nu}$ here $C^{\alpha}_{\beta\gamma}$ are the structure constants of SU(3), g is the bare coupling of the theory and α, β and γ run over the eight colour degrees of freedom of the gluon field. The quantities m_k are the bare masses of the quark fields and the quark fields q_k are in the triplet representation of the SU(3) group. The t are the Gell-Mann matrices and satisfy $[t_{\beta}, t_{\gamma}] = iC^{\alpha}_{\beta\gamma}t_{\alpha}$[13]. As for QED, it is required to add a gauge fixing term $\mathcal{L}_{g.f.}$ in order to derive a propagator for the gauge bosons. Gauge fixing is not dealt with further in this work. The so-called *Feynman Rules* for QCD can be calculated from the Lagrangian and can be found in many reference works, for example [9].

Thus, QCD is a non-abelian gauge theory with the gauge group SU(3). The degrees of freedom associated with the quark field are the quantum numbers of *colour* and the eight gauge bosons that are required to preserve local gauge invariance are the gluons. It is not strictly true to state that the strong coupling is the only free parameter of QCD. The most general Lagrangian also includes a CP violating term that introduces a parameter θ_{QCD}. However, experimental results, such as measurements of the neutron electric dipole moment, indicate

that $\theta_{QCD} < 10^{-9}$ and it is common to state that this parameter is simply zero. It is essential to understand why a free parameter should be (nearly) zero but this question remains unsolved and is referred to as the *strong CP problem.* Further discussion of this topic is beyond the scope of this work.

1.3.3 Infrared Safety

Low momentum (*soft*) and collinear gluon emissions in QCD lead to divergences in perturbative attempts to calculate cross-sections. There are divergences when two final state partons become collinear and when a final state gluon becomes soft. There are also divergences when several final state partons become collinear to each other. However, the picture is (thankfully!) not hopeless. By dividing the contributions to the scattering cross-section into short-time and long-time effects[3], some control can be regained. Perturbation theory is of little or no value for long-time physics so, in order to test perturbative QCD, it is important that we examine observables that do not depend on long-time effects. The total scattering cross-section is one example of such an observable. Observables where there is no sensitivity to long-time physics are known as *infrared safe.* This can be defined as the case where an observable with an n-parton configuration has the same value as a corresponding $(n+1)$-parton configuration where the energy of the additional parton tends to zero. An observable is safe from collinear divergences if a pair of collinear particles can be combined into a single particle (carrying the combined momentum) without changing the value of the observable.

1.3.4 Factorisation

Contributions from partonic interactions on the scale of a hadron are considered to be non-perturbative and are factorised into the so-called *parton density functions*, which give the probability density of finding a given parton within a

[3]That is, phenomena occuring a short or long time after the initial interaction.

hadron carrying a fraction x_{Bj} of that hadron's longitudinal momentum. The parton density function must be determined by experiment. Any cross-section that contains partons in the initial state must be given by the product of the parton density function (integrated over all x_{Bj} for all partons considered) and the parton level cross-section. Higher order corrections must be considered that include gluon emissions from the "struck" parton prior to the interaction with the virtual photon. These corrections must be integrated over all transverse momenta of the gluons (relative to the initial parton). As this radiation becomes soft, this integral becomes divergent. These collinear divergences can be extracted as factors which can be included in a redefinition of the parton density function. This introduces a factorisation scale μ_f below which gluon emissions are considered to be part of the hadron and are thus considered as part of a redefined parton density function, which is a function of μ_f. The parton density function now depends on the choice of factorisation scale.

1.3.5 Renormalization

It has been said that short-time physics is both ugly and beautiful - the former due to the difficulties posed for theoretical calculations by the myriad infinities that occur, the latter due to the fundamental physics that is undoubtably hidden therein. It is highly unlikely that experimental facilities will ever have sufficient time resolution to explore this region. In order to deal with the infinities, a process known as *renormalization* is employed. This section attempts to give an overview of what renormalization is and what some of the theoretical consequences of using such a method are.

For any interaction, one can consider perturbative corrections to the interaction vertices and propagating particles. For events that occur on time scales smaller than $\sim \frac{1}{\sqrt{s}}$ (where $\sqrt{s}$ is the centre of mass energy), the loop integrals for these processes make large contributions. The exchanged virtual boson propagates for a time $\sim \frac{1}{\sqrt{s}}$ and the virtual fluctuations under consideration

here occur over a period $\Delta t \ll \frac{1}{\sqrt{s}}$. In order to produce theoretical calculations that consider the effect of fluctuations up to some perturbative order, an arbitrary ultraviolet cutoff $M \gg \sqrt{s}$ is introduced. This allows the calculation of effects from fluctuations where $\frac{1}{M} < \Delta t$. There are different methods of performing this renormalization process, all of which have the effect of introducing of an arbitrary - but characteristic - scale parameter. It is common to use the $\overline{MS}$ scheme[4]. This work will follow this convention, and thus we must introduce an $\overline{MS}$ renormalization scale μ. This scale can be thought of in such a way that the effects of physics at times $\Delta t \ll \frac{1}{\mu}$ are removed from the theoretical calculations of pQCD. These effects are not simply ignored, but are accounted for by the adjustment of the coupling such that its value now has some dependence on the choice of scale such that $\alpha_s \to \alpha_s(\mu)$.

It is worth reassuring the reader at this point that the procedure described above is nothing more than a cover for our ignorance of the behaviour of matter at high energy (short time duration or distance). The cutoff mass M simply accounts for some unknown modification to Quantum Field Theory at this energy, for example if the quarks involved have some substructure, or the effect of some other unexpected new physics. Dirac[26] suggested that accepting a theory that predicts a known finite quantity as infinite is a delusion and whilst the method is functional for now, a fundamental change in ideas is required.

Aside - The Proton as a Fractal?

Self similarity occurs in many aspects of nature, from branch patterns in trees and blood vessels to galaxies and the large scale structure of the universe itself. An object can be said to possess self similarity if its composition or general form appears the same, regardless of scale, when any small section is viewed in isolation (perhaps up to or within predefined limits). The expected emission

[4]Modified minimal-subtraction.

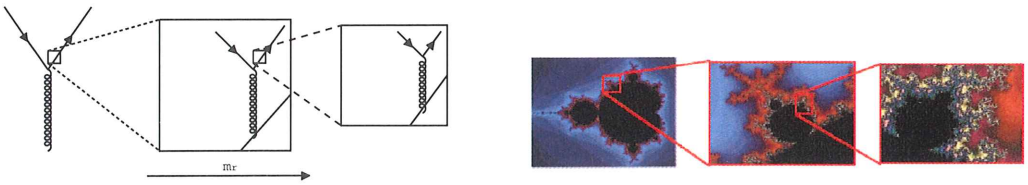

Figure 1.5: *The proton can be thought of as possessing a fractal structure. Compare an expected QCD radiation pattern (left) and the self-similar geometry of a common generated fractal (right).*

pattern of QCD radiation is such that the structure of a hadron can be considered to have some degree of self similarity. This is supported qualitatively by experiment, where increasing resolution yields ever more complex structure thought to be due to a continuum of increasingly low x_{Bj} partons, which can be compared against a generated geometric self similar object that is infinite in structure (see figure 1.5). This idea has been parameterised mathematically in [28] resulting in an expression for the proton structure function $F_2(x_{Bj}, Q^2)$ that provides an excellent fit to recent low x_{Bj} HERA data, with a small number of parameters. A full description of self similarity is beyond the scope of this work but an excellent introduction to the subject is available in [27].

1.3.6 Running Coupling

A physical interpretation of the running coupling can be seen by considering one of the similarities of QCD with QED - the effect known as *charge screening.* However, one of the main differences between QED and QCD - that is, that the exchanged bosons are themselves charged - has an effect on the way the "charge screening" functions. An overview of charge screening in QED is given in appendix C. QCD also features screening effects but due to the interaction of gluons with each other and because gluons carry away colour from the quark (both effects due to their coloured status) the higher-order effects contain additional loops. This has the effect that, as an incident probe penetrates closer to the "bare" charge, it sees ever decreasing amounts of colour and so

the measured colour charge decreases. As in QED, this is well described by a running coupling; in this case $\alpha_s(Q^2)$.

However, the purpose of renormalization was to account for the effects of physics that occurs on time scales $\Delta t \ll \frac{1}{\mu}$. This brings us now to the differential equation that describes the μ dependence of $\alpha_s(\mu)$, known as the *renormalization group equation.* A full account of this equation can be found in [25].

$$\frac{d}{d\log(\mu^2)}\frac{\alpha_s(\mu)}{\pi} = \beta(\alpha_s(\mu)) = -\beta_0(\frac{\alpha_s(\mu)}{\pi})^2 - \beta_1(\frac{\alpha_s(\mu)}{\pi})^3 + ... \qquad (1.12)$$

The beta function is calculated perturbatively, with the first coefficients being given by

$$\beta_0 = \frac{(33-2N_f)}{12} \quad and \quad \beta_1 = \frac{(306-38N_f)}{12} \quad , \qquad (1.13)$$

where N_f is the number of quark flavours[29]. The kinematic region of this work falls entirely above the production theshold for the b quark and below that of the t quark, thus N_f is taken to be five throughout. The coefficients β_0 and β_1 are scheme independent. The next two coefficients are available for the $\overline{MS}$ scheme and can be found in [30]. The effect of physics at very small time intervals, for example at the GUT scale, can not reasonably be known. Thus, the treatment outlined here accounts for short duration physics such that $\frac{1}{M} < \Delta t < \frac{1}{\mu}$. The boundary condition for the renormalization group equation is then given by the value of α_s at $\mu_0 \approx M$,

$$\alpha_s(\mu) = \frac{\alpha_s(M)}{1 + \frac{\beta_0}{\pi}\alpha_s(M)\log(\frac{\mu^2}{M^2})} \qquad (1.14)$$

to first order in β. This differs from the similar expression from QED in

a few ways, but crucially in the opposite sign (in this case, positive) in the denominator. This means that so long as there are fewer than sixteen quark flavours - and there are strong experimental and theoretical reasons to believe that this is so - the screening effect will be opposite to that in QED, such that the strong charge will decrease as μ increases. It is convenient to use a different, but equivalent, parameter in place of M. This is chosen to be the experimentally determined value of the mass of the Z^0 boson, M_Z. The version of the equation used for the remainder of this work is, to second order in β,

$$\alpha_s(\mu) = \frac{\alpha_s(M_Z)}{1 + \frac{\alpha_s(M_Z)}{\pi}(\beta_0 \log(\frac{\mu^2}{M_Z^2}) + \frac{\beta_1}{\beta_0}\log(\frac{\alpha_s(M_Z)}{\alpha_s(\mu)}))} \quad . \tag{1.15}$$

It has been shown[6] that, for the $\overline{MS}$ scheme, the difference between using the four term and the two term approximation for β is negligible. The two term approximation given above is used for the theory calculations within this work. In order to avoid confusion between the renormalization scale and the factorisation scale, the renormalization scale will from here on be denotated μ_r.

1.3.7 Towards Jets

It has been shown in the previous sections that QCD is a Quantum Field Theory (QFT) with two unique features, these being related to the effect of the interaction energy scale on the coupling. In the high energy limit, where the strong coupling tends to zero, quarks and gluons can be considered to be free particles. This is known as *asymptotic freedom.* In the low energy limit, where the strong coupling approaches infinity, the quarks and gluons are confined. This is known as *infrared slavery.* Asymptotic freedom holds in cases where two quarks can be thought of as coming into very close contact (or a *hard* interaction) and in this sort of event the strong coupling is relatively weak and perturbation theory may be used reliably. At lower values of momentum transfer, the approximations inherent in perturbation theory are no longer

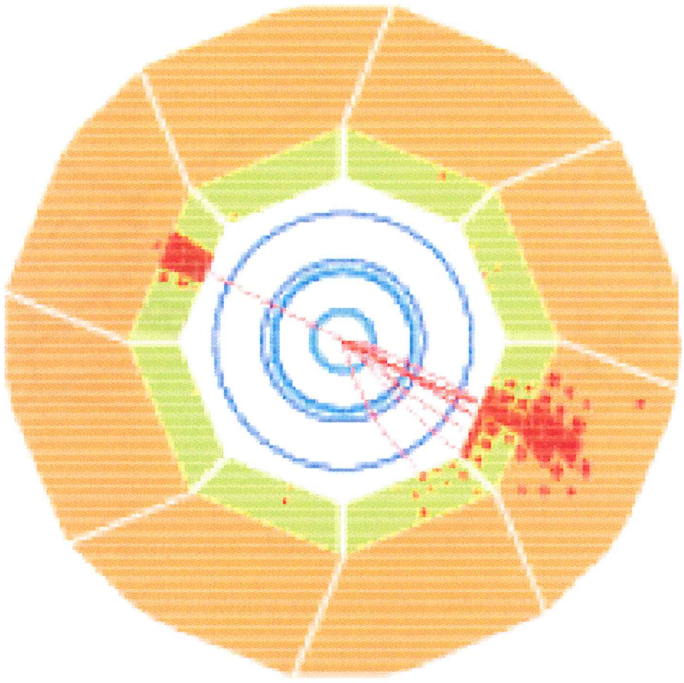

Figure 1.6: *r-ϕ view of the H1 detector showing a single jet event.*

mathematically justified[5]. Absolute quark confinement may not be an intrinsic feature of QCD - the possibility of one day observing a free quark is not ruled out. At short distances, the force between two quarks is approximately described by an inverse square law. At larger distances the potential energy between two quarks increases as they are separated in a way similar to that of a stretched elastic cord. It is postulated that when the energy stored in this "cord" is large enough to produce a quark-antiquark pair, the "cord" will break with one of this new pair at either side. Thus, as quarks are pulled apart, they appear to generate additional quark-antiquark pairs. It is also assumed that gluons behave in a similar way. This is the basic picture behind the process of *hadronization*, which is not fully understood, whereby an initial

[5]The boundary between what is calculable in perturbation theory and what is not is poorly defined. Some hadronization models appear to employ regions of phase space that are arguably non-perturbative. Agreement with data allows this to continue, but the distrinction between pQCD and non-pQCD ought to be made explicit.

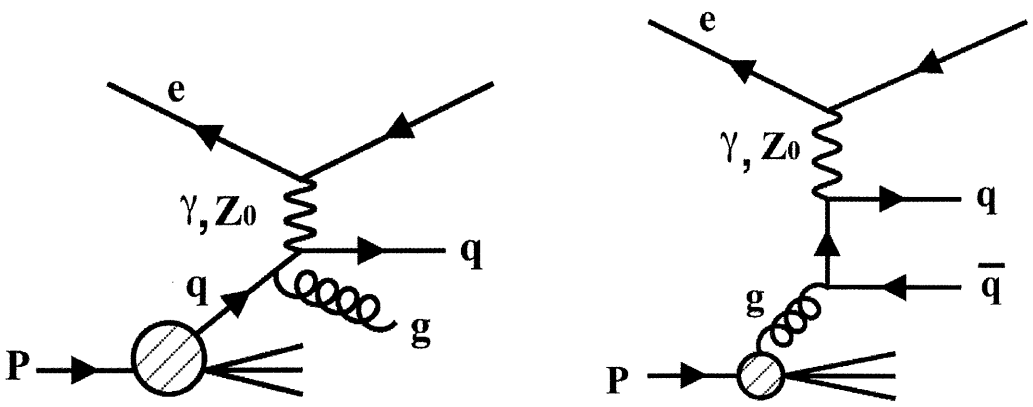

Figure 1.7: *Feynman diagrams showing LO QCD-Compton (left) and boson-gluon fusion (right) DIS processes for dijets. The diagrams show interactions between a proton and a positron. The time axis runs from left to right.*

post-interaction state of quarks or gluons becomes a highly collimated spray of hadrons, or a *jet*. These ideas are strongly supported by experimental evidence, with jet observations now being central to the experimental programme of many facilities (figure 1.6).

The cross-section for the production of n jets is infrared safe. This means that an event with jets in the final state ought to be closely related to the same event with the groups of hadrons replaced by single partons, after the removal of soft partons and the combination of collinear particles. This produces a *parton level* event where calculations consider partons rather than hadrons in the final state. The infrared safety of the calculation can be summarised as stating that the infrared divergences cancel.

The hadronization process can also be pictured as being akin to the bremsstrahlung process for quarks as they decelerate when they move apart, due to the force between them. The idea of a QCD equivalent to the bremsstrahlung emission of photons by an accelerating electric charge is a

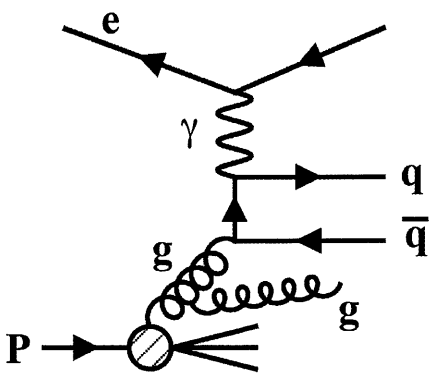

Figure 1.8: *Feynman diagram showing an example of a LO three jet process in DIS. The time axis runs from left to right.*

useful one. QCD bremsstrahlung consists of the emission of gluons in an interaction with other coloured particles. Bremsstrahlung gluon emissions from initial and final state partons are referred to as a *parton shower*.

At leading order in α_s, dijet production takes place in NC DIS interactions via the QCD-Compton and boson-gluon fusion processes as illustrated in figure 1.7. The contribution from the latter of these processes results in the multi-jet cross-section being directly sensitive to the gluon density within the proton. Three jet production can be modelled in a similar way to dijet production, with the third jet being due to an additional non-collinear bremsstrahlung gluon (figure 1.8).

The lowest (leading) order dijet processes illustrated in figure 1.7 each contain one strong coupling vertex, indicating that LO calculations for dijets contain terms of $\mathcal{O}(\alpha_s)$. The lowest order three jet processes (figure 1.8) contain two such strong vertices, meaning that LO calculations for three jet events contain terms of $\mathcal{O}(\alpha_s^2)$. In this work, the order stated refers to the order of the process being described and not the order of α_s utilised in the calculations, e.g. a tree

level trijet process is considered to be LO, but contains terms of $\mathcal{O}(\alpha_s^2)$.

1.3.8 Current Status of $\alpha_s(M_Z)$

The value of the strong coupling can not be measured experimentally but must be determined by a comparison of data (from an α_s sensitive measurement) to theory calculations. As $\alpha_s(M_Z)$ is effectively the only free parameter of QCD, the best way to quantify tests of the theory is by examining the consistency of determinations of this parameter. $\alpha_s(M_Z)$ can be extracted in many ways from many processes and the current world average value is

$$\alpha_s(M_Z) = 0.1187 \pm 0.0020 \tag{1.16}$$

according to the particle data group[12]. The uncertainty given includes both experimental and theoretical errors and includes an estimation of correlations between related values. This average and a selection of the contributing results is given in figure 1.9. Care must be taken to consider the order of the QCD calculations used in the determination. Next-to-next-to leading order (NNLO) calculations are available for e^+e^- collision processes, whilst NLO calculations for three-jet events in DIS have only recently become available. Figure 1.9 shows that $\alpha_s(M_Z)$ can be reliably and consistently extracted from various experimental processes but it is not intended to be exhaustitive. The values shown give a fair indication of measurement methods available and, if applicable, a reasonable spread of uncertainties from different processes is provided. The diagram also shows a determination from lattice gauge theory, which is, encouragingly, one of the more precise determinations. Values are based on the comprehensive overview of α_s determinations found in [12].

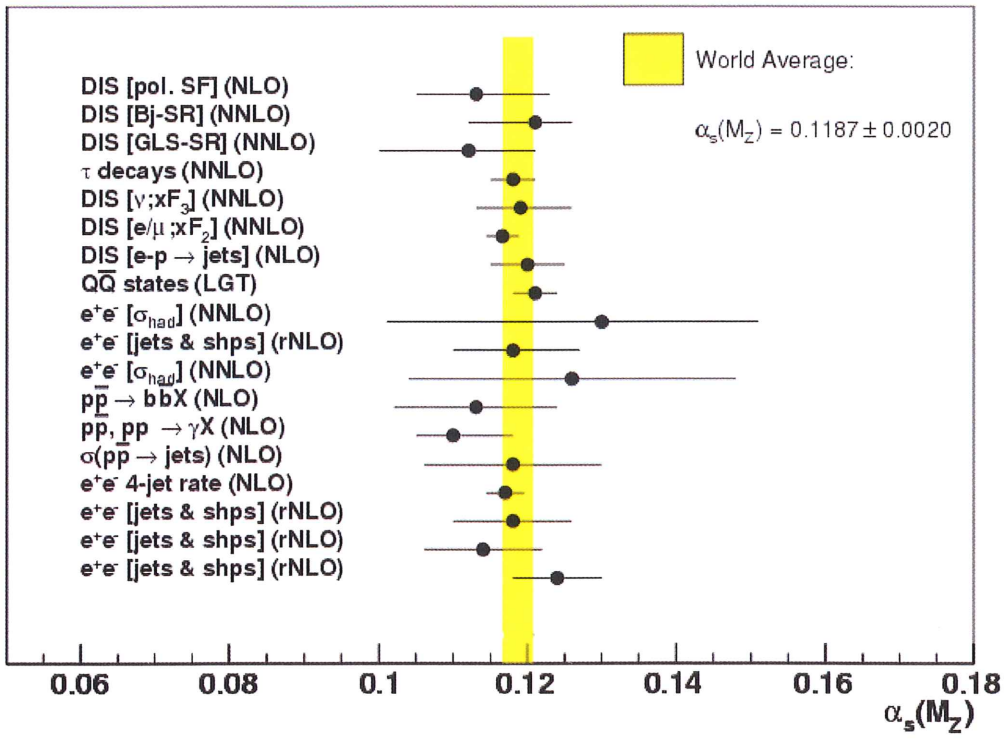

Figure 1.9: *Author's summary of current $\alpha_s(M_Z)$ determinations, based on the comprehensive overview from [12]. A selection of methods and a reasonable spread in uncertainties is provided. rNLO refers to resummed next-to-leading order and LGT indicates a determination from lattice gauge theory.*

Last Words

It is worth noting here that, although QCD is undoubtably a fine achievement of modern physics and is capable of describing many experimental observables in collider experiments, it is still not possible to calculate hadronic quantities such as the proton-neutron mass difference, or the force between two protons. This area of physics is still in need of much further research in order to answer these fundamental questions, the understanding of which would seem to be essential before an investment in more speculative theories is justifiable.

Chapter 2

The Concepts

This work is concerned with the relationship between the likelihood of DIS events with three or more jets and those with two or more. At lowest order, the ratio of the rates of these event types is proportional to the strong coupling at the scale of the interaction. The ratio of the inclusive trijet cross-section to the inclusive dijet cross-section will be refered to as $R_{3/2}$ in this work. Even when considering higher order effects and higher jet multiplicities, the overall relationship will still have a sensitive dependence on the strong coupling. By studying the cross-sections for multijet events as well as $R_{3/2}$, the efficacy of pQCD for describing the strong interaction can be precisely cross-checked. It is expected that an extraction of α_s from a study of $R_{3/2}$ will be both sensitive and precise. The procedure was first attempted at H1 [7], but insufficient data prevented an extraction of the strong coupling from being performed. The ZEUS Collaboration performed the first extraction from $R_{3/2}$ for DIS events [2] several years later, whilst this work represents the first extraction by the H1 Collaboration.

Definitions of the jet phase space employed can be found in a later section. The purpose of this section is to outline the ideas and concepts employed in a general manner.

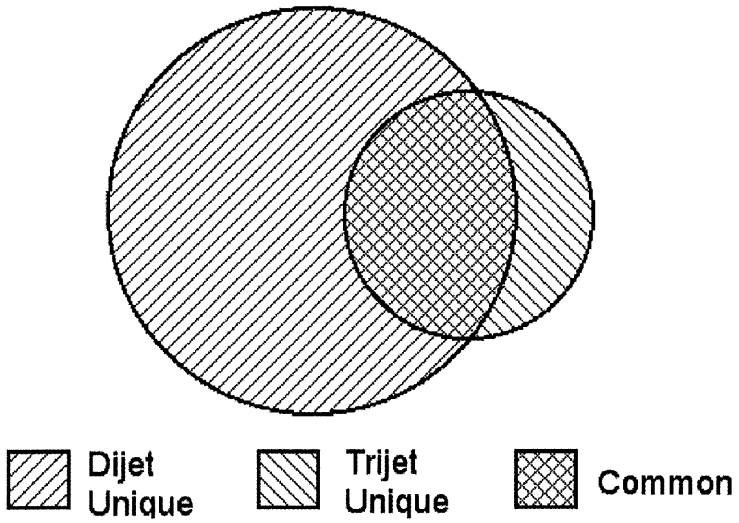

Figure 2.1: *Representation of overlap of dijet and trijet samples.*

2.1 The Method

The expression, including $\mathcal{O}(\alpha_s^3)$ effects, for $R_{3/2}$ as a function of $\alpha_s(M_Z)$ is:

$$R_{3/2}(\alpha_s(M_Z)) = C_1(Q^2)\alpha_s(M_Z) + C_2(Q^2)\alpha_s^2(M_Z) + C_3(Q^2)\alpha_s^3(M_Z) \quad , \quad (2.1)$$

where $C_1(Q^2)$, $C_2(Q^2)$ and $C_3(Q^2)$ are parameters which are expected to be positive for all values of Q^2. There is no constant term by necessity as $R_{3/2}(\alpha_s(M_Z))$ must be zero for the hypothetical case where $\alpha_s(M_Z) = 0$ as no QCD radiation would be present to produce the hadronic final states required for the event topologies considered in this work.

2.1.1 Overlapping Samples

Assuming that the trijet and dijet phase space is defined, the total event sample can be separated into three subsamples, containing events that are common to the dijet and trijet samples as well as events that are unique to each (see figure 2.1).

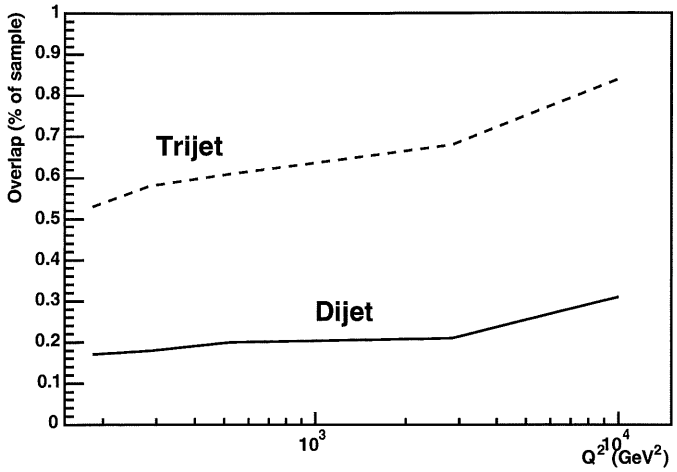

Figure 2.2: *Fraction of total trijet (dashed line) and dijet (solid line) samples that are common to both sets, as a function of* Q^2.

It is expected that the contribution to the theoretical uncertainty on $R_{3/2}$ from uncertainties in the PDF will be very small, as the same PDF is employed for both components of the ratio.

Consider two overlapping sets, X and Y, and let the total number of events, N_T, be expressed as the linear combination of the unique Y events, N_{uY}, the unique X events, N_{uX} and the common events, N_c such that $N_T = N_{uX} + N_{uY} + N_c$. The ratio of sample X to sample Y, $R_{X/Y}$, is given by:

$$R_{X/Y} = \frac{N_{uX} + N_c}{N_{uY} + N_c} \tag{2.2}$$

Differentiating the above expression provides the error on $R_{X/Y}$:

$$\delta R_{X/Y} = R_{X/Y} * \sqrt{(\frac{\delta N_{uX}}{N_{uX} + N_c})^2 + (\frac{\delta N_{uY}}{N_{uY} + N_c})^2 + (\frac{(N_{uY} - N_{uX})\delta N_c}{(N_{uY} + N_c)(N_{uX} + N_c)})^2}. \tag{2.3}$$

In the case where the errors considered are statistical errors, $\delta N_{uY} = \sqrt{N_{uY}}$,

$\delta N_{uX} = \sqrt{N_{uX}}$ and $\delta N_c = \sqrt{N_c}$. The errors due to the renormalization scale uncertainty in this analysis are treated in a similar way. The overlap of the samples causes a reduction in the error on $R_{X/Y}$ compared with the case where X and Y are completely independent.

Due to the correlated nature of systematic experimental errors (see chapter 5 for a full discussion of the sources of error considered), the effect of these uncertainies on $R_{3/2}$ is calculated differently. The error on $R_{3/2}$ is calculated as the difference between the measured value of $R_{3/2}$ and the value of $R_{3/2}$ obtained following the systematic shift in the variable under consideration. This can lead to significant reductions in systematic errors on $R_{3/2}$ in the case where the dijet and trijet cross-sections are effected by the systematic shift in a similar way, as is expected for the majority of systematics.

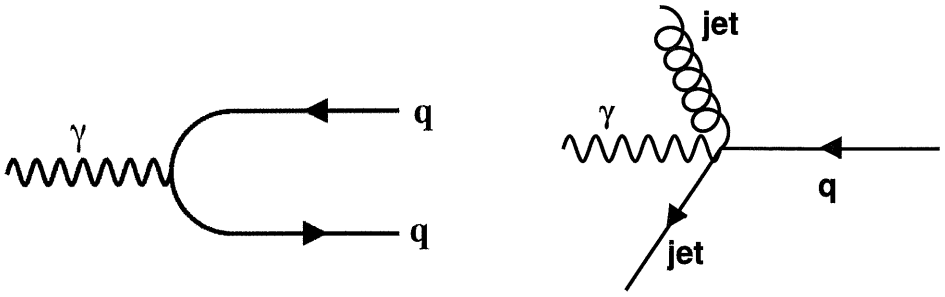

Figure 2.3: *Diagrams showing lowest order (left) and high E_T (right) jet events in the Breit frame.*

2.2 The Breit Frame

It has been shown[32] that for DIS jet events the factorisation of soft collinear QCD radiation from the initial state parton into the parton density functions is only permissable in certain frames of reference. One such frame, the Breit frame, is used for all jet observables in this work[31]. The Breit frame is defined as the frame in which the boson exchanged between the incident electron and proton is completely spacelike such that the relation $2x_{Bj}P^{\mu} + q = 0$ holds. The velocity of the Breit frame with respect to the laboratory frame is given by:

$$\frac{\mathbf{v}}{c} = \frac{(\mathbf{q} + 2x_{Bj}\mathbf{p_p})}{(q_0 + 2x_{Bj}E_p)} \quad . \tag{2.4}$$

The four-vectors describing the DIS events are boosted and rotated such that the exchanged virtual boson is orientated along the negative z axis and such that the scattered lepton is directed in the positive x direction. It can be seen from the definition of the Breit frame that the transverse[1] energy of the hadronic final state does not have to balance the transverse energy of the scattered lepton, as is required in the laboratory frame. Instead, it directly reflects the hardness of the underlying QCD process. At lowest order (Born level) the quark from the proton is backscattered and no transverse energy is produced. Jets with high E_T in this frame can only be accounted for by hard QCD pro-

[1]Transverse refers to the component perpendicular to the z-axis.

cesses whose contribution is at least $\mathcal{O}(\alpha_s)$ (figure 2.3)[32]. By imposing a cut on the transverse energy of jets, events corresponding to the purely electroweak Born level are excluded from consideration allowing precision studies of pQCD to be made. The Breit frame is also useful as it offers the maximum possible separation of the hard jets and the proton beam remnant.

Leading order diagrams for boson-gluon fusion (BGF) and QCD Compton (QCDC) events are given in figure 1.7. The BGF process dominates dijet production in most regions of phase space. Three other kinematic variables help us to describe dijet events. At leading order, in the special case where all final state partons are contained within the two leading (highest E_T) jets, the centre of mass energy is equal to the invariant mass M_{jj}. This means that the observable $\xi = x_{Bj}(1 + \frac{M_{jj}^2}{Q^2})$ represents an approximation to the proton momentum fraction carried by the struck parton. The variable $x_p = \frac{Q^2}{2\xi P^\mu q_\mu}$ is limited to the range $x_{Bj} < x_p < 1$. The final variable, z, is equivalent to the inelasticity, y. The matrix elements of the QCDC processes diverge as $z \to 1$ and $x_p \to 1$. The divergences for BGF events occur as $z \to 0$ and $z \to 1$ [6].

Chapter 3

The Tools

The data used in this research were collected using the H1 detector, at the HERA *ep* collider during the years 1999 and 2000. This section gives an overview of these tools, with particular attention being given to the components of the H1 detector that are most relevant to this work. The descriptions presented here pertain to the experimental set-up prior to the hardware upgrade of 2001. This section also contains a description of the software tools required to perform this analysis, these being primarily concerned with simulating *ep* collisions and the response of the H1 detector to such events. The software utilised for performing NLO multijet cross-section calculations is also described.

3.1 The HERA Electron Microscope

The HERA[1] *ep* collider is situated at the *Deutsches Elektronen Synchotron* (DESY) laboratory in Hamburg, Germany. It is effectively the highest resolution electron microscope ever constructed, with a resolving power of $\sim 10^{-18}$m, or 10^{-3} of the classical proton radius. At this resolution, the nucleon can be seen to possess a substructure that increases in complexity at decreasing distances. In order to probe the structure of the proton at these most fundamen-

[1]Hadron Elektron Ring Anlage.

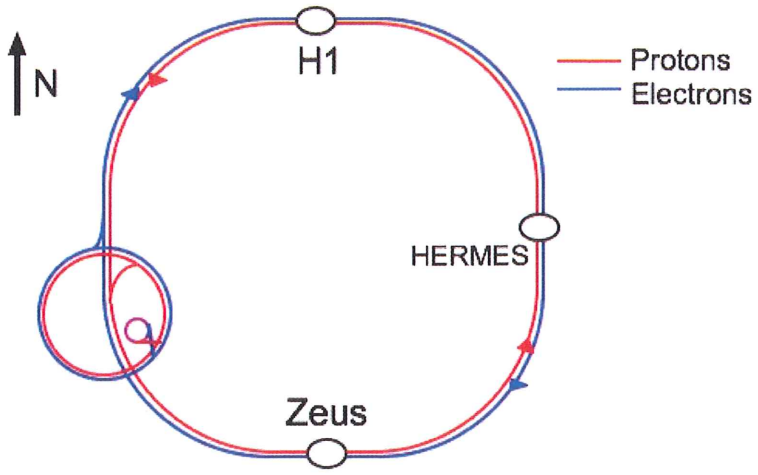

Figure 3.1: *The HERA accelerator with experiment locations.*

tal distance scales, 27.6 GeV electrons and 920 GeV protons[2] are brought into collision at a centre-of-mass energy of $\sqrt{s} \sim 319$ GeV.

To make these collisions possible, the particles involved are stored in two concentric storage rings, each 6.4 km in circumference - one for electrons and one for protons (figure 3.1). Each ring consists of an beam-pipe that is held at near vacuum conditions (pressure $\sim 10^{-9}$ bar). Pumps, cooling equipment and the dipole and quadrupole magnets required to steer and focus the particle beams, surround the beam-pipes. Prior to injection into the main HERA rings, the particles are first accelerated to an intermediate energy in a series of smaller rings and pre-accelerators. Once inside HERA, the particles are accelerated to their desired energy and stored in bunches, with each ring capable of containing two hundred and twenty bunches, each of around 10^{11} particles. Particles are brought into collision by crossing the bunches at two specific points on the ring, where apparatus to detect the products of the collisions is situated. The nominal timing between bunches is 96 ns and, under good conditions, about one hundred and seventy-five of the bunches will be brought into collision. A detailed understanding of backgrounds caused by beam-pipe and beam-gas

[2]The procedure of passing H^- ions through a stripper foil is utilised to produce protons.

interactions is acquired by studying the interactions of electron or proton *pilot* bunches, i.e. bunches which do not have a proton or electron bunch partner, respectively.

The beam interaction regions are situated at opposite locations on the HERA ring, at the northern and southern points. The ZEUS detector resides in the south, the H1 detector in the north. Furthermore, at the eastern point, the HERMES experiment utilises the polarised electron beam in fixed target collisions with hydrogen, deuterium or helium gas in order to measure the spin-structure of the nucleon. The western point was formally occupied by the HERA-B experiment, which was designed to study physics in the b quark sector. This experiment was removed from the beam line during 2001.

3.2 The H1 Detector

3.2.1 Overview

Figure 3.2 shows a schematic of the H1 detector. Due to the asymmetry in the energy of the electron and proton beams at HERA, the centre-of-mass for ep collisions is strongly boosted along the proton direction. To account for this, the H1 detector is asymmetric in design [53], being considerably more massive and highly segmented in the forward direction. This may be seen in figure 3.2, which shows a cut along the beam axis.

The polar angle θ is measured with respect to the direction of the proton beam. The H1 coordinate system is a right handed Cartesian system, with the z-axis pointing in the proton beam direction, known as the "forward direction", and the x-axis pointing towards the centre of HERA. The coordinate origin is at the nominal interaction point, which is at the centre of the inner silicon tracker. It is often convenient to use cylindrical coordinates for which the radial coordinate r is taken as perpendicular to the z-axis and the azimuthal angle Φ is positive for all positive values of y.

The interaction point is surrounded by tracking chambers and calorimeters that are in turn surrounded by a superconducting solenoid providing a uniform magnetic field of 1.15T parallel to the beam axis in the tracking region.

Luminosity is measured using the Bethe-Heitler process $ep \rightarrow e\gamma p$. This is an elastic bremsstrahlung process with a well known cross-section and is thus excellently suited to a precise determination of the luminosity. The final state electron and photon are detected in calorimeters situated close to the lepton beam pipe[35]. These detectors are known as the electron tagger, situated at $z = -33.4$m, and the photon detector, situated at -102.8m. The uncertainty for the luminosity measurement is given as 1.5%.

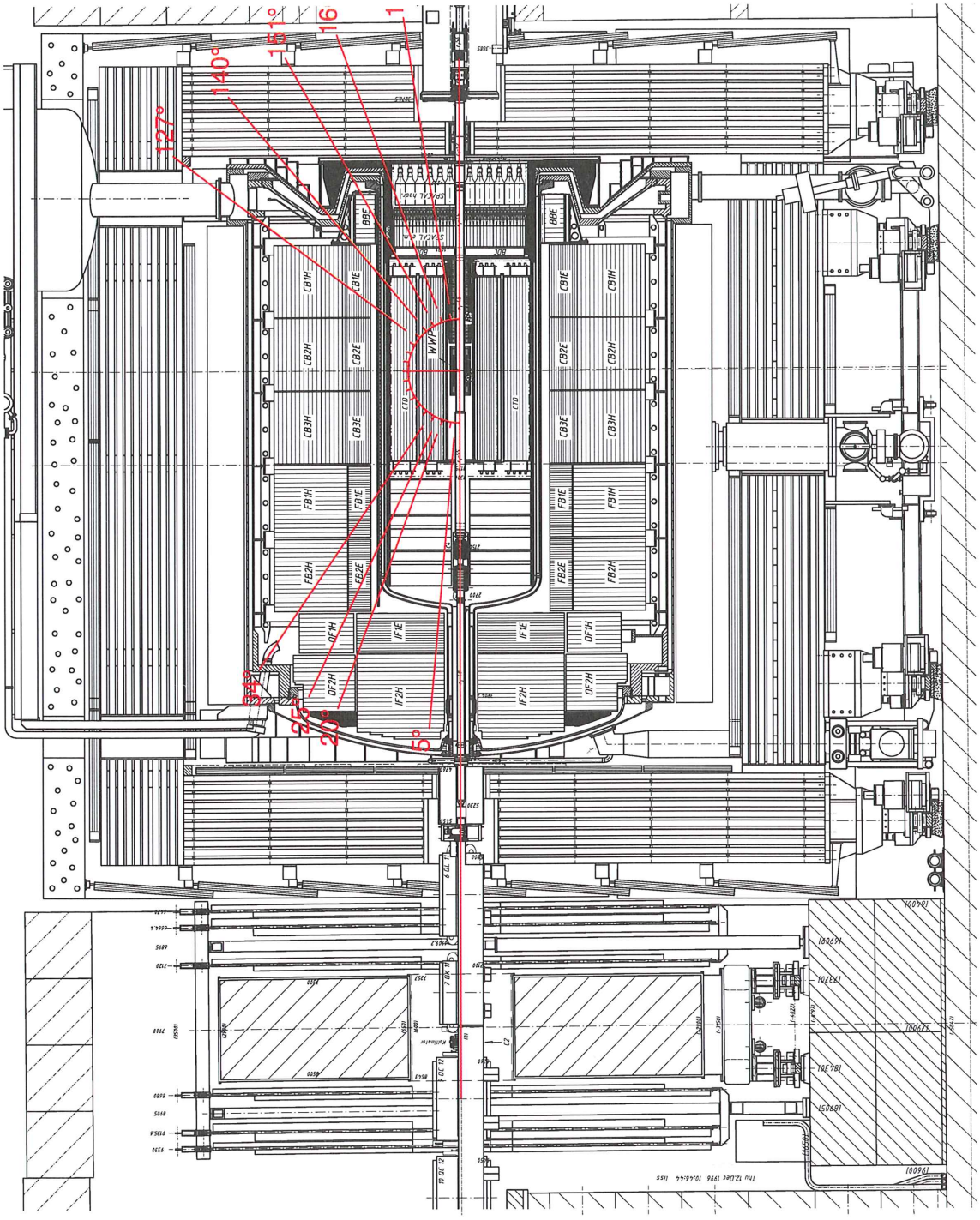

Figure 3.2: *Cut along the beam axis of the H1 detector (c. 1996).*

3.2.2 Tracking

The tracking system is divided into three principle components that cover the forward, backward and central regions. The forward track detector covers

$7° < \theta < 25°$ and consists of drift chambers with alternating planes of wires parallel to the z-axis and others with wires in the radial direction arranged into three larger modules. The momentum resolution of the forward track detector is $\frac{\sigma p}{p^2} < 0.03$ GeV^{-1} and the angular resolution $\sigma_{\theta,\Phi} < 1$ mrad[33]. The forward track detector is not used for locating the interaction vertex for events considered in this work due to several operational problems suffered by this device during the run periods under consideration.

The main components of the central tracking device are the two concentric drift chambers (CJC1 and CJC2), which cover the angular range $15° < \theta < 165°$. They have wires strung parallel to the z-axis in order to provide measurements in the $r - \Phi$ plane and a transverse momentum resolution of $\frac{\delta p_T}{p_T} < 0.01\ p_T$ GeV^{-1}. The central inner and outer z-chambers (CIZ, COZ) act to improve measurement of the z coordinate. Thus, the wires lie approximately on circles of constant radii to produce a drift direction along the z-axis. The final two components of the central tracker are the central inner and outer proportional chambers (CIP and COP), which are used primarily for triggering. These Multi-Wire Proportional Chambers (MWPCs) possess a fast response time and are thus well suited to this task with a time resolution better than the separation between bunch crossings at HERA. The central tracker is used to reconstruct the primary interaction vertex for events used in this work.

The drift time measurement from the CJC also provides an indication of when an event took place, known as its T0. Events with a T0 which does not coincide with a bunch crossing are unlikely to have resulted from an ep collision and can be rejected as background.

3.2.3 Calorimeters

In the angular range $4° < \theta < 154°$, electromagnetic and hadronic energies deposited by particles from the ep collision are measured by the Liquid Argon

(LAr) calorimeter, consisting of an electromagnetic section with lead absorbers and a hadronic section with steel absorbers. The LAr is highly segmented and situated inside the solenoid to prevent energy losses in the uninstrumented iron. It consists of eight wheels in the z direction with each of these being composed of eight sections known as octants. The most backward wheel, known as the BBE, does not have a hadronic section. The electromagnetic sections have a depth of around 25 radiation lengths with the total depth of the calorimeter varying between 4.5 and 8 hadronic interaction lengths. The energy resolution for the electromagnetic sections was found to be $\frac{\sigma_{em}}{E} = \frac{0.11}{\sqrt{E\ [GeV]}} \oplus 0.01$ for electrons[1]. The resolution for charged hadrons was found to be $\frac{\sigma_{had}}{E} = \frac{0.5}{\sqrt{E\ [GeV]}} \oplus 0.02$ from test beams [36]. The LAr is principally employed to measure the energy of the scattered electron for values of Q^2 above about 100 GeV^2 and as such is used for all events considered in this work. It is also used for measurements of the hadronic final state such as for the jet analysis described here.

The backward region ($153° < \theta < 177°$) is covered by a lead-fiber calorimeter, known as the SPACAL. The iron return yoke for the magnetic field, situated outside the solenoid, is instrumented and is utilised for identifying muons and to estimate the energy of hadronic particles not measured by the LAr. This system is known as the tail catcher. The final calorimeter at H1 is the plug, which is used to cover the region between the LAr and the beam pipe in the positive z direction. Besides a small contribution from the SPACAL, none of the contributions from these system are included in the hadronic final states considered in this work.

3.2.4 Time of Flight System

The time-of-flight (ToF) system is used to reduce background caused by interactions of the proton with the beam pipe or the residual gases within the

[1] $\oplus$ signifies addition in quadrature.

beam pipe. Such events will occur on time scales that are inconsistent with genuine *ep* collisions at the nominal interaction vertex. The ToF system consists of plastic scintillators mounted around the beam pipe at both ends of the detector, the high speed response ($\sim$ 2 ns time resolution) of which makes it possible to reject events with signals in the ToF that do not coincide with the precisely known bunch crossing timings provided by the HERA clock.

3.2.5 Trigger System

The time between *ep* collisions during normal running is 96 ns, giving a colliding frequency of 10.4 MHz. The rate at which the information from the various detector components can be acquired is much slower. A large quantity of events consist of backgrounds such as synchrotron radiation from the lepton beam or beam gas interactions with the proton. In order to avoid missing genuine *ep* events, a system for triggering on genuine *ep* events is utilised. The trigger system is multilayered (L1-L5) with each successive layer having more time to decide on the event quality. L1 to L4 are conducted in real time, with L5 acting offline. The overall rate of event recording is about 10 Hz. The data considered for this work have trigger requirements based on L1, L4 and L5 and so more detail is provided for these layers.

The first trigger layer, L1, utilises information from all detector components known as trigger *elements*, of which there are about 200. These elements are combined by the central trigger logic system into 128 *subtriggers*. If any one of the subtrigger conditions are met (signals in particular detector components), the event passes onto the next layer that has more time to perform a more rigorous selection. The decision making process takes approximately 24 bunch crossings and so information from subsequent collisions is stored in a pipeline so that there is no delay in taking new data. The subtriggers that are present are recorded with each event. The subtriggers used for this work are S67, S75 and S77 with the subtrigger S71 used to monitor the efficiency of these

triggers. The subtrigger S71 is active for events with a central vertex, three or more central tracks with $p_T > 420$ MeV and a track combined with a cluster in the LAr. This trigger is independent of the other triggers employed in this work and it is thus used to monitor their efficiency. Trigger S67 requires that the energy in the electromagnetic section of the LAr is greater than 3.8 GeV. Trigger S75 requires that the energy in the electromagnetic section of the LAr is greater than 2.8 GeV and that there is at least one central track with $p_T >$ 420 MeV. The final subtrigger, S77, requires that the missing transverse energy in the LAr is below a cut-off value and is employed to ensure that events are consistent with neutral current topologies.

Trigger layer four (L4) occurs quasi-online and consists of a farm of processors used to perform more accurate calculations of various quantities. It is used for providing more detailed selections as well as reconstruction of tracks and clusters for each event. Trigger layer five (L5) consists of full event reconstruction using the H1REC software [37] (see for example appendix E, figure E.1). Each event that reaches L5 is verifed to high precision and, if selected, written to tape for permanant storage. The output is written in full to Production Output Tapes (POTs) and a reduced version is written to Data Summary Tapes (DSTs). DSTs are processed further for physics analysis at a later stage. At DST level, each event consists of about 10kB of information.

3.2.6 Particle Identification

Isolated energy deposits in the electromagnetic section of the LAr are considered as candidates for the scattered electron. The highest P_T candidate is used as the scattered electron. The electron finding algorithm is over 99% efficient for all regions of the LAr except within the detector cracks between the wheels CB2, CB3 (see figure 3.2) and around each octant [38]. In order to ensure that the electron candidate is a clean energy deposit, an isolation criteria in

pseudorapidity[2]-azimuth ($\eta - \Phi$) space is made such that no more than 3% of the electron energy lies in a cone of radius 1 around the electron candidate. The scattered electron energy, E', and the polar angle θ are determined from the LAr.

The four-vector of the hadronic final state is measured using the LAr, SPACAL and track momentum information. The momentum measurement for $P_T < 2$ GeV hadrons is more accurately determined by the trackers than the calorimeters, which allows for the inclusion of low P_T tracks without an associated cluster.

[2]Pseudorapidity is defined as $\eta = -\ln(\tan\frac{\theta}{2})$ where θ is the polar angle.

3.3 Event Simulation

3.3.1 Overview

The general features of DIS events are well described by leading order (LO) calculations. Accurate predictions of multi-jet event rates would require next-to-leading order (NLO) calculations. Full NLO event simulations are not yet available for DIS events. An alternative method to obtain an approximation to higher order calculations is to use programs based on parton cascade models. Programs such as RAPGAP [44], HERWIG [46] and LEPTO [47] contain additions to the LO matrix element described by parton shower models. The program ARIADNE [48] utilises the colour dipole model for these approximations. Programs to perform parton level cross-section calculations, at NLO, in DIS for jet multiplicities up to and including three jets are available and are employed in this study.

In this analysis the programs DJANGO (version 1.2) [50] (used as an interface for ARIADNE) and RAPGAP (version 20.8) [44] are utilised. These programs simulate the hard (DIS) scattering process for leptons on protons, and include first order QED radiative corrections (via the HERACLES program [51]) as well as initial and final state QCD radiation ($\mathcal{O}(\alpha_s)$). Previous publications [59] have shown that the event generators used in this analysis provide an acceptable description of the internal structure of jets.

The simulated events are passed through a detailed simulation of the H1 detector, where the detector response (e.g. wire hits within the trackers, energy deposits in the calorimeters) for the generated event is simulated by the program H1SIM. The events are then reconstructed by the same software used for the reconstruction of data events. The reconstructed events are then used for comparision with the data.

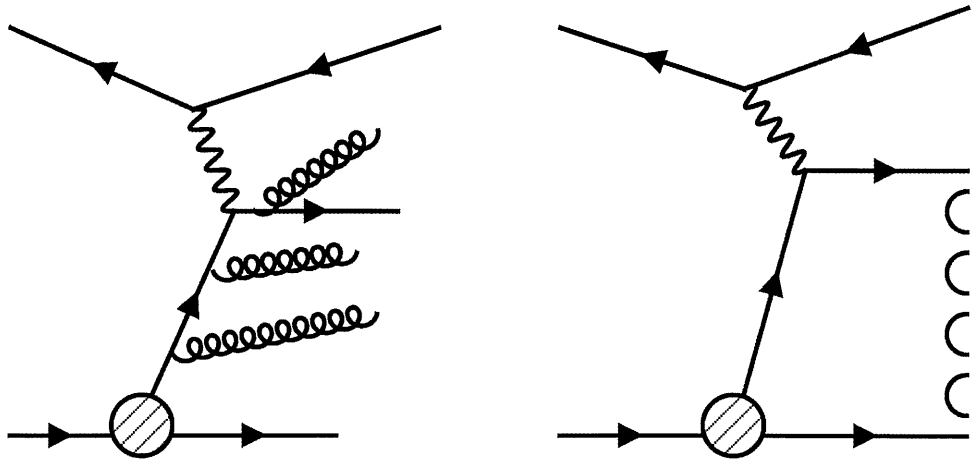

Figure 3.3: *Representation of parton shower (left) and Colour dipole models (right).*

3.3.2 RAPGAP

RAPGAP (version 20.8) is an event generator capable of simulating deep-inelastic scattering, photoproduction, diffractive DIS and photoproduction as well as processes involving π exchange. It provides the option for initial state QED radiation via the HERACLES 4.4 program and can include higher order QCD approximations by either utilising initial and final state parton showers or the ARIADNE colour dipole model (version 4). The non-perturbative hadronization process is simulated via the LUND string model program JETSET 7.4. RAPGAP provides QCD matrix elements that are leading order in α_s and in this work the renormalization / factorisation scales are set to the momentum transfer of the virtual boson that mediates the ep interaction (Q). The PDF CTEQ5L is utilised and α_s evolved according to the one loop solution of the renormalization group equation. Many physics parameters are user defined and can be tuned to the analysis being undertaken. The treatment of the beam remnant and initial state parton showers are similar to those employed in LEPTO (version 6.1) [47] and PYTHIA [56]. Further technical details for RAPGAP, including the treatment of initial state QCD radiation,

can be found in [45].

The higher order QCD approximations available in RAPGAP utilise a virtuality-ordered parton shower based on soft and collinear approximations. The cross-section for multiple emissions can be described as a probabilistic series of parton splittings. The QCD cascade is composed of initial and final state showers that are space-like and time-like respectively. The parton shower is matched to the $\mathcal{O}(\alpha_s)$ matrix elements. A representation of the parton shower model is shown in figure 3.3 (left).

3.3.3 DJANGO

DJANGO (version 1.2) is an interface for the programs LEPTO, ARIADNE and HERACLES. It allows simulation of ep collisions with the option of initial and final state parton showers and initial state QED radiation. The LUND string model is employed to model the hadronization process via the program JETSET 7.4. Most relevant features are similar to those described for RAPGAP above. In this work, the program ARIADNE is used to implement the colour dipole model (CDM) for the QCD cascade. In this model, gluon emissions are described as radiations from the colour dipole between pairs of partons. The process $g \rightarrow q\bar{q}$ is also added to the model. A representation of the colour dipole is shown in figure 3.3 (right).

3.3.4 QED Radiation

A discussion of the effects of electroweak radiative effects in DIS is provided in chapter two. These effects are dealt with for simulated events by the program HERACLES, which is interfaced to the Monte Carlos detailed above. The effects of QED radiation are well understood and the effect on the cross-sections is correspondingly precisely known.

3.3.5 Hadronization

At the time of writing, full Monte Carlo simulations for deeply inelastic lepton proton scattering are only available with leading order (LO) matrix element processes included. However, many tests of QCD, such as the extraction of the strong coupling, require predictions to include terms that are at least next-to-leading order (NLO). Programs exist for making these calculations for jet cross-sections, up to and including jet multiplicities as high as trijet events, and have been shown to agree with data to $\pm 5\%$, or better (see later section). These programs only produce values for the cross-sections and do not give a full simulation of DIS events - the values for the cross-sections produced are at what is known as the *parton level*. The parton level can be thought of as the pure products of the DIS interaction, before any quarks or gluons in the final state have hadronized. Of course, this has little meaning in reality, where the concept of a *free* quark is incompatible with our current theoretical understanding of QCD (see chapter 2). It certainly isn't what is measured in an experiment such as H1. This is where the same LO Monte Carlos used for detector and QED corrections can prove their usefulness yet again. The process of hadronization is not completely understood, but there are several models that seem to give a good approximation to what is occurring. The two most popular models are the HERWIG cluster algorithm and the Lund string model. These are implemented by programs that are interfaced to LO simulations such as DJANGO or RAPGAP. The HERWIG program utilises the cluster method, whilst the string model is implemented by the program JETSET.

Figure 3.4 shows a schematic representation of the hadronization process as implemented in HERWIG. Pairs of partons are associated into colourless clusters, which then undergo phase-space decay to produce stable hadrons. Clusters with a mass greater than a mass parameter M_{cl} are split before this decay occurs. The HERWIG program requires much fine-tuning for the description

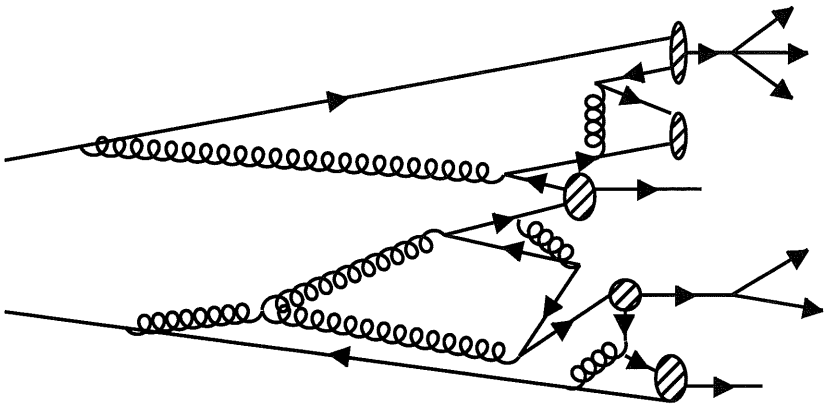

Figure 3.4: *Schematic of hadronization in HERWIG. Colourless clusters are formed from pairs of partons.*

of high jet multiplicities. An adequate description of the experimental data for trijet events (see chapter 4) could not be obtained, using HERWIG, within the time constraints of this work and as such was not considered for further use.

JETSET utilises the Lund string model of hadronization, a schematic of which is shown in figure 3.5. The colour field between partons is represented as a one dimensional massless relativistic string that ends at quarks and antiquarks with gluons being represented by momentum carrying kinks in the string. The fragmentation of the string is performed iteratively using the following mathematical structure,

$$f(z) \propto \frac{1}{z}(1-z)^a \exp(-b\frac{m_\perp^2}{z}) \quad , \tag{3.1}$$

where z is the fraction of the $E + p_{||}$ of a parent string fragment taken by a daughter, $m_\perp = \sqrt{p_\perp^2 + m^2}$, where perpendicular and parallel refer to the string axis and a and b are parameters. Transverse momentum is introduced randomly using a Gaussian probability distribution. The details of particle

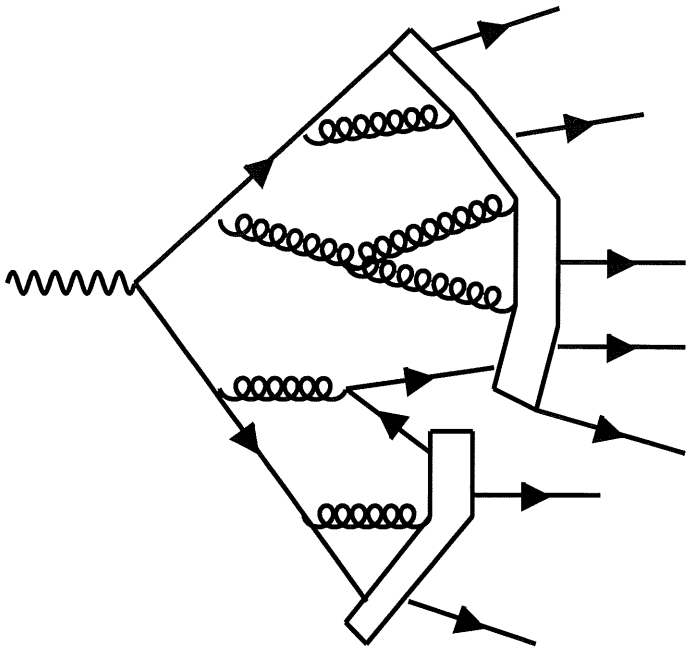

Figure 3.5: *Diagram of hadronization in JETSET. In this example, the parton cascade contains a perturbative $g \rightarrow q\bar{q}$ vertex causing two strings to form. Gluons are thought of as introducing 'kinks' into these strings.*

production are controlled by a large number of parameters. JETSET has been proven to accurately model events featuring high jet multiplicity final states [6, 7, 2] and it is chosen as the hadronization model to be employed for this work.

3.4 Jet Algorithms

The hadronic final state can be studied in detail by using so-called *jet algorithms* to separate the hadronic final state into collimated *jets*, the expected observable final state in DIS. The cross-sections required for this work are dependent upon properties of the jets and so a clearly defined procedure is required to systematically cluster the final state particles. This is slightly problematic, as there is no unique method for this and the cross-sections will inevitably depend on the jet definitions. It must be noted, that whilst the cross-sections and their ratio will be effected by the choice of jet definition, the

extracted value of α_s will not as the same definition will be applied consistently throughout the analysis and extraction.

Different jet definitions will be influenced in different ways by the effects of hadronization and have different sensitivities to low energy particles in the hadronic final state. One procedure defines jets by maximizing the transverse energy flow through a cone of a given radius. Cone algorithms have been criticised [62] due to the possible ambiguities of particle assignment to different jets. Whilst cone algorithms remain popular, particularly at hadron-hadron based experiments, this ambiguity is deemed unacceptable for this analysis, where the large uncertainties introduced are inappropriate for the precision comparison of data to perturbative calculations required.

The most popular form of definition today is based on an iterative recombination procedure, known as a clustering algorithm. For such a definition, it is required to specify the manner in which particles are clustered to form jets. It has been suggested that the relative transverse momenta $k_\perp$ is a good choice of clustering variable [63] and this choice has been proven to be effective (see for example [6]).

There is a further definition to be made, that being the distinction between *inclusive* and *exclusive* jet definitions. Exclusive definitions cluster every final state particle into one of the jets and are employed where the entire final state is expected to be composed of hard jets, such as in e^+e^- collisions. Inclusive definitions cater for final states resulting from collisions involving hadrons where particles from the beam remnant are present, but not included within the hard jets. Exclusive definitions for DIS also exist, where the beam remnant is clustered into explicit jets that can then be neglected.

For DIS, the $\gamma - p$ centre-of-mass frame differs from the Breit frame by a

longitudinal boost (see chapter 2). It is therefore required that the distance parameters in the clustering algorithm are invariant under longitudinal boosts. Examples of such quantities are the transverse energy, the azimuthal angle and the pseudorapidity.

It has been found [6] that the inclusive $k_\perp$ algorithm produces smaller hadronization corrections for multijet events than for other available algorithms and as such it is utilised for the jet definitions in this work.

3.4.1 The Inclusive $k_\perp$ Algorithm.

The clustering procedure utilises two lists, one that starts as a list of all available particles and the other as an empty list that will contain a list of the jets. For each particle, i and each pair of particles i, j the distances d_i and $d_{i,j}$ are calculated where:

$$d_i = E_{T,i}^2 \quad ; \quad d_{i,j} = \min(E_{T,i}^2, E_{T,j}^2)\frac{R_{i,j}^2}{R_0^2} \quad . \tag{3.2}$$

Here $R_{i,j}^2 = (\Delta\eta_{i,j})^2 + (\Delta\Phi_{i,j})^2$ and R_0 is chosen to be unity. The smallest value of d_i and $d_{i,j}$ is known as d_{min}. If d_{min} belongs to the set of $d_{i,j}$ the particles i and j are merged into a new particle. If d_{min} belongs to the set of d_i, then the particle i is moved from the list of particles to the list of jets. The procedure is repeated until the list of particles is empty. From this procedure, it can be seen that the last jets entered into the list of jets will be those with highest transverse energies E_T.

3.5 NLO Predictions

3.5.1 Choice of Program

There are several programs available to perform parton-level dijet cross-section calculations in next-to-leading order. DISENT [42] and DISASTER have been used in many previous analyses and provide consistent results [43]. However, only NLOJET++ allows the three jet cross-section from ep collisions to be calculated to NLO. NLOJET++ has been shown to be consistent with both DISENT and DISASTER for the dijet cross-section at LO and NLO [7, 60].

The influence of heavy quark masses and electroweak effects are not included in the NLOJET++ calculations. It has been shown that, at LO, these effects are small ($< 1\%$) for the kinematic region considered in this analysis, with the exception of the final Q^2 bin ($5000 < Q^2 < 15000$ GeV^2), where the expected change in the dijet cross-section resulting primarily from the inclusion of Z exchange is $\sim 20\%$. For this reason, the final Q^2 bin is neglected in the QCD analysis presented in this document. It may be possible to include this region using an electroweak correction procedure, using a method similar to that employed for detector, QED and hadronisation corrections, but this procedure has not been attempted in this work.

The NLO predictions use the $\overline{MS}$ scheme for five massless quark flavours. The PDF used in this analysis for comparison with data was CTEQ5M (the CTEQ4A[61] PDF is also employed for the QCD analysis). The value of $\alpha_s(M_Z)$ used with this PDF was $\alpha_s(M_Z) = 0.118$, and this value was subsequently evolved according to the second order solution of the renormalization group equation. NLOJET++ produces cross-sections at the parton level and as such requires a correction for hadronization effects before a comparison with data can be made (see previous section).

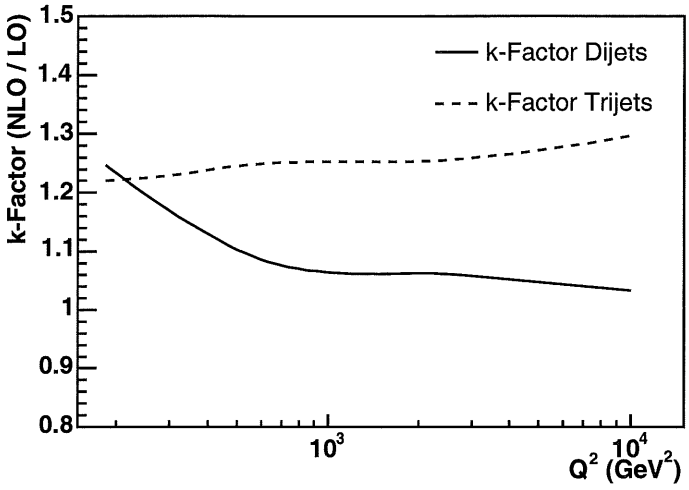

Figure 3.6: *k-Factors for dijets (solid line) and trijets (dashed line). Q^2 is used as the choice of renormalization/factorisation scale.*

3.5.2 Choice of μ_r and μ_f

The choice of renormalization and factorisation scales is almost entirely arbitrary, although it is sensible to choose a scale such that theoretical uncertainties associated with the choice of scale are minimised. One simplistic requirement is that $\log(\frac{\mu_r^2}{s})$[1] ought not be large, otherwise the perturbative functions in pQCD will fail to converge and calculations will become unreliable.

For the region of Q^2 considered in this analysis, it has been shown that little difference results in the size of the NLO corrections, for dijets, if Q^2 or $\overline{E_T}^2$ is chosen for the renormalization/factorisation scale [6]. It has been observed that the choice of Q^2 produces marginally smaller scale uncertainty for the value of $R_{3/2}$ and this is also seen to be a harder scale for the majority of events in the data. Thus, this scale has been chosen for the renormalization/factorisation scale in this work, although it is stressed again here that the choice of these scales is arbitrary[3]. Uncertainties associated with the choice of

[1] Recall s is the centre of mass energy squared.

[2] Mean E_T of the leading jets.

[3] It is customary to set $\mu_r = \mu_f$ as it produces smaller uncertainties, but these variables

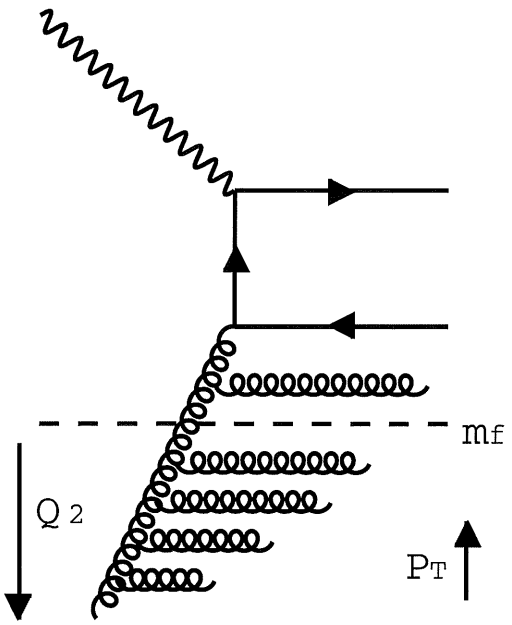

Figure 3.7: *Pictorial representation of μ_f choice.*

scale are found by examining the effect of a factor of two change in the renormalization/factorisation scale chosen, although this method is merely conventional. Values for the k-factor, which represents the size of the NLO correction to the born level, for dijets are $\sim$ 1.2 - 1.05 and for trijets are $\sim$ 1.25 (figure 3.6).

Based on the description of QCD given in chapter 2, it is possible to obtain a qualitative, perhaps intuitive, idea of what values these arbitrary scales may be set to. It is valid to state that setting $\mu_f^2 = Q^2$ is a sensible choice. The reason for this can be pictured by considering the virtuality of the electroweak probe as a measure of the distance (depth) of penetration into the proton. It can be considered that QCD radiation from the "struck" parton is emitted in a continuum in P_T such that radiation that is emitted "short" of the penetrated distance (that is, with momentum below Q^2) can be thought of

are independent.

as being radiated "within" the proton and thus be considered as part of the parton density function (figure 3.7). The relationship between space and momentum described here is approximate at best, but the choice of $\mu_f^2 = Q^2$ has been repeatedly proven to be a sound one.

Chapter 4

The Data

4.1 Data Set

The data used in this work were collected with the H1 detector during the 1999-2000 data taking period at HERA and corresponds to an integrated luminosity of 65.4 pb^{-1}. Data taken during this time was primarily composed of positron-proton collisions and those data using electrons instead of positrons are not considered in this work. The events chosen for this analysis are characterised by a high-energy isolated positron in the central region of the detector.

Each fill of the HERA rings with electrons and protons is divided into several data taking *runs* by H1. Background conditions and other experimental factors are not constant throughout each run and so only runs that occur under acceptable conditions are analysed here.

The kinematics may be defined using information from the scattered electron alone, the hadronic system, or a combination thereof. An overview of the reconstruction methods is detailed in appendix D.

Example events (as visualised by the H1 event display) that illustrate various features of the H1 detector and several of the background phenomena rejected

in this work as well as a set of clean multijet events can be found in appendix E.

4.2 Phase Space

The differential cross-sections presented are given for the kinematic region defined by $150 < Q^2 < 15000$ GeV^2, $0.2 < y < 0.6$ and $s = 4E_pE_e$. The range of y was chosen to exclude regions with large x_{Bj} (where jets tend to be produced in the forward direction, at the edge of detector acceptance) and to ensure large energies of the scattered positron respectively. The y range also ensures higher bin purities and smaller correction factors than an alternative range $0.15 < y < 0.7$, which was also investigated.

4.3 DIS Event Selection

The event selection criteria closely follow those used in recent measurements of the inclusive DIS cross-section[54], the dijet cross section[6] and the trijet cross section[7]. The following selection criteria were applied:

- A reconstructed vertex within $\pm$ 35 cm of the nominal interaction vertex was required to ensure that events are consistent with inelastic ep collisions.

- In order to suppress photoproduction events, $E - P_Z$ was required to be greater than 45 GeV. An upper limit of 65 GeV was also applied to $E - P_Z$ to reduce any cosmic ray background.

- The scattered electron was required to have an energy of at least 11 GeV with a polar angle $\theta < 153°$. For $\theta < 35°$ the positron candidate is only valid if it can be associated with a reconstructed track pointing in the direction of the positron cluster with a distance of closest approach (DCA)

of less than 12 cm to help reduce backgrounds from misidentification of the scattered electron.

- To ensure sound event reconstruction, the sub-detectors CJC1, CJC2, CIP, COP, TOF, LAr, SPACAL and Lumi system are required to have been fully operational during the data taking run (for example, see figure E.8).

- Fiducial cuts were made to avoid cracks in the detector acceptance in the Φ and Z directions where the efficiency of both the trigger and the electron finder is less than 100%. These regions occur at 2° either side of the octant edges and at $15.0 < Z < 25.0$ cm (for example, see figure E.4).

- The event interaction vertex must be detected using the central tracking system and the scattered electron must be found in the LAr calorimeter.

- A requirement is made that the CJC T0 be within 20 ns of the nominal bunch crossing time (for data events), to remove non *ep* background.

- The polar angle of the hadronic final state must be >8° to ensure that the jets are within the geometric acceptance of the LAr.

- In charged current events, the initial state electron is converted to a neutrino that passes undetected resulting in an imbalance in the measured transverse momentum. In order to reduce the number of charged current events that make it into the event sample, a cut of $P_{Tmiss} < 15$ GeV is applied.

- A series of topological background finders to remove remaining background from lepton pairs, beam halo muons and cosmic rays were also utilised (for example, see figures E.5 and E.6).

The subtrigger combination (S67 || S75 || S77) is used for triggering events,

with S71 used as a monitor trigger. For this description, || represents a logical OR operation. An event is retained if it passes any of the subtriggers S67, S75 or S77 and is then verified by the L4 offline trigger. The trigger efficiencies for all samples are above 99%. Figure 4.1 shows an example of the trigger efficiencies for various event variables for the dijet sample. It can be seen that there is less data in the bin around $\Phi = 0°$ for the leading jet azimuthal angle. This is because in the Breit frame, the scattered electron is found at $\Phi = 0°$ *by definition* and there is a slight reduction in the probability of finding jets in this region due to a requirement for an isolation cone surrounding the scattered electron candidate.

Regions of the LAr, where the subtrigger S67 is $< 100\%$ efficient, were removed. The remaining events were reweighted to account for the event loss, using the concept of Φ symmetry.

The variables Q^2, x_{Bj} and y were determined using the electron-sigma method [55] (see appendix D for an outline of the various reconstruction methods).

4.3.1 Calibration

The calibration of the electromagnetic and hadronic energy scales of the LAr is performed as described in[39], an overview of which is presented here. The scattered electron energy, E', from NC DIS events was measured by the LAr and also reconstructed using the Double Angle (DA) method (see Appendix D). The ratio $E' : E_{DA}$ was taken and calibration constants introduced to bring this value into agreement with that for simulated events, which are centred around unity. These calibration constants are a function of z and Φ, with each wheel of the LAr performing differently. The areas of low efficiency mentioned above were excluded from the study. The final calibration constants are such that the double ratio of $E' : E_{DA}$ to its value in simulated events (ideal calibration) is unity within 0.7% - 3%, depending upon the z position. This calibration

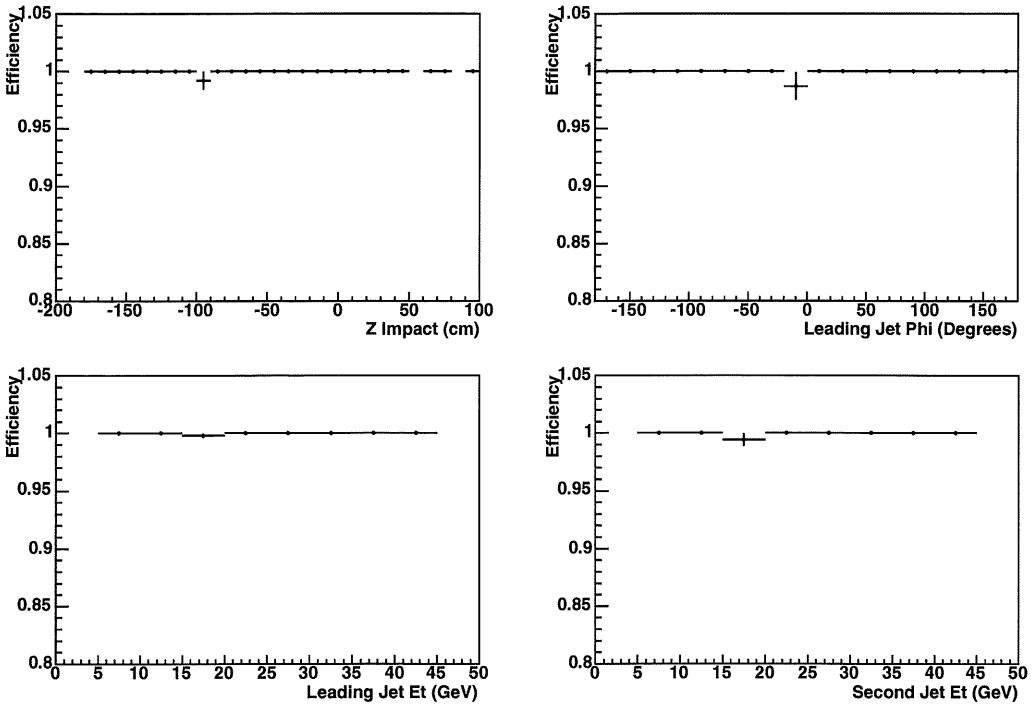

Figure 4.1: *Trigger efficiencies for the dijet event sample. Efficiencies are for the subtrigger combination (S67 || S75 || S77) vs positron Z impact (top left), leading jet azimuthal angle (top right), leading jet E_T (bottom left) and second jet E_T (bottom right). In this work, || represents a logical OR operation.*

was checked using the DIS sample of events used in this work for both of the event simulations employed (see figure 4.2 (top left)).

The hadronic calibration is carried out in a similar way, using the transverse momentum of the calibrated electron, P_{Te}, and the transverse momentum of the hadronic final state, P_{Th}. The ratio of these values, known as the P_T *balance*, is expected to be distributed around unity for NC DIS events. Calibration constants are introduced to bring the P_T balance into agreement with simulated events. The calibration is performed on a wheel-by-wheel basis and introduced as a function of γ (the polar angle of the hadronic final state). The ratio of P_T determined from the hadronic final state and from the double-angle method is a further measure of the calibration, whilst the balance of

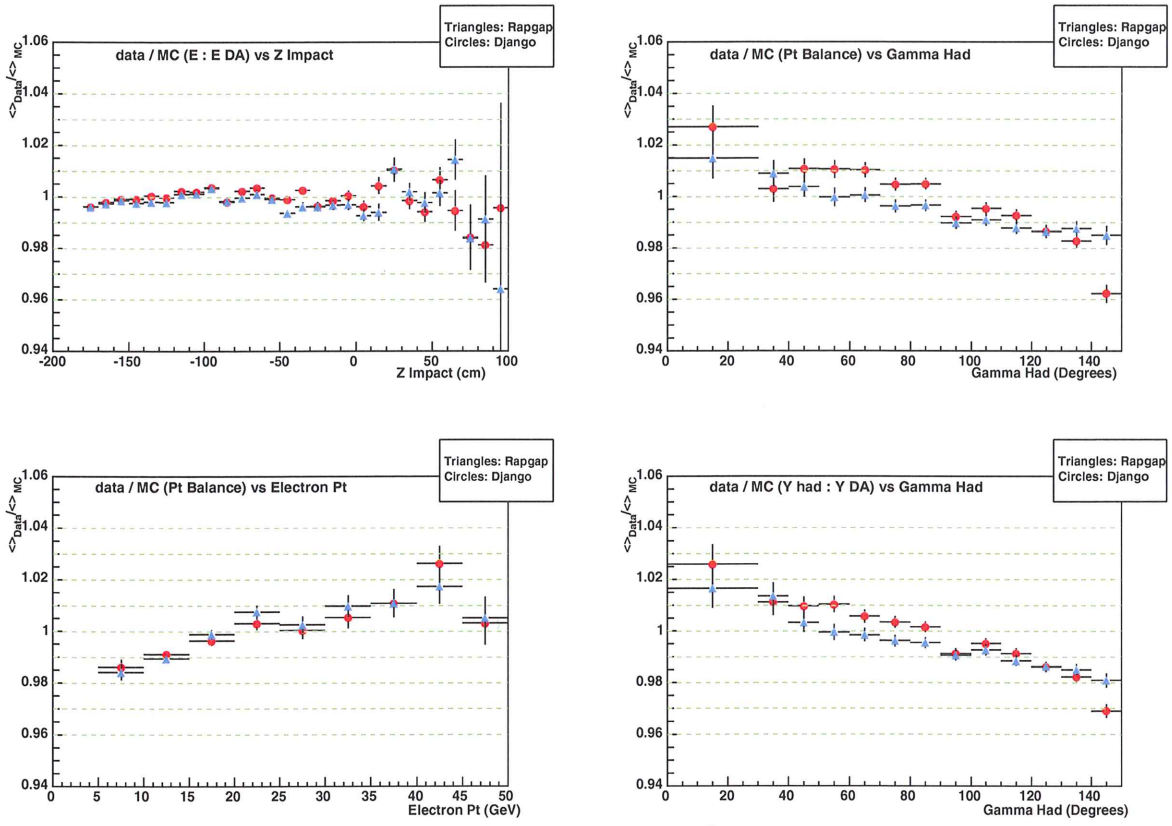

Figure 4.2: *Demonstration of calibration. Plots show double ratios (data / MC) for Electron energy ($E_{e-sigma}/E_{DA}$) vs Z impact (top left), P_T balance vs γ_{Had} (top right), P_T balance vs scattered electron P_T (bottom left) and y balance vs γ_{Had} (bottom right).*

the inelasticity, y, is also employed in a similar ratio. The agreement with simulated events for the entire determination of the hadronic energy (based on contributions from the LAr, SPACAL and tracks) was found to be 2% overall. This calibration was checked using the DIS sample of events used in this work for both of the event simulations, as illustrated in figures 4.2 and 4.3. It can be seen that the calibration is accurate over a wide range in the variables studied. It appears to be better than the quoted value of 2% for all but very backward hadronic activity and as such the systematic error associated with this uncertainty in this work is likely to be an overestimation.

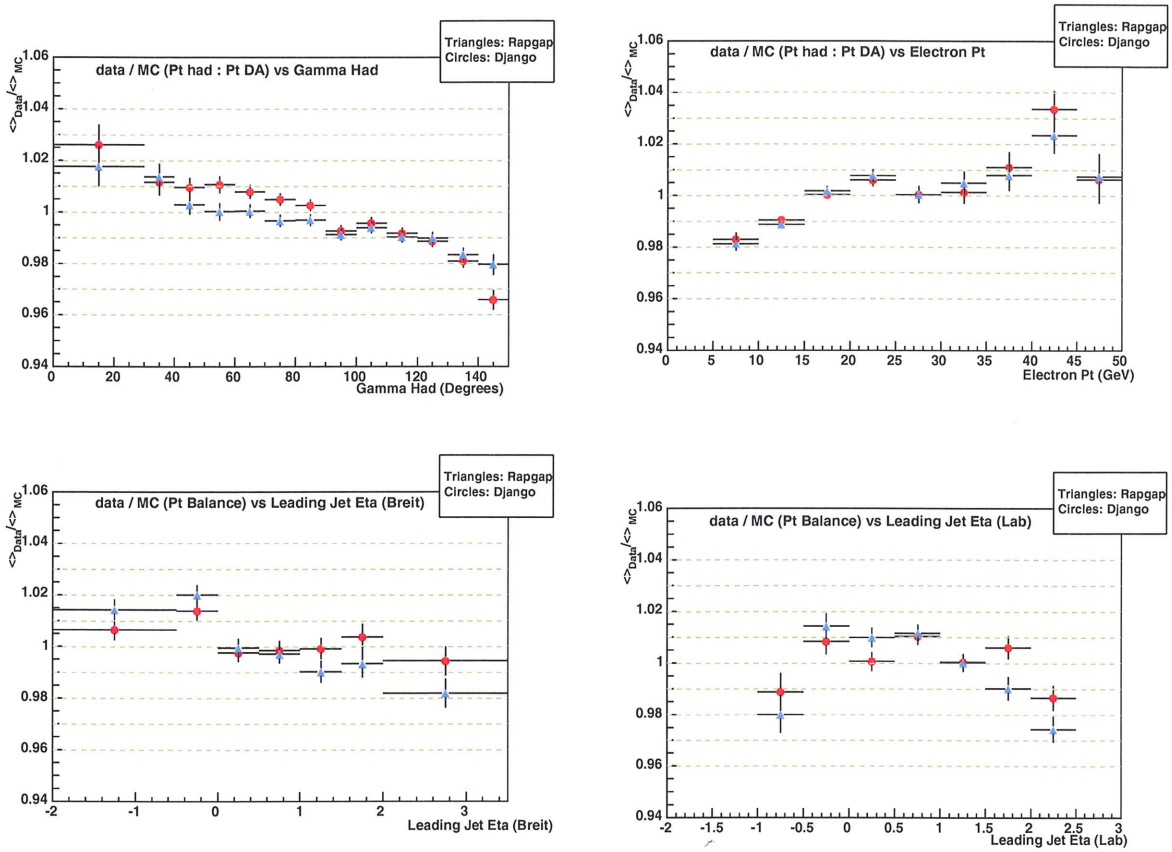

Figure 4.3: *Demonstration of calibration. Plots show double ratios (data / MC) for P_T ratio vs γ_{Had} (top left), P_T ratio vs scattered electron P_T (top right), P_T balance vs leading jet η in the Breit frame (bottom left) and P_T balance vs leading jet η in the lab frame (bottom right).*

4.3.2 DIS Control Distributions

The following distributions demonstrate that effectiveness of the DIS selection criteria described above. All distributions are well described by the models RAPGAP and DJANGO. This indicates that both the physics and the geometry of the H1 detector have been understood and well described.

Figure 4.4 shows the kinematic variables Q^2 and y, which represent the virtuality of the exchanged vector boson in the DIS event and the relative energy of the electron transferred to the proton respectively. This work is concerned

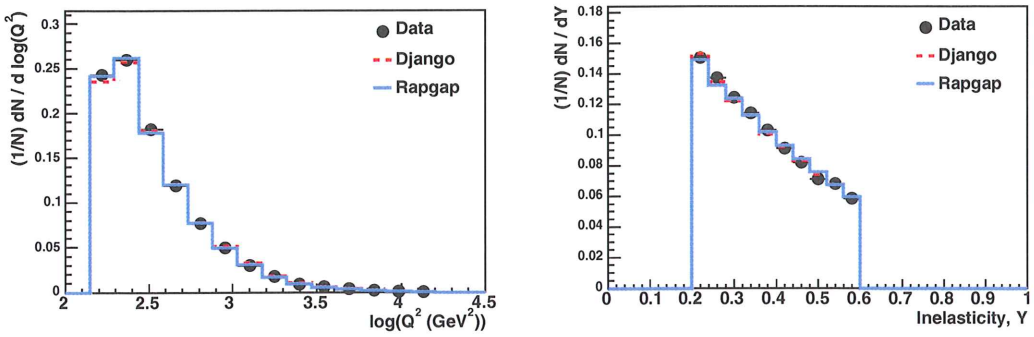

Figure 4.4: *The Q^2 (left) and inelasticity, y (right) for the DIS event sample. A cut is present at $y = 0.6$*

with values of Q^2 that are considered to be very high, that is above 150 GeV^2. Due to detector acceptance, the peak of this distribution is around 316 GeV^2. The inelasticity distribution is almost linear with a differential coefficient of ~ -0.23. In approximately 13% of events, 50% or more of the incident electron energy is transfered to the proton. The accurate reconstruction of the neutral current event topology requires the presence of a high energy electron in the final state. For this reason, and because a photoproduction event misidentified as a NC DIS event due to a hadronic energy deposit near the forward beam pipe being incorrectly flagged as an electron will have a high value of y, events with values of y above 0.6 are not considered.

Figure 4.5 shows the energy spectrum for the scattered electron, E', in the DIS event sample, along with the polar angle. The energy spectrum demonstrates the inelastic nature of the collisions concerned. The spectrum for an elastic collision is expected to be a Gaussian distributed around the initial energy of the projectile (in this case a 27.6 GeV electron). The left side of the distribution shown here indicates that the target (proton) contains hard scattering centres, which are point-like at the resolution available at HERA. The θ distribution emphasizes this idea - recall the original Rutherford scattering results in figure 1.2. The distribution is brought into a peak due to the kine-

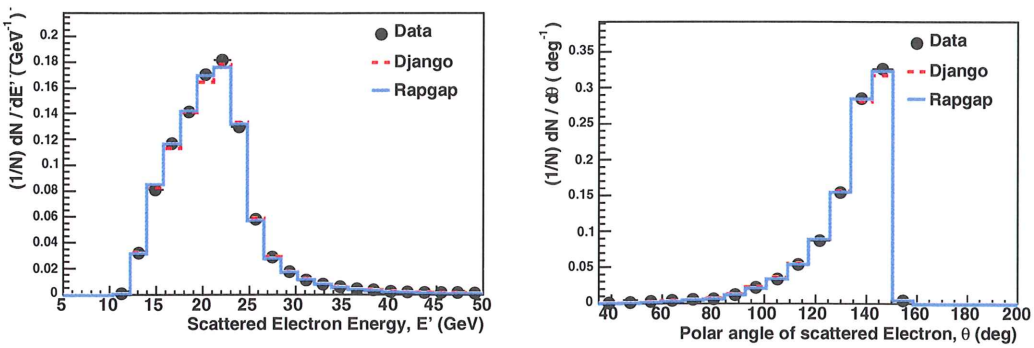

Figure 4.5: *The scattered electron energy spectrum (left) and polar angle θ (right) for the DIS event sample.*

matic range considered in this work and also because of limitations in detector acceptance. The initial state electron enters the H1 detector along $\theta = 180°$ so the scattering angle can be found by the expression $\theta_{scat} = 180° - \theta$. The requirement of high virtuality for the events considered in this work ensures that $\theta_{scat} > 40°$ and that for $\sim 5\%$ of events the electron is scattered through an angle greater than 90° - backwards relative to its incident direction.

Figure 4.6 shows the nominal z position of the primary interaction vertex and the Björken x distribution. The z vertex distribution is as expected for inelastic ep collisions - that is, a Gaussian distribution about the nominal interaction point, which was at $z = 5.6$ cm for the running periods considered here. The models used are reweighted in this distribution so that a good description is assured. The x_{Bj} distribution shows the kinematic reach of this work, with values as low as 10^{-3} being observed. Almost the whole distribution occurs below the valence region ($\log(\ x_{Bj}\ ) \sim -0.48$) indicating that, in this work, the incident electron interacts with either a sea quark or a gluon (via boson-gluon fusion) within the target proton more than 99% of the time. The distribution is expected to be asymptotic to log(ys) $\sim$ -4.8 from kinematic considerations, but the restrictions imposed on the phase space result in the peaked distribution shown.

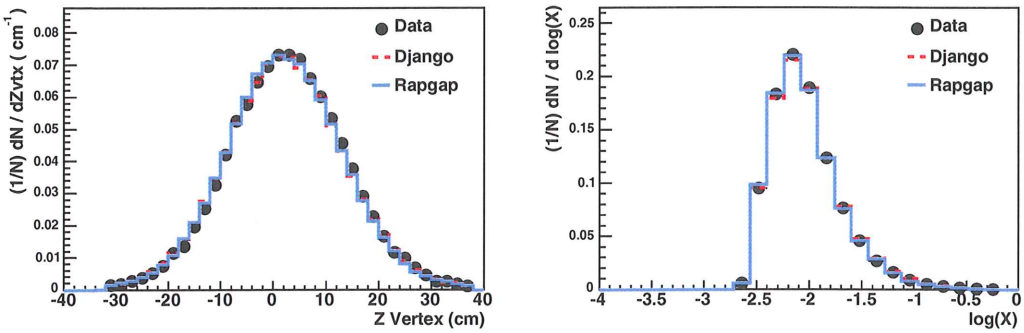

Figure 4.6: *The Z position of the primary interaction vertex (left) and the Björken x distribution (right) for the DIS event sample.*

Figure 4.7 shows the variable $E - P_z$. For a DIS collision, the sum of all $E - P_z$ is expected to peak at $2E_e$, assuming that all energy is correctly measured, as the beam proton remnant can be neglected due to its small forward angle. Deviations from this value occur due to particles escaping down the backward beampipe, photons radiated collinearly to the initial state electron and measurement inaccuracies. The sum of $E - P_z$ is reduced by twice the energy lost in the backward direction. This means that the cut imposed causes the total effect of such losses to be no greater than 5 GeV per event. The distribution can be seen to peak at 55 GeV as expected, with no more than 2% of events having the maximum allowed backward energy losses. This cut also helps remove photoproduction events because, for an event in which the scattered electron escapes undetected, the value of $E - P_z$ is reduced by twice the energy of the scattered electron, E'.

Figure 4.8 shows the influence of some of the geometric features of the H1 detector. The distribution of the z impact position shows the effect of the z-crack cut with the limited acceptance of the very backward region resulting in a peaked rather than an asymptotic distribution. This distribution is also influenced by the Q^2 cut, which results in a minimum transverse momentum of the scattered electron. The azimuthal angular distribution for the scattered

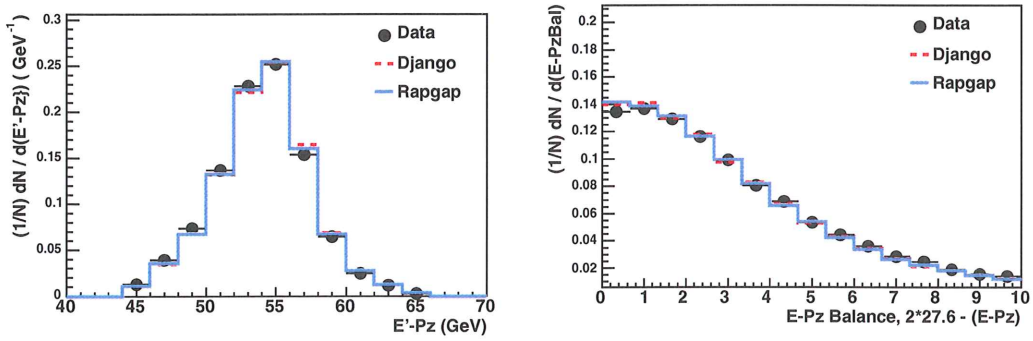

Figure 4.7: *The distribution of the variable $E - P_z$ (left) and the $E - P_z$ balance (right) for the DIS event sample.*

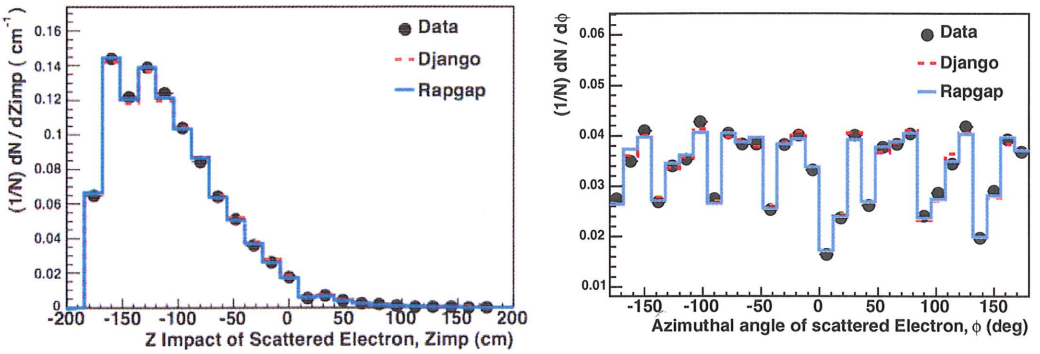

Figure 4.8: *The distribution of the z impact position (left) and the Φ distribution (right) of the scattered electron for the DIS event sample.*

electron shows the octant structure of the H1 detector with reduced acceptance around the boundaries of each segment. This distribution is expected to be flat for a perfect detector and it is this expectation of symmetry that allows the remaining data events to be reweighted to account for the losses due to the reduced acceptance at the octant boundaries.

Figure 4.9 shows the ratio of the transverse momentum, P_t, as measured from the hadronic final state and from the electron along with the angle γ. The P_t balance is peaked around one and demonstrates that the overall hadronic calibration is sound. The calibration is examined in greater detail in section 4.3.1.

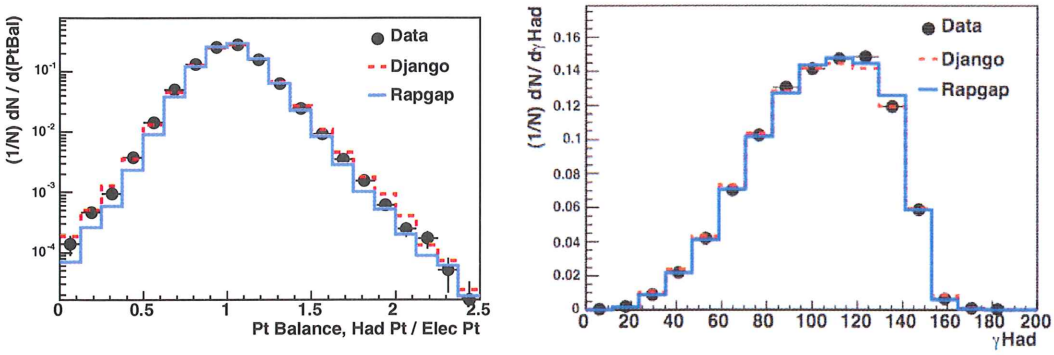

Figure 4.9: *The distribution of the P_t balance (left) and the angle γ for the hadronic final state (right) for the DIS event sample.*

The sample of DIS events selected for this work is extremely clean, with all studied variables from the electron and the hadronic final state being well described by the models RAPGAP and DJANGO. The possibility of background from photoproduction has been investigated. Such a background can occur if a particle from the hadronic final state is misidenitified as a positron. An estimation of this background has been made using events simulated by the photoproduction event generator PYTHIA. The contribution after the cuts described above is extremely small, such that it is not meaningful to perform any statistical subtraction. The effect of this background is considered to be negligible.

The events of the DIS sample are sufficiently well described to cluster the hadronic final state into jets and examine the properties of events featuring a multijet final state.

4.4 Jet Search

The inclusive $k_\perp$-cluster algorithm was used to reconstruct jets in both data and simulated events. The algorithm is defined by a radius parameter R_o, which defines the minimal separation of jets in pseudorapidity and azimuth

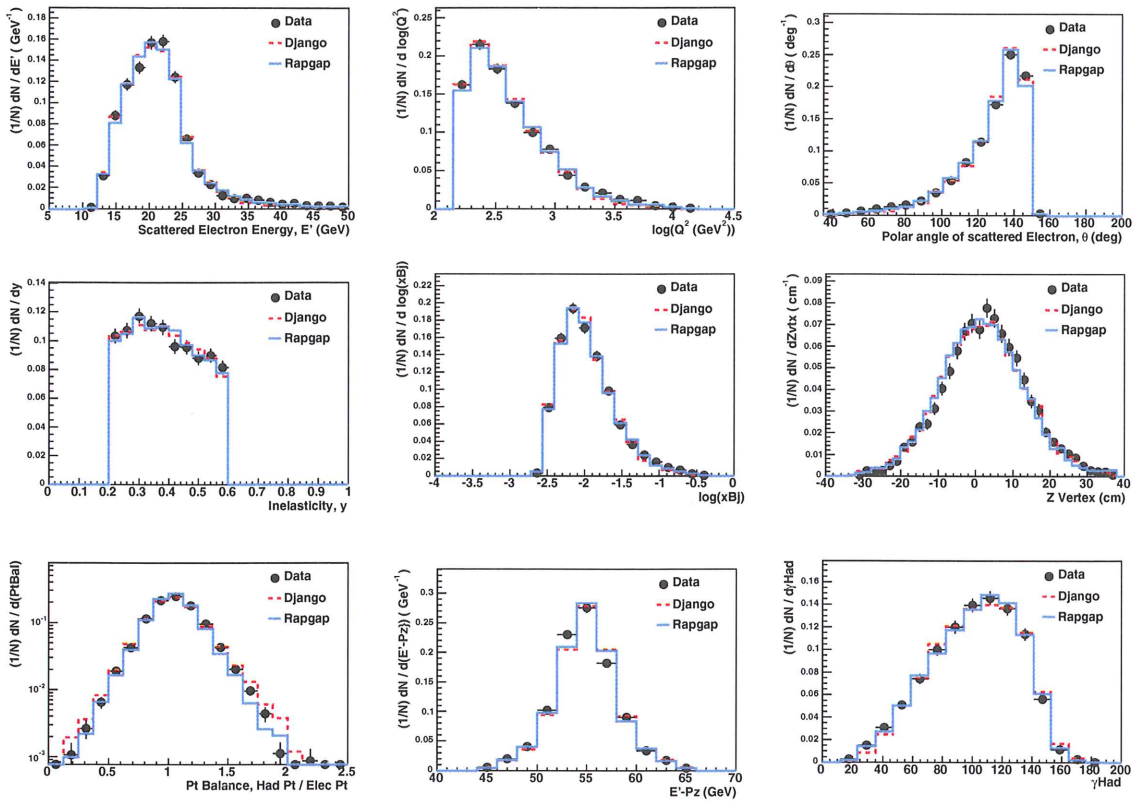

Figure 4.10: *Shape comparisons of data and simulations for kinematic and hadronic distributions of the dijet sample. Variables shown are those already described for the DIS sample in the previous section. In these plots N = number of dijet events.*

space. R_o was set to unity, as in [40]. A complete description of the inclusive $k_\perp$-clustering algorithm can be found in section 3.4.1 and in [6, 40].

The concept of a jet is rather arbitrary and it only has meaning if rigorously defined. The $k_\perp$ cluster algorithm will produce jets down to a given low transverse momentum cut-off. It is not considered that very soft hadronic final state clusters are true jets, as they may consist of little more than one particle. For this analysis, the minimum transverse momentum considered by the $k_\perp$ algorithm is 4 GeV although only jets with $E_T > 5$ GeV are considered for the jet cross section measurements, the difference allowing for some smearing due to non-perfect jet energy resolution. Four-vectors of jets in the Breit frame are

then boosted back to the laboratory frame where their pseudorapidity must fall within the range $-1 < \eta^{jet}_{Lab} < 2.5$. Jets that satisfy both of these criteria are referred to as *good* jets. In order to increase the stability of the NLO calculations, events considered for the trijet (dijet) cross section are included only if the three (two) jets of highest E_T have an invariant mass $M_{3jet} > 25GeV$ ($M_{2jet} > 25GeV$). The invarient mass is found by taking the sum of the four-vectors of the three (two) highest E_T (leading) jets and the scalar product of the resulting four-vector taken with itself. The invarient mass requirement introduces a non-complete overlap of the jet samples that allows some error cancellation and also an increase in sensitivity to α_s for $R_{3/2}$.

In this document the proton remnant is not included in the jet count and is neglected. After all cuts have been made, a total of 5032 dijet events and 1586 trijet events remained.

4.4.1 Dijet Control Distributions

After clustering the hadronic final state of the DIS sample events into jets, the total number of events that remain (those that pass the dijet selection criteria) is greatly reduced. Thus it is important to check if the events that make up the dijet subsample are well described in terms of their kinematics and the specifics of the H1 detector. Some of the distributions examined for the DIS sample are given for the dijet sample in figure 4.10. The Q^2 distibution for the jet sample is reweighted by a small amount to provide better agreement at very high values (RAPGAP) and medium values (DJANGO). Besides this small effect, there are no specific problems, with all distributions being well described by both models, within statistical uncertainties, following the reweight. The robustness of the reweight was checked by varying the kinematic cuts and the jet definitions. The models described the data equally well under these circumstances showing that the small Q^2 reweight is acceptable and independent of arbitrary event sample definitions.

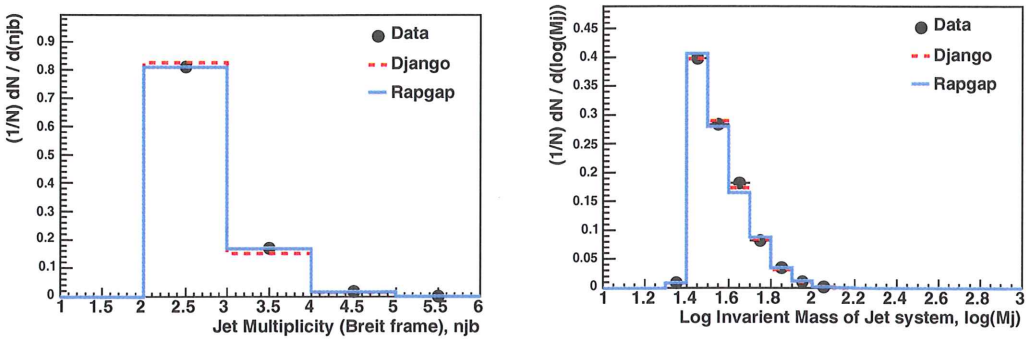

Figure 4.11: *Shape comparison of data to simulations for the jet multiplicity (left) and invariant mass (right) distributions for dijets in the Breit frame. In these plots N = number of dijet events.*

Figure 4.11 shows the output of the $k_\perp$-cluster algorithm for the hadronic final state in the Breit frame for events with two or more jets that pass the jet phase space selection criteria. The number of jets is correctly predicted by both models indicating that the description of the topology of the hadronic final state by these models is consistent with the data. The distribution of the invariant mass of the dijet system is also well described. Here the four-vectors of the two highest E_T (leading) jets are summed and the scalar product of the resulting four-vector taken with itself.

Figure 4.12 shows the transverse energy spectra for the leading and next-to-leading jets in the dijet sample. Both distributions are well described by both MC models, giving further evidence that the hadronic final state is well understood. The E_T distributions are expected to be asymmptotic at low values, but the distributions are modified by the phase space cut made on the invariant masses. Both distributions peak at around 15 GeV, but the differential coefficient for the second jet is much larger than for the leading jet, meaning that the distribution falls away more quickly to the right of the peak. Values of E_T are as high as 60 GeV for the leading jet, but no next-to-leading

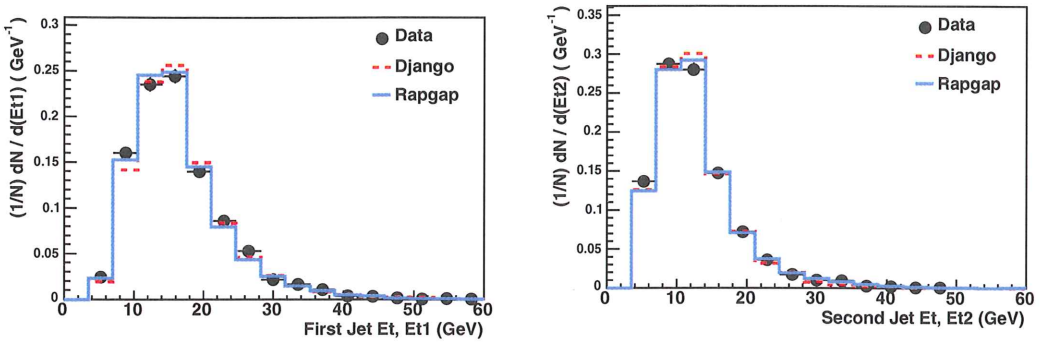

Figure 4.12: *Shape comparison of data to simulations for the transverse energy spectra for the leading (left) and next-to-leading (right) jets for dijet events in the Breit frame. In these plots N = number of dijet events.*

jet has an E_T larger than 50 GeV.

Figure 4.13 shows further that the hadronic final state is well modelled, to the extent that the clustering procedure produces jets for simulated events that have the same transverse energy relationship as those in the data. The fractional difference in transverse energy consists of the difference in transverse energy for the leading and next-to-leading jets, as a fraction of the E_T of the leading jet. It can be seen that, for nearly 50% of events, the difference in E_T between the two leading jets is less than 20%. As, at leading order in the Breit frame, jet pairs are produced with equal transverse energy, this distribution is expected. The remainder of the distribution occurs due to higher order effects. The accuracy with which this distribution is modelled demonstrates the efficacy of the higher order approximation methods for the region of phase space considered in this work. The relationship between the hard scales $\overline{E_T}^2$ and Q^2 shows that the choice of Q^2 as the QCD scale for the theoretical predictions used in this work is justified. The comparison with $\overline{E_T}^2$ shows that in $\sim$ 86% of events, Q^2 is the harder scale.

Figure 4.14 shows the distributions of pseudorapidity in the laboratory frame

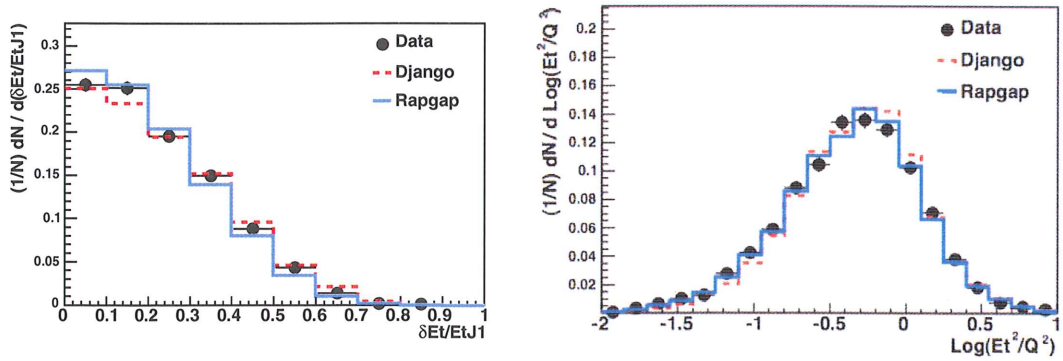

Figure 4.13: *Shape comparison of data to simulations for the fractional difference in E_T (left) and comparison of $\overline{E_T}^2$ (right) to Q^2 for dijet events in the Breit frame. In these plots N = number of dijet events.*

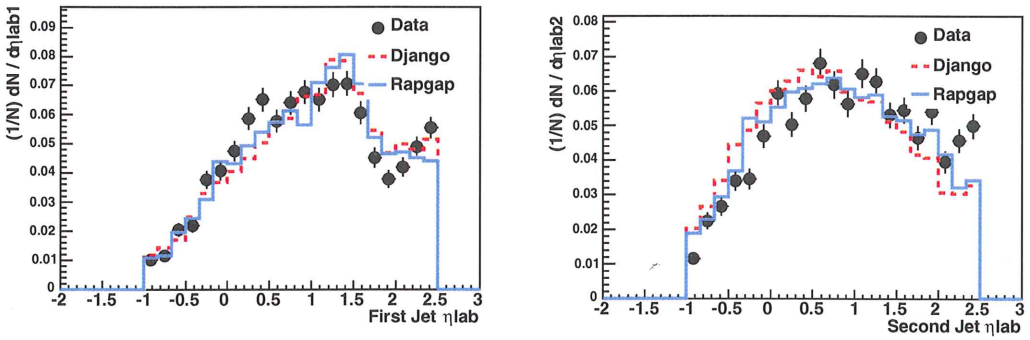

Figure 4.14: *Shape comparison of data to simulations for the pseudorapidity, η, distributions for the leading (left) and next-to-leading (right) jets in the laboratory frame for dijet events. In these plots N = number of dijet events.*

for the leading and next-to-leading jets in the Breit frame. The four-vectors for the jets in the Breit frame are boosted to the laboratory frame for this measurement. The distribution for the leading jet shows good agreement with simulation as does the next-to-leading jet in all but the most forward region. Even here, agreement is not unacceptable. The disagreement may be due to several factors including a weakness in modelling very forward jets. It can be seen that there are fewer jets in the backward region than for all other regions of the detector. This is partly due to the inelasticity cut imposed on the event sample.

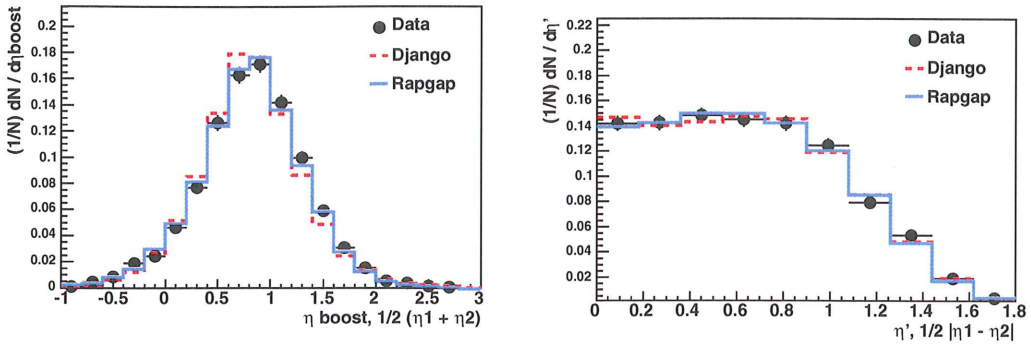

Figure 4.15: *Shape comparison of data to simulations for the η-Boost, (left) and $\eta\prime$ (right) distributions for dijet events. In these plots N = number of dijet events.*

Figure 4.15 shows the variables η-Boost and $\eta\prime$, which are composed from the sum and the difference of the pseudorapidities of the two leading jets in the Breit frame. η-Boost demonstrates the effect of the approximate longitudinal boost that distinguishes the Breit frame from the dijet centre of mass frame. The distribution is peaked around η-Boost ~ 0.9 indicating that the Breit frame is typically shifted by this quantity in pseudorapidity from the dijet centre of mass frame. The distribution is not quite symmetric, with a small tendency for the Breit frame to be shifted by an amount smaller than this peak value. $\eta\prime$ reflects, at leading order, the angular distribution of the jets in the dijet centre of mass frame. The distribution is relatively flat until around $\eta\prime \sim 1$ where the distribution drops off due to the transverse energy cuts.

Figure 4.16 shows the Breit frame pseudorapidity for all jets in the final state. The distribution indicates that jets are primarily produced in the target region of the Breit frame (positive pseudorapidity). At leading order, in the special case where all final state partons are contained within the leading two jets, the centre of mass energy is equal to the invariant mass M_{jj}. This means that the variable $\xi = x_{Bj}(1 + \frac{M_{jj}^2}{Q^2})$ represents an approximation to the proton

momentum fraction carried by the struck parton.

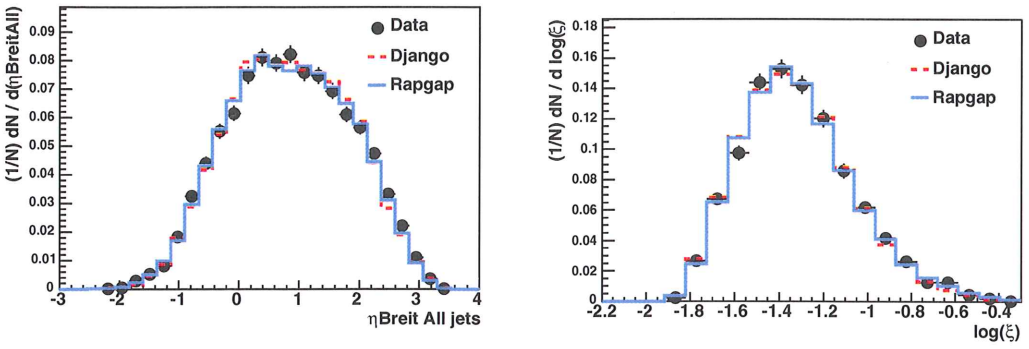

Figure 4.16: *Shape comparison of data to simulations for the η-Breit, (left) and ξ (right) distributions for dijet events. In these plots N = number of dijet events.*

4.4.2 Trijet Control Distributions

The control distributions given for the trijet event sample are almost identical to those for the dijet sample and so they are presented in a briefer fasion. It is somewhat remarkable that the data (particularly the jet transverse energy and angular distributions) are still well described by the simulations. No terms for producing trijet events are present in the LO QCD matrix elements in the simulations and so all information with regards to a third jet must be derived from the parton shower or colour dipole models (RAPGAP and DJANGO respectively) used to approximate higher order processes. Even the number of very high multiplicity jets is well simulated, indicating that the approximate methods employed are well justified and may one day provide an alternative method to more fully understand the nature of the strong force.

The kinematic variables relating to the electron and the general hadronic final

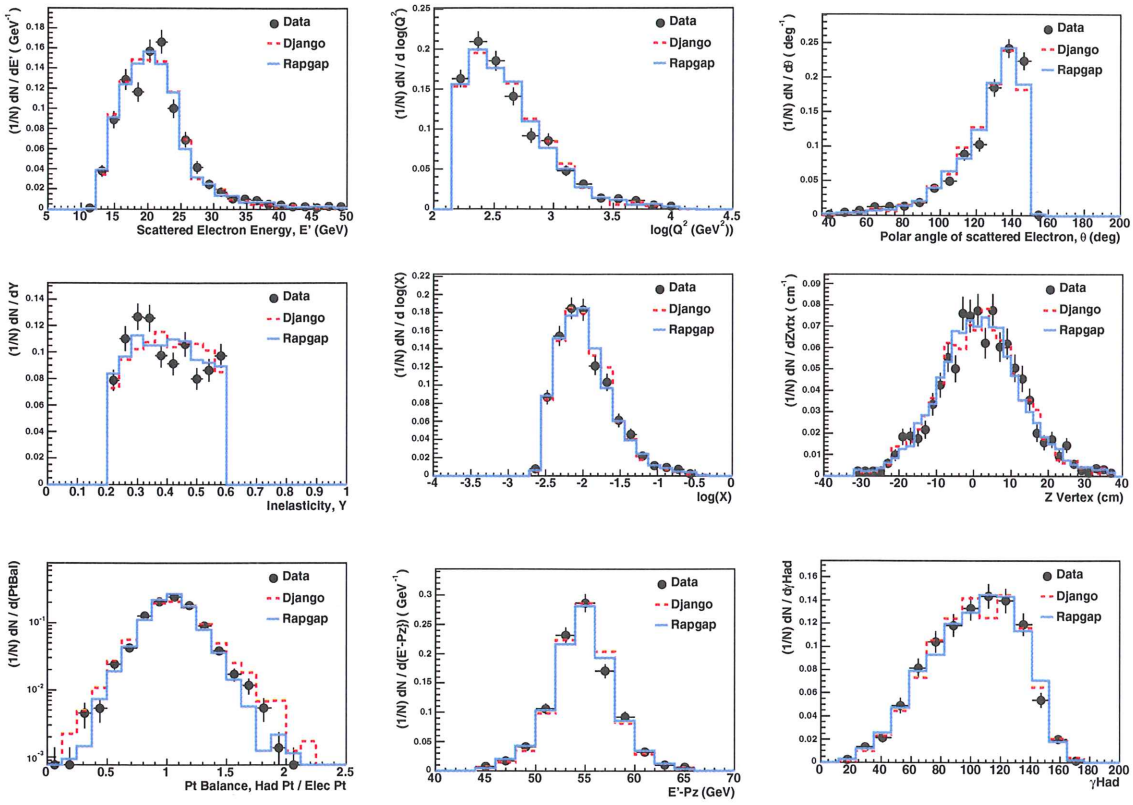

Figure 4.17: *Shape comparison of data to simulations for the kinematic and hadronic distributions of the trijet sample. Variables shown are those already described for the DIS sample in the previous section. In these plots N = number of trijet events.*

state are shown in figure 4.17 and are well described, although, as for the dijet sample, a small reweight in Q^2 is required to improve the overall description. The possibility of a bias introduced by the reweight is ruled out using the same method as for the dijet sample and it is once more confirmed to be stable. The total event sample is much smaller than even the dijet sample and so statistical uncertainties are larger. The data and the simulations are in agreement within these uncertainties.

The distributions pertaining to the jets within the sample are given in figure 4.18. Some points of interest between the dijet and the trijet sample are evident. The invariant mass of the jet system is broader for the trijet sample

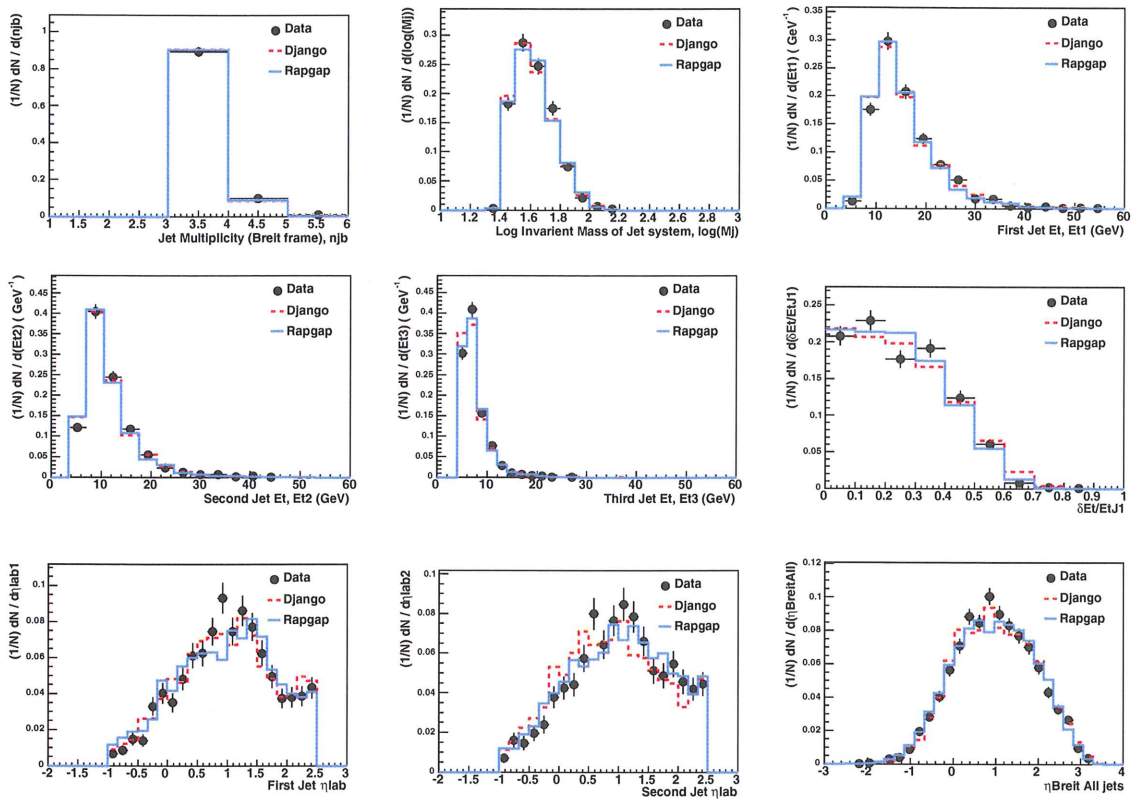

Figure 4.18: *Shape comparison of data to simulations for the jet variables of the trijet sample. Variables shown are those already described for the dijet sample in the previous section. In these plots, N = number of trijet events.*

due to the inclusion of the third jet. The transverse energy distributions for the leading and next-to-leading jets are narrower for the trijet sample and have lower maximum values. The transverse energy distribution for the third jet is very steeply falling, indicating that the third jet in events in the trijet sample often does not carry a large quantity of the total hadronic transverse energy. The distributions of pseudorapidity in the laboratory frame for the two leading jets are similar in both samples, with jets tending to be produced in the forward region of the detector.

The total sample of events considered consists of well modelled DIS events. From these events, a further two sub-samples are produced based on the con-

figuration of the hadronic final state. Events that pass the dijet or trijet phase space requirements are also well described for all distributions examined. The excellent agreement between data and the two different simulations indicates that the jet samples are acceptable for further analysis leading to the jet production cross-sections required to form $R_{3/2}$. The increased quantity of data provides reduced statistical uncertainties and allows for a superior description of the trijet event variables than that previously obtained by H1 [6, 7].

Chapter 5

The Analysis

"Solve et Coagula" - Paracelcus

The previous sections have shown that the high quality data collected by the H1 detector is well described by simulation. This section details the analytical procedure undertaken to produce the cross-sections required for the QCD study.

5.1 Unfolding the Data

5.1.1 Bin Selection

The binning for the cross-sections that will go into the calculation of $R_{3/2}$ was chosen to ensure a roughly equal number of events for each bin that is to be included in the QCD analysis. Whilst the dijet sample contains sufficient events to allow for finer binning, the scarcity of trijet events, particularly in the higher Q^2 regions, imposes stricter limits for the bin widths. The bins used are given in table 5.1 below.

The bins are wider than those used for the previous measurement of the dijet cross-section at H1 and so, whilst fewer measurements are made, the results from this work are of significantly higher statistical precision. The binning for

Bin Number	Q^2 Range (GeV^2)
1	150 - 220
2	220 - 350
3	350 - 700
4	700 - 5000
5	5000 - 15000

Table 5.1: *Q^2 binning for the dijet and trijet cross-sections.*

the trijet sample is the same as that previously employed at H1 as, although this work is based on twice the integrated luminosity, it was felt that the statistical precision for the trijet cross-section was unacceptably low when finer binning was tested. As the calculation of $R_{3/2}$ requires the specifications for the dijet and trijet cross-section measurements to be as similar as possible, the binning for the dijet cross-section is chosen to be equal to that of the trijet cross-section.

5.1.2 Correction Factors

The effect on the data of limited detector acceptance and resolution as well as inefficiencies in the selection is accounted for by the correction factors that are applied to the multijet cross-sections. These are shown, as a function of Q^2, for both the dijet and trijet samples in figure 5.1.

The correction factors for detector effects are found using the event simulations described in chapter 3. A sample of DIS events is generated for each simulation. These are events as expected from pure physics consideration of ep collisions and are refered to as the *generator* level events. The number of events in each Q^2 bin (N_{GEN}) is determined. The same events are then subjected to a detailed simulation of the H1 detector. The effects of H1 on the events (e.g. on tracks, energy deposits) are determined and the same reconstruction software employed for the real data is used to reconstruct the kinematics of

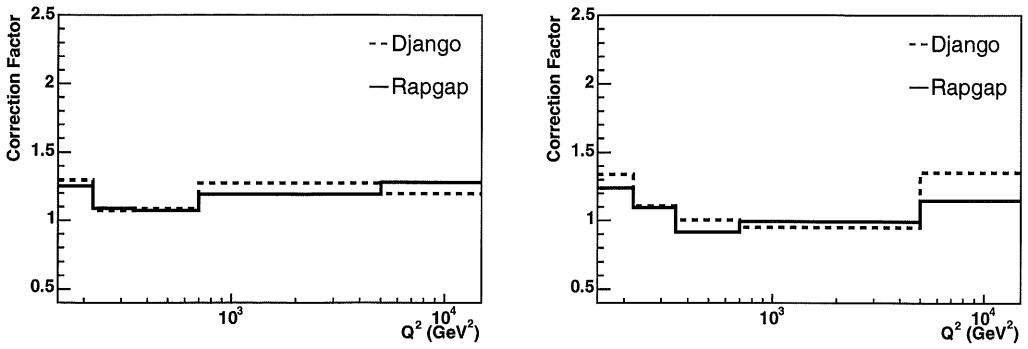

Figure 5.1: *Detector correction factors vs Q^2 for dijet (left) and trijet (right) event samples. Five times as many simulated events as data events were considered and as such, errors are considered to be negligible.*

the simulated events. These are known as the *reconstructed* level events and the number of events in each Q^2 bin (N_{REC}) is determined. The reconstructed level events are those compared with the data in the previous chapter. If the reconstructed simulated events describe the data as measured by the H1 detector, the procedure for correcting for detector effects is as follows.

It is known how many events were considered (N_{GEN}) and how many events are detected by H1 (N_{REC}). The acceptance, A is then given by

$$A = \frac{N_{REC}}{N_{GEN}} \quad , \tag{5.1}$$

where A represents the total acceptance of the H1 detector. As the calculated cross-section must be divided by this acceptance, the correction factor can be thought of as $\frac{1}{A}$.

Two other variables are also considered that help provide an indication of the suitability of the event simulations for correcting the data. These are known as *purity* and *stability*. They are defined by considering the number of events that are in the same bin at both the reconstructed and generator level, N_{STAY},

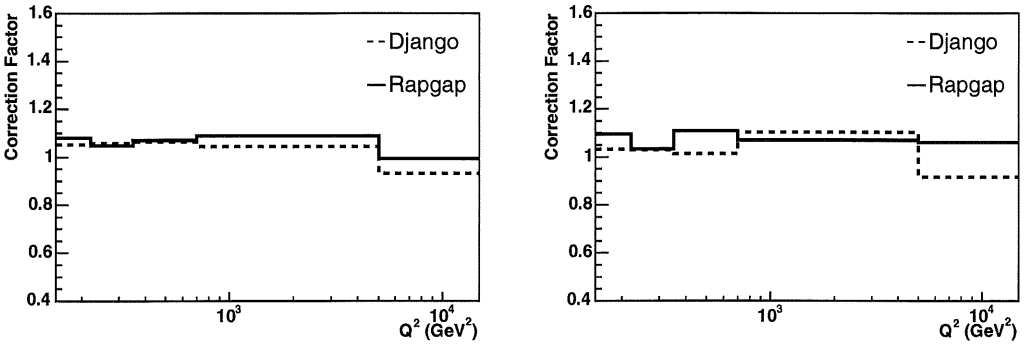

Figure 5.2: *QED correction factors vs Q^2 for dijet (left) and trijet (right) event samples.*

and the number of events that are smeared out of the phase space defining the bin in the detection and reconstruction procedure, N_{LOST}. The purity and stability are then defined as:

$$Purity = \frac{N_{STAY}}{N_{REC}} \qquad Stability = \frac{N_{STAY}}{N_{GEN} - N_{LOST}} . \tag{5.2}$$

Five times as many simulated events as data events were considered and as such, errors are considered to be negligible. The average purities over Q^2 for the DIS sample, the dijet sample and the trijet sample are 0.90, 0.75 and 0.60 respectively. The average stabilities for the DIS sample, the dijet sample and the trijet sample are very similar at ~ 0.95.

The previous chapter demonstrated that the simulated events from both RAPGAP and DJANGO describe the data well and there appears to be no reason to favour one simulation over the other. In the regions where the data and models disagree, the data tend to fall between the models. Thus, in order to gain a reasonable estimation of the uncertainty associated with the use of a model to correct the cross-sections, the average correction factor from RAPGAP and DJANGO is used, with the difference between the mean value and the single values being used as the resulting uncertainty.

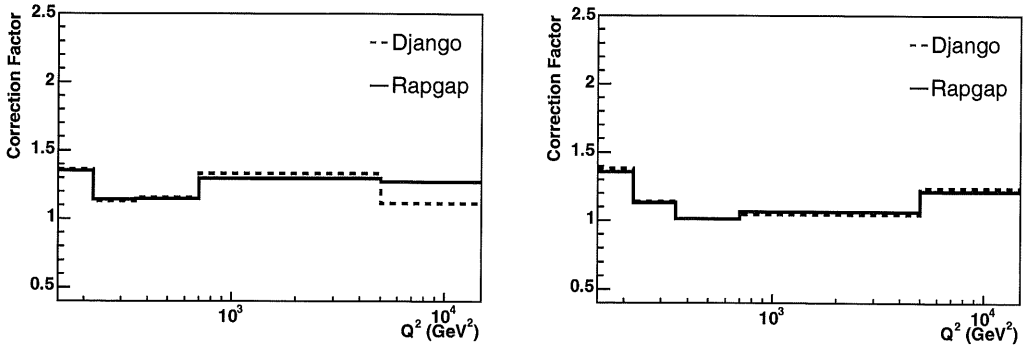

Figure 5.3: *Total correction factors vs Q^2 for dijet (left) and trijet (right) event samples.*

The effects of QED radiation are also accounted for by the use of a correction factor. The simulated events utilised for the detector corrections are used once more, but they are now compared against a set of events that are generated under identical conditions except that the effects of QED radiation are excluded. The QED correction is defined as $\frac{N_{GEN;w/o.QED}}{N_{GEN;w.QED}}$.

Figure 5.2 shows the QED correction factors for the dijet and trijet samples, as a function of Q^2. The values are on average 5% for both samples and differences between the calculations for each model are small, typically around 1%.

The overall correction factor is the product of the detector and QED radiation correction factors. The total correction factors are shown in figure 5.3 and it can be seen that, for the total correction factors, there is little difference between the two models employed for event simulation. The size of the total correction factor is reduced for the ratio $R_{3/2}$, an example of which is shown in table 5.2.

Bin	Trijets	Dijets	$R_{3/2}$
1	1.38	1.36	1.01
2	1.14	1.13	1.01

Table 5.2: *Example reductions of the total correction factor, with respect to Q^2, for the ratio $R_{3/2}$ compared with trijet and dijet events.*

5.1.3 Hadronization Corrections

Just as the effect of a particle detector can be simulated and corrected for, so too can the process of hadronization. By calculating the event rate with and without the effects of a hadronization model, the hadronization correction factor can be determined. Details of the parameters defining the partonic final state are provided in appendix B. Consider the number of events generated *with* hadronization effects divided by the number of events generated *without* hadronization effects:

$$C_{HAD} = \frac{N_{HADRON}}{N_{PARTON}} \quad , \quad \delta_{HAD} = 1 - C_{HAD} \quad . \tag{5.3}$$

In order to produce this correction factor, the events are simulated at parton level. An example of the procedure used to obtain parton level information, illustrated by an event from the generator RAPGAP, with higher order approximations from the parton-shower model, is shown in appendix B.

Hadronization corrections C_{HAD} can be seen in figure 5.4. Values from DJANGO (dashed line) and RAPGAP (full line) are in close agreement for dijets, but differ by up to 8% for trijets due to the different parton cascade models employed. Following the conclusions reached in [12], the average C_{HAD} of both models is used to correct the parton level NLO cross-sections in this analysis with the associated theoretical uncertainty being half the difference between the models. The hadronization correction factors were typically ~ 0.93 for

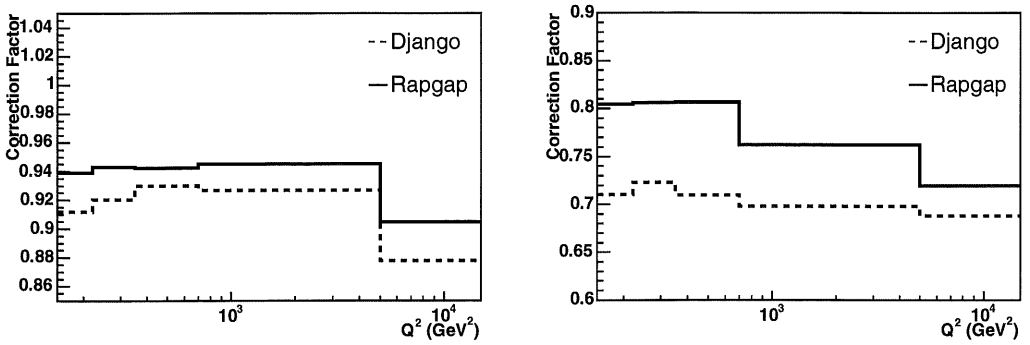

Figure 5.4: *Hadronization correction factors vs Q^2 for dijet (left) and trijet (right) event samples.*

dijets and ~ 0.75 for trijets (figure 5.4 as well as tables A.1 and A.2).

5.2 Systematic and Theoretical Uncertainties

"It 'aint so much the things we don't know that get us in trouble - it's the things we know that 'aint so." - Artemus Ward

The effect of several sources of systematic uncertainties are considered. They are given below, along with the typical change of the cross-sections [dijet; trijet]:

- The calibration of the positron energy in the LAr is varied by $\pm 0.7...3\%$, depending on the position of the positron within the detector (figure 4.2) [1%; 2%].
- The positron polar angle is varied by $\pm$ 1...3 mrad, depending on the position of the positron within the detector [0.5%; 1%].
- The positron azimuthal angle is varied by $\pm$ 3 mrad [$< 0.5\%$; $< 0.5\%$].
- A simultaneous shift of the hadronic energy scale of the LAr calorimeter ($\pm 2\%$), the track momenta of the hadronic final state ($\pm 3\%$) and

the hadronic energy scale of the SPACAL ($\pm 5\%$), producing an overall hadronic uncertainty of $\sim \pm 2\%$ (figures 4.2 and 4.3) [2%; 2%].

- The difference between using the average correction factor and that of DJANGO or RAPGAP alone as well as the effect of the small reweight in Q^2, as an estimate of the model uncertainty [1.5%; 2%].

- The uncertainty due to the measurement of the luminosity is also considered [1.02%; 1.02%].

The systematic uncertainties are combined in quadrature with the statistical uncertainties of the data and the correction function to produce a total estimation of the error on the measurement of the cross-sections.

The main contributions to the uncertainty associated with the theoretical cross-section predictions are:

- Uncertainties due to the hadronization correction factor, estimated as the difference between using the average correction factor and that of DJANGO or RAPGAP alone [1%; 4%].

- Uncertainties due to terms beyond NLO and the choice of scale are estimated by varying the renormalization scale squared and factorisation scale squared simultaneously by a factor of four [3% ; 10%].

The total theoretical uncertainty was obtained by adding the individual contributions in quadrature.

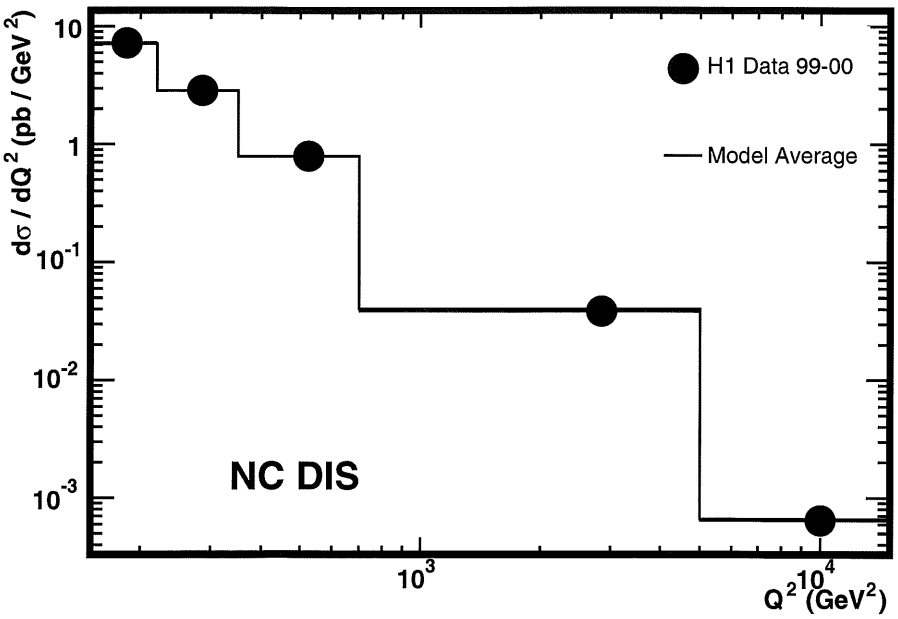

Figure 5.5: *NC DIS differential cross-section as a function of Q^2 compared with average of RAPGAP and DJANGO predictions. Errors are not visible on the scale shown.*

5.3 Cross-Sections

The differential cross-section with respect to Q^2 for NC DIS is measured and compared with the average of the models RAPGAP and DJANGO in figure 5.5. Agreement within 1% is observed, over two orders of magnitude in Q^2 and five orders of magnitude for the cross-section. This result contains no jet selections. This is not intended as a full analysis of the NC DIS cross-section, a more detailed measurement of which has been made by H1 [67].

The values for the inclusive dijet and trijet cross-sections, shown in figure 5.6 as a function of Q^2, are in good agreement with published measurements [6, 7], with slight differences due to the increase in the HERA beam energy. All results are consistent with previous measurements within the quoted un-

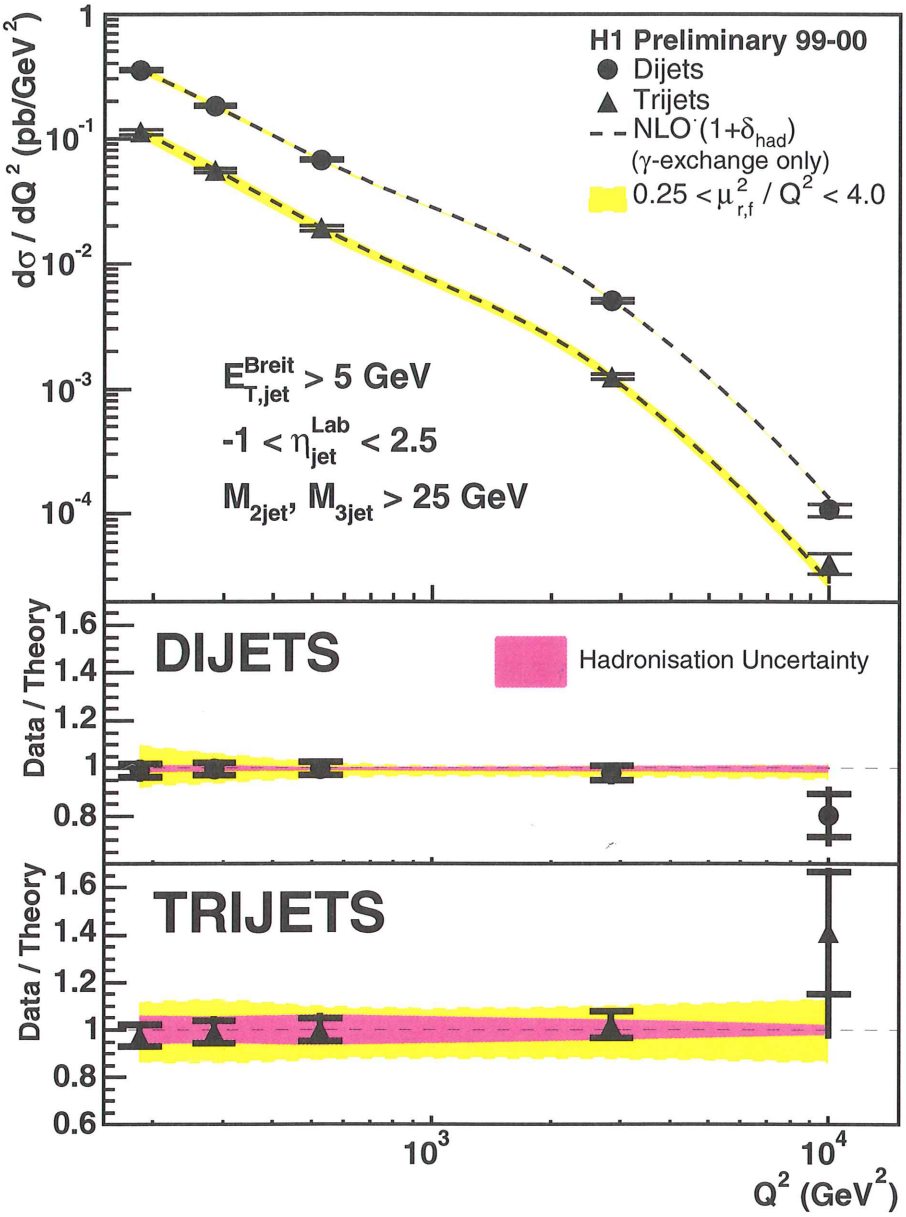

Figure 5.6: *NC dijet and trijet differential cross-sections, with respect to Q^2, shown with NLO pQCD predictions including hadronization corrections. The scale uncertainty is shown as a light shaded band and the hadronization uncertainty as a dark shaded band. Errors shown are statistical up to the horizontal bar and the quadratic sum of the statistical and experimental uncertainties thereafter.*

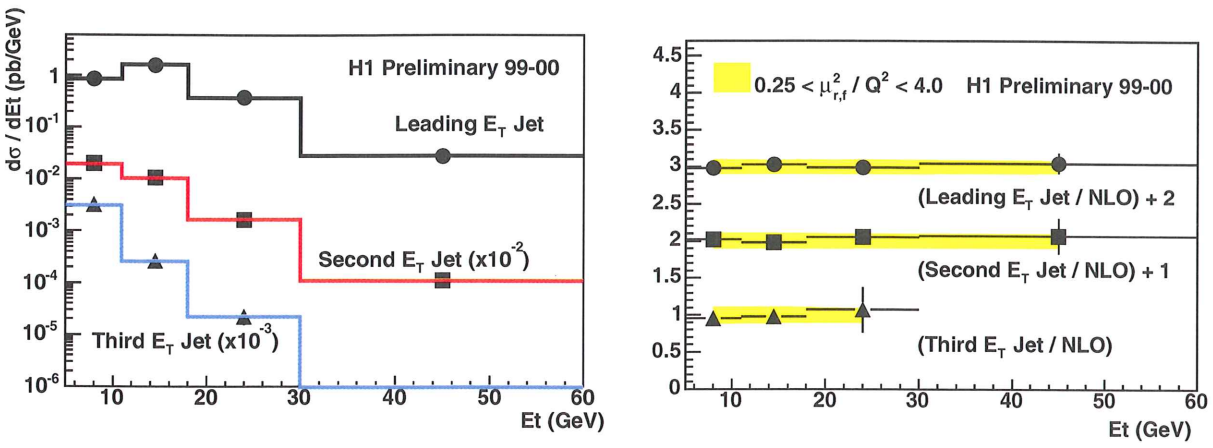

Figure 5.7: *The lefthand plot shows NC trijet differential cross-sections, with respect to E_T, with NLO pQCD predictions including hadronization corrections. The righthand plot shows the ratio of the data and theoretical values from the lefthand plot. The ratio for the leading and next-to-leading jets, with respect to E_T are translated by two and one respectively for clarity. The light shaded bands show the effect of varying the renormalization scale squared and the factorisation scale squared simultaneously by a factor of four.*

certainties, accounting for the beam energy difference. Owing to the size of the dataset employed in this study, the range of Q^2 has been extended compared with existing three jet studies[7, 2]. The highest Q^2 point has large statistical uncertainties due to the low event rate in this kinematic region, but represents the first measurement of the three jet cross-section in this kinematic region for *ep* collisions.

The cross-sections show good agreement with the predictions of NLOJET++ (corrected for hadronization effects) in the phase space region where electroweak effects can be neglected as described in an earlier section. Figure 5.6 shows both the dijet and trijet cross-sections compared to the predictions of NLO pQCD with hadronization corrections. Further detail for these measurements is shown by normalising the results from data to the theoretical expectation as shown in the bottom half of figure 5.6. It can be seen that data

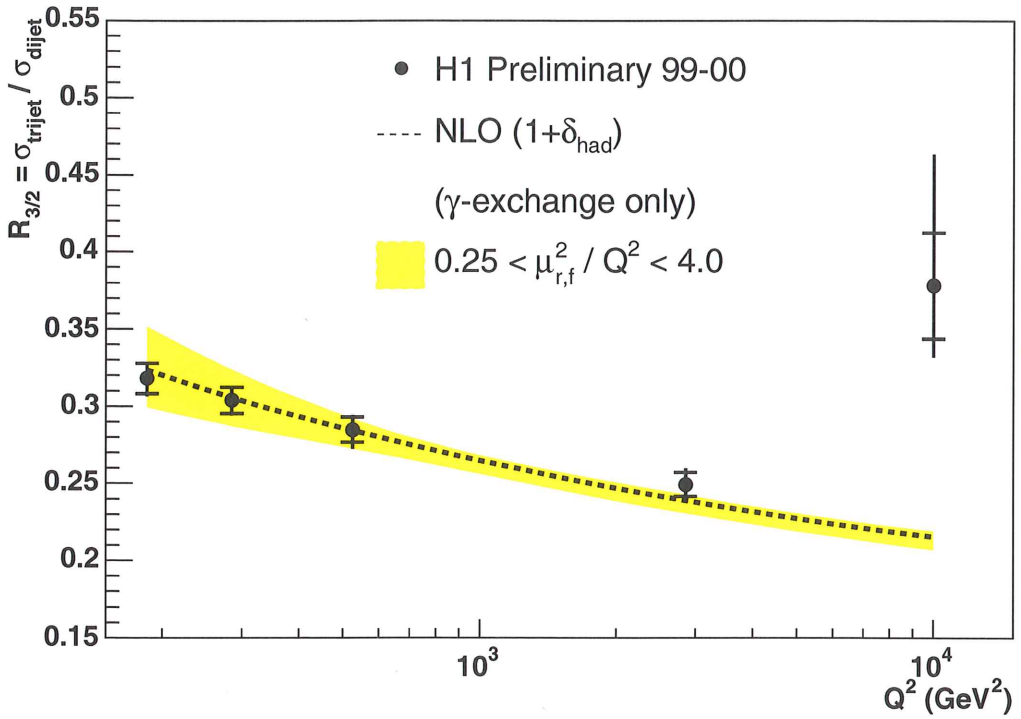

Figure 5.8: *Distribution of measured values of $R_{3/2}$ against Q^2 compared with a NLO pQCD prediction, with hadronization corrections.*

are in agreement with theory within quoted uncertainties. The deviation of the theoretical expectation for the dijet cross-section from the data in the final Q^2 bin is due to the omission of the effects of Z^0 exchange in the calculations and is approximately 20% in line with estimations (see section 3.5.1).

The theoretical description of the trijet event topology is studied further by comparing the differential cross-section with respect to E_T for each of the three principle jets with NLO pQCD predictions including with hadronization corrections. These distributions can be seen in figure 5.7. The agreement of theory with data is within the quoted uncertainties and is typically better than 5%. The cross-sections for the second and third highest E_T jets are multiplied by 10^{-2} and 10^{-3} respectively for increased visibility at the low end of the E_T spectrum, where the cross-sections are of a similar magnitude.

5.3.1 The Cross-Section Ratio, $R_{3/2}$

The distribution of $R_{3/2}$ with respect to Q^2 can be seen in figure 5.8. The data are well described by the NLO predictions in the region where electroweak effects can be neglected. Data lie within one standard deviation of the central NLO prediction, and well within the theoretical uncertainty associated with the renormalization/factorisation scale, across almost two orders of magnitude in Q^2. The total experimental uncertainty on $R_{3/2}$ is typically $< 2\%$. The experimental precision of the measurement and the quality of the description of the distribution of $R_{3/2}$ by NLO pQCD is sufficiently accurate to allow an extraction of the strong coupling to be made. This procedure is described in the next section.

Chapter 6

The Extraction

"While the true is Godlike, it does not appear directly. We must divine its reality from its manifestations." - Goethe

6.1 Next-to-Leading Order Calculations

The NLO predictions, calculated using the NLOJET++ programme, were performed using the CTEQ4A and CTEQ5M PDF sets. The CTEQ4A PDF sets are obtained with different assumptions for $\alpha_s(M_Z)$[1]. The CTEQ4A PDFs have been shown to be consistent with the CTEQ5 PDF ($\alpha_s(M_Z) = 0.118$) (figure 6.4) for the phase space regions used in this work. The dijet and trijet cross-section calculations with CTEQ5M have been shown in the previous section to be consistent with the data within uncertainties.

Figure 6.1 shows the NLO cross-section calculations, with respect to Q^2m for dijets (left) and trijets (right) differentially with respect to $\alpha_s(M_Z)$. NLO calculations include hadronization corrections and use $\mu_r = \mu_f = Q$. The dijet cross-section is fitted with the function $K_1\alpha_s^2(M_Z) + K_2\alpha_s(M_Z)$, whilst the trijet cross-section is fitted with the function $K_3\alpha_s^3(M_Z) + K_4\alpha_s^2(M_Z)$, where K_n are constants. The mathematical structures of these functions are those

[1] $\alpha_s(M_Z)$ values available in the CTEQ4A PDF are 0.110, 0.113, 0.116, 0.119 and 0.122.

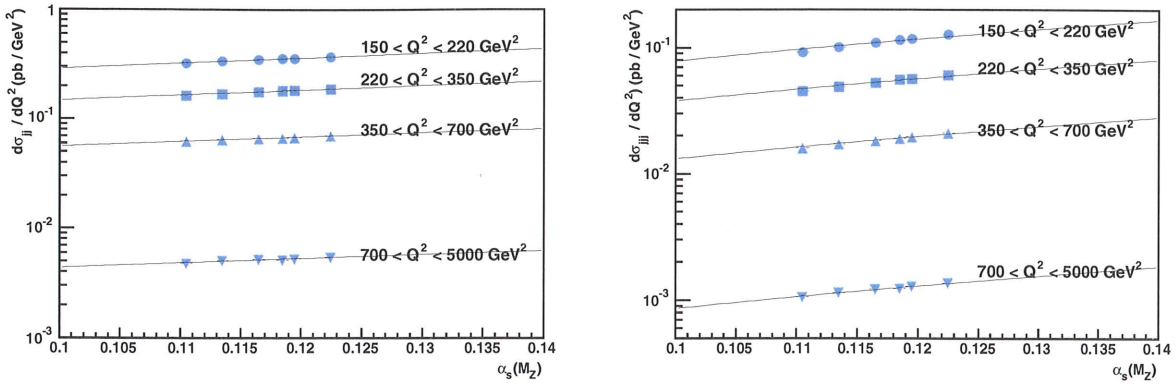

Figure 6.1: *NLO calculations of $d\sigma$ / dQ^2 against $\alpha_s(M_Z)$ for dijets (left) and trijets (right).*

expected from pQCD at next-to-leading order and it can be seen that the theoretical predictions show satisfactory agreement. The regularity of the fit functions provides further confidence in the NLO calculations.

The cross-sections calculated using the CTEQ4A PDF series are shown normalised (decreasing $\alpha_s(M_Z)$ from top to bottom) to the central value of the CTEQ4A series, known as CTEQ4M ($\alpha_s(M_Z) = 0.116$) in figure 6.2. It can be seen that a change of $\sim \pm 5\%$ in the value of $\alpha_s(M_Z)$ results in $\sim \pm 6\%$ change in the dijet cross-section but to a change of $\sim \pm 16\%$ in the trijet cross-section, demonstrating the sensitivity of the trijet cross-section to variations in the strong coupling.

The next-to-leading order calculations appear to be stable when used to calculate the dijet and trijet cross-sections as well their ratio $R_{3/2}$. It is therefore considered safe to proceed with the extraction of $\alpha_s(M_Z)$ using the theoretical calculations from NLOJET++.

6.2 Extraction of $\alpha_s(M_Z)$

The value of $R_{3/2}$ in the highest Q^2 bin was considered to be flawed due to the

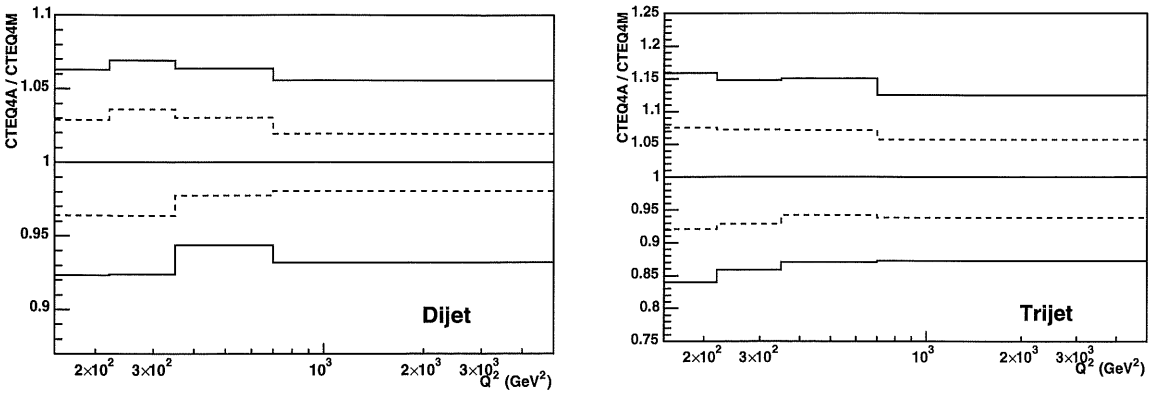

Figure 6.2: *Ratio of CTEQ4A series to CTEQ4M for dijets (left) and trijets (right).*

very small number of trijet events in this region of phase space. Also, as the effects of the Z^0 boson in this region are not included in the NLO programs considered in this work, no reliable theoretical predictions could be made. As such, only the virtuality range $150 < Q^2 < 5000$ GeV^2 is considered for the extraction of $\alpha_s(M_Z)$. Within this range, the distribution of $R_{3/2}$ with respect to Q^2, was used to extract $\alpha_s(M_Z)$. The method for extraction is similar to that employed in a recent publication by the ZEUS collaboration [2]. The procedure is as follows:

- The NLO calcultions are repeated for each available value of $\alpha_s(M_Z)$. The theoretical sensitivity to $\alpha_s(M_Z)$ is shown in figure 6.3.
- The function $C_1\alpha_s(M_Z) + C_2\alpha_s^2(M_Z) + C_3\alpha_s^3(M_Z)$ is fitted to the theoretical predictions from NLOJET++ using the CTEQ4A PDF, for each bin in Q^2 as shown in figure 6.4.
- A value of $\alpha_s(M_Z)$ is determined for each bin in Q^2 and an overall value calculated using a χ^2 minimization over the entire Q^2 range.

Figure 6.3 shows the sensitivity of the theoretical prediction for $R_{3/2}$ for the four data points considered for the α_s extraction. The data are in good agree-

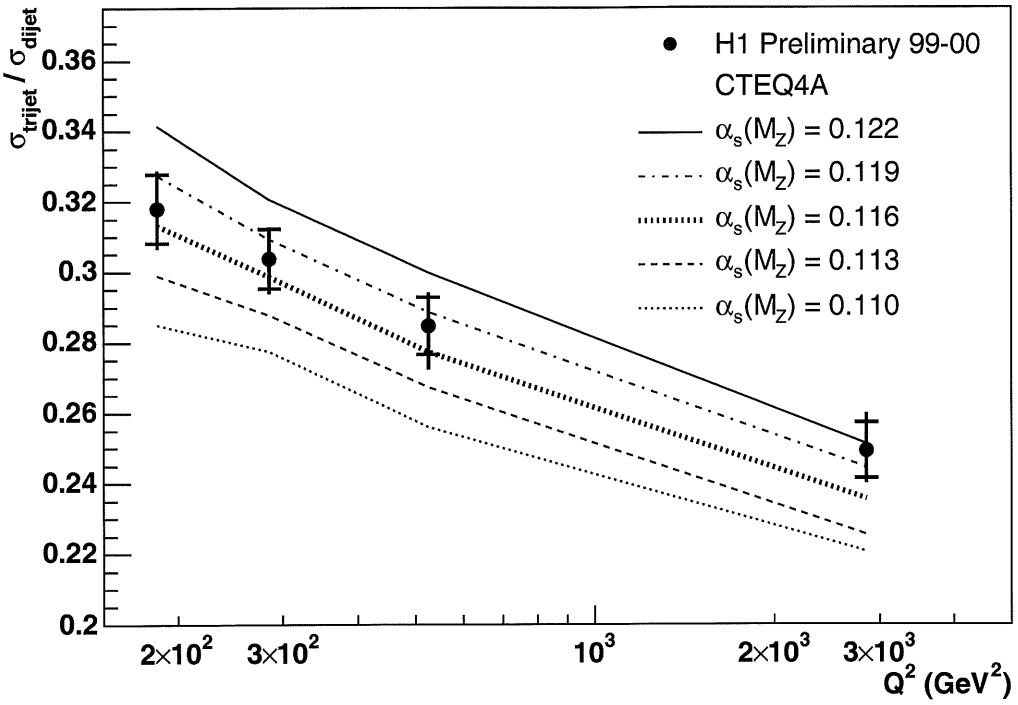

Figure 6.3: *Distribution of measured values of $R_{3/2}$ against Q^2 compared with NLO pQCD predictions, with hadronization corrections, for five values of $\alpha_s(M_Z)$. The CTEQ4A PDF set features parton information calculated using different $\alpha_s(M_Z)$ values.*

ment with the NLO values calculated with the value $\alpha_s(M_Z) = 0.118$ and so it is expected that the extracted value will be close to this figure.

Figure 6.4 shows the extraction for each Q^2 bin. The slope of each distribution appears to become shallower with increasing Q^2 and the fit is good for each bin. The $R_{3/2}$ values calculated with CTEQ5M are also shown (square points) to demonstrate the consistency of the PDFs employed in this region of phase space. The strong coupling is extracted for each bin, along with the statistical uncertainty, by comparing the measured value of $R_{3/2}$ to the function derived from the fit to the NLO predictions.

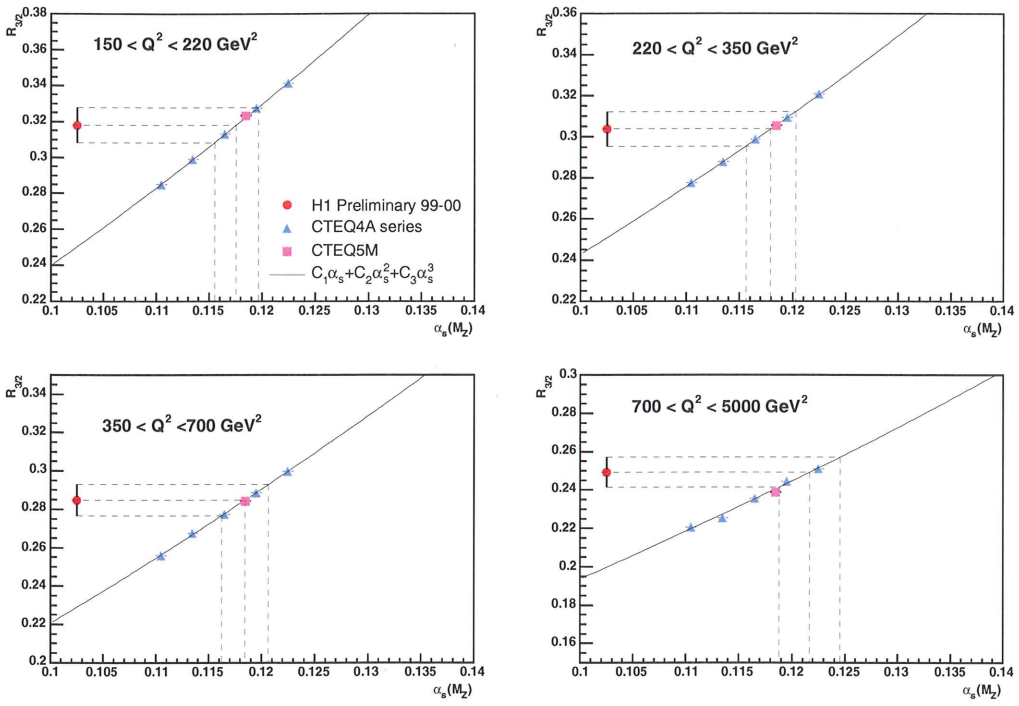

Figure 6.4: *$R_{3/2}$ against $\alpha_s(M_Z)$ for each Q^2 bin. The function $C_1\alpha_s(M_Z) + C_2\alpha_s^2(M_Z) + C_3\alpha_s^3(M_Z)$ is fitted to the theoretical predictions from NLOJET++ using the CTEQ4A PDF (triangles). The value obtained using the CTEQ5 PDF is also shown (square point).*

Taking into account only the statistical uncertainties on the measured values of $R_{3/2}$, $\alpha_s(M_Z)$ is determined to be $\alpha_s(M_Z) = 0.1187 \pm 0.0011$ (stat.).

The systematic and theoretical uncertainties of the extracted value of the strong coupling are found by repeating the above procedure using the cross-sections shifted by the total systematic and theoretical uncertainties as described in section 5.2. The value of $\alpha_s(M_Z)$ extracted from $R_{3/2}$ is thus:

$$\alpha_s(M_Z) = 0.1187 \pm 0.0011 \text{ (stat.)} \; ^{+0.0014}_{-0.0016} \text{ (syst.)} \; ^{+0.0050}_{-0.0050} \text{ (th.)}.$$

It was observed that the largest contributions to the systematic uncertainty on the extracted value of $\alpha_s(M_Z)$ came from the hadronic energy uncertainty

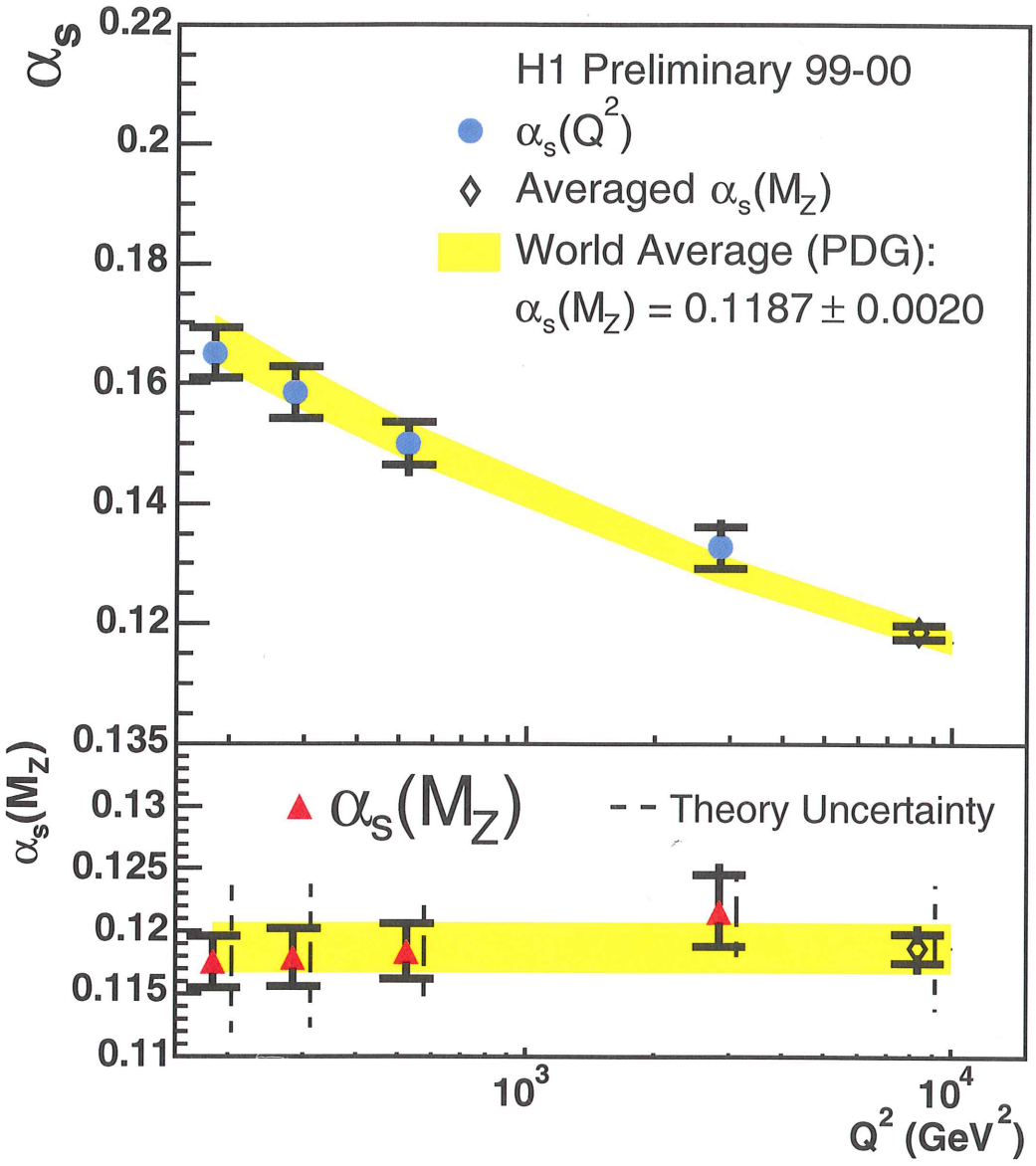

Figure 6.5: *Extracted $\alpha_s(Q^2)$ and $\alpha_s(M_Z)$ values from each Q^2 bin.*

and the uncertainty associated with the model. The largest contribution to the theoretical uncertainty was from the renormalization scale uncertainty at lower values of Q^2 and the hadronization uncertainty at higher values of Q^2.

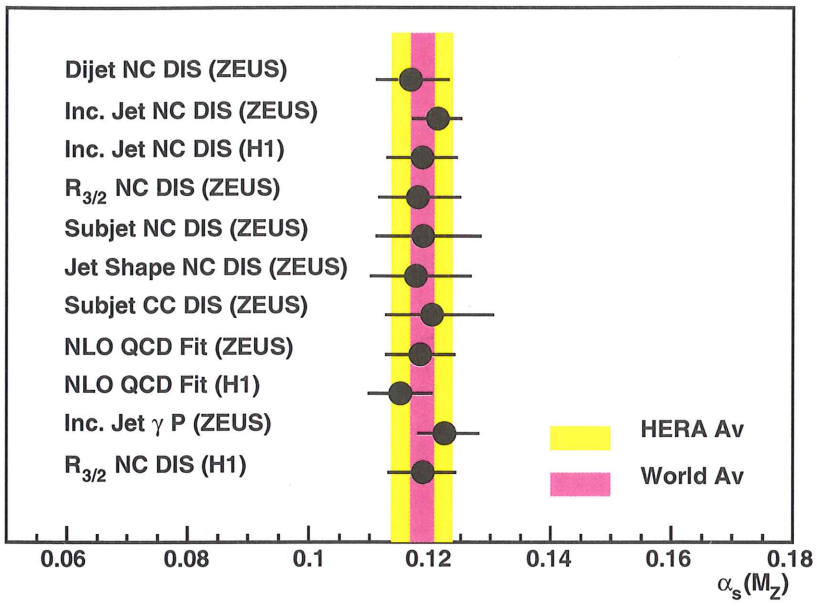

Figure 6.6: *Summary of $\alpha_s(M_Z)$ values from HERA. Uncertainties shown are experimental and theoretical combined in quadrature. The world average is $\alpha_s(M_Z) = 0.1187 \pm 0.0020$ and the HERA average is $\alpha_s(M_Z) = 0.1186 \pm 0.0051$.*

6.3 Analysis of α_s Determination

Figure 6.5 shows the extracted values of $\alpha_s(M_Z)$ from each Q^2 bin evolved to their values at their respective values of Q^2 (circles) using the two-loop solution of the renormalization group equation. The overall value of $\alpha_s(M_Z)$, found using a χ^2 minimisation procedure, is shown at the far right as a hollow point. The evolution of the current world average value of $\alpha_s(M_Z)$ is shown as a shaded band. The uncertainties shown are statistical up to the horizontal bar, and then the quadratic sum of statistical and systematic uncertainties. The world average is $\alpha_s(M_Z) = 0.1187 \pm 0.0020$[12]. The values of $\alpha_s(M_Z)$ are also shown in the lower part of figure 6.5, with the theoretical uncertainties shown as dashed lines offset to the right.

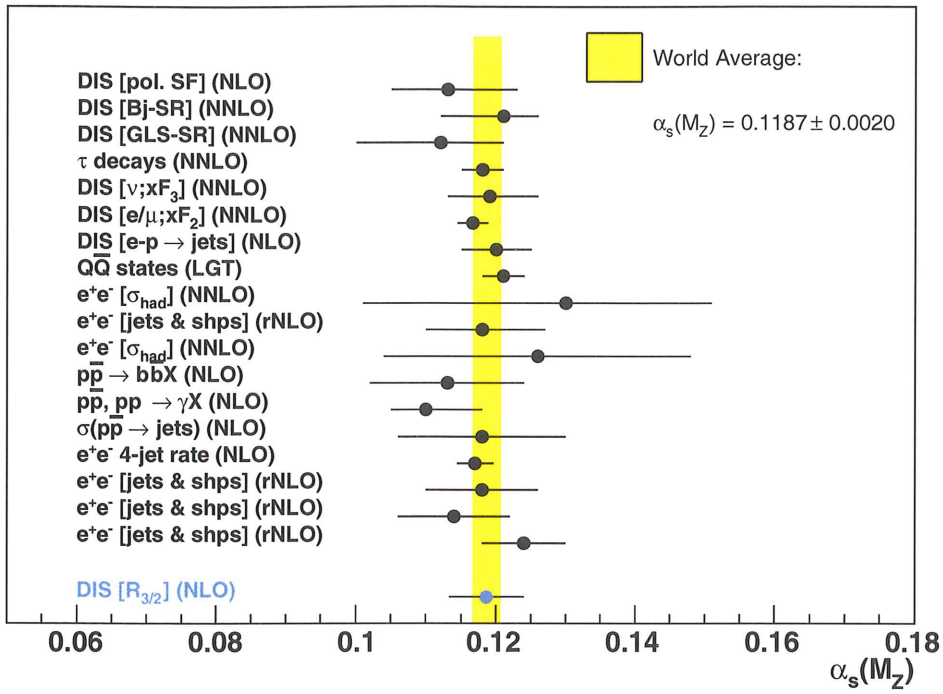

Figure 6.7: *Summary of $\alpha_s(M_Z)$ values from various experimental methods compared with the value from this work (bottom point). Uncertainties shown are experimental and theoretical combined in quadrature. The world average is $\alpha_s(M_Z) = 0.1187 \pm 0.0020$.*

This result is in good agreement with previous determinations at HERA, a selection of which are shown in figure 6.6, along with the current HERA average [68] and the world average as determined by the Particle Data Group [12]. The uncertainties shown are the quadratic sum of experimental and theoretical uncertainties. The result from this work is also shown and it can be seen that the uncertainties are competitive with determinations from both H1 and ZEUS and are similar to the HERA average.

The result is also competitive with results from other experimental procedures from different processes, as shown in figure 6.7. Uncertainties shown are experimental and theoretical combined in quadrature. Figure 6.7 shows a selection

of results that is in no way exhaustitive, but attempts to show a fair representation of the precision of results obtained in various processes [12] and it can be seen that the result obtained in this work is amongst the more precise determinations.

Chapter 7

The Conclusion and Outlook

"A conclusion is the place where you got tired of thinking." - Anon

Data collected by the H1 experiment at HERA during the years 1999 and 2000 were used to measure dijet and trijet cross-sections for neutral current deeply inelastic scattering to higher precision than has previously been achieved at H1. The ratio of these cross-sections, $R_{3/2}$, has been measured with a precision that permits a competitive extraction of the strong coupling constant, $\alpha_s(M_Z)$, to be performed from an analysis of this variable as a function of the momentum-transfer-squared (Q^2). Such an extraction is a first at H1 and represents an important test of our current understanding of the strong interaction.

The data used in this analysis correspond to an integrated luminosity of $\mathcal{L} = 65.4\ \text{pb}^{-1}$ and were taken at a centre-of-mass energy of $\sqrt{s} = 319$ GeV. The inclusive $k_\perp$ algorithm was employed to define the jets, which were clustered in the Breit frame of reference. Differential jet cross-sections were measured with respect to Q^2 for dijets and trijets and jet transverse energy, E_T, for trijets. Theoretical predictions of perturbative Quantum Chromodynamics agree with the data within the quoted uncertainties across a wide range of phase space. It has also been shown that leading-order event simulations with higher-order approximations based on parton cascade methods are effective in describing

the shapes of a diverse set of jet variables.

The strong coupling is extracted from four bins in Q^2 and a combined fit used to find an overall value. The combined fit yields the result

$$\alpha_s(M_Z) = 0.1187 \, ^{+0.0053}_{-0.0054} \quad , \tag{7.1}$$

which is in good agreement with the current HERA and world average values. The cancellation of uncertainties offered by the cross-section ratio method allows for a high precision determination of the strong coupling, with uncertainties of $\sim$ 4.5 %. The results from this work are in good agreement with current knowledge.

Significant improvements in experimental precision have been made since previous jet analyses at H1. Experimental uncertainties are now almost a factor of 3 smaller than theoretical uncertainties. This is to be compared with, for example, [6], where experimental and theoretical uncertainties were of similar size. This is due largely to the cancellation of uncertainties in the ratio method as well as to improvements in the hadronic calibration and smaller differences between the event simulation models used in the analysis. Improvements in theoretical precision will be required for advances on this result to be obtained. The large quantity of data taken during the HERAII run period will allow for greater statistical precision on quantities where events are scarce, such as the trijet cross-section at very high Q^2. The theoretical uncertainties on $R_{3/2}$ are found to be lowest for the Q^2 bins where the overlap of the trijet and dijet cross-sections are largest. A larger data set will allow for finer binning in this region of phasespace, with a corresponding reduction in the overall theoretical uncertainty. Further theoretical improvements such as full NLO event simulations for DIS and NNLO cross-section calculations for jet cross-sections seem improbable, due to the imminent start-up of CERN's Large Hadron Collider,

which has led to a declining interest in pQCD calculations for DIS.

The study of $R_{3/2}$ can be extended by the additional consideration of low Q^2 data ($Q^2 < 150\ GeV^2$). This region of phase space contains much high E_T jet data and it has been shown [2] that the cancellation of errors permits competitive theoretical uncertainties in this region. A larger quantity of data, combined with a cross-section calculation that includes the effect of the Z^0 boson, could also be employed to extend the phase space region to higher values of virtuality.

Appendix A

Tables of Results

Q^2 (GeV^2)	$(d\sigma / dQ^2)_{dijet}$ (pb/GeV^2)	δ Statistical (%)	δ Systematic (%)	C_{had}
150 - 220	0.353	2.56	$^{+3.24}_{-2.89}$	0.93
220 - 350	0.183	2.36	$^{+2.69}_{-2.21}$	0.93
350 - 700	0.0673	2.53	$^{+2.04}_{-2.45}$	0.94
700 - 5000	0.00503	2.86	$^{+2.69}_{-3.40}$	0.94
5000 - 15000	0.000109	11.01	$^{+11.01}_{-10.10}$	0.89

Table A.1: *The dijet differential cross-section $d\sigma/dQ^2$ for hadronic jets in the Breit frame. The statistical and systematic uncertainties are shown separately as percentages. The hadronization correction factor C_{had} is shown in the last column.*

Q^2 (GeV^2)	$(d\sigma / dQ^2)_{trijet}$ (pb/GeV^2)	δ Statistical (%)	δ Systematic (%)	C_{had}
150 - 220	0.112	4.37	$^{+2.12}_{-2.65}$	0.76
220 - 350	0.0555	4.23	$^{+3.57}_{-1.68}$	0.76
350 - 700	0.0192	4.44	$^{+4.65}_{-3.52}$	0.76
700 - 5000	0.00125	5.10	$^{+3.71}_{-2.48}$	0.73
5000 - 15000	0.0000408	18.18	$^{+6.49}_{-25.75}$	0.70

Table A.2: *The trijet differential cross-section $d\sigma/dQ^2$. Other details as table A.1.*

$Q^2(GeV^2)$	$R_{3/2}$	δ Statistical (%)	δ Systematic (%)
150 - 220	0.318	3.07	$^{+1.52}_{-1.81}$
220 - 350	0.304	2.78	$^{+1.05}_{-1.69}$
350 - 700	0.285	2.85	$^{+1.65}_{-3.23}$
700 - 5000	0.249	3.16	$^{+2.81}_{-1.89}$
5000 - 15000	0.378	9.09	$^{+20.6}_{-8.18}$

Table A.3: *The ratio of trijet to dijet differential cross-sections. Other details as table A.1.*

$Q^2(GeV^2)$	$\alpha_s(M_Z)$	δ Statistical	δ Systematic	δ Theoretical
150 - 220	0.1176	± 0.0020	$^{+0.0010}_{-0.0012}$	$^{+0.0065}_{-0.0057}$
220 - 350	0.1180	± 0.0023	$^{+0.0009}_{-0.0014}$	$^{+0.0058}_{-0.0057}$
350 - 700	0.1184	± 0.0022	$^{+0.0013}_{-0.0025}$	$^{+0.0038}_{-0.0043}$
700 - 5000	0.1217	± 0.0029	$^{+0.0025}_{-0.0017}$	$^{+0.0027}_{-0.0036}$
150 - 5000	0.1187	± 0.0011	$^{+0.0014}_{-0.0016}$	± 0.0050

Table A.4: *The $\alpha_s(M_Z)$ values determined in this analysis. Statistical, systematic and theoretical uncertainties are shown separately.*

E_T (GeV)	$(\mathrm{d}\sigma$ / $\mathrm{d}E_T)_{J1}$ (pb/GeV)	δ Exp. (%)	$(\mathrm{d}\sigma$ / $\mathrm{d}E_T)_{J2}$ (pb/GeV)	δ Exp. (%)	$(\mathrm{d}\sigma$ / $\mathrm{d}E_T)_{J3}$ (pb/GeV)	δ Exp. (%)
5 - 11	0.865	6.0	0.201	3.7	0.325	2.9
11 - 18	1.586	4.0	0.105	5.0	0.0265	10.5
18 - 30	0.374	5.8	0.0164	9.3	0.00219	30.4
30 - 60	0.0273	13.7	0.00109	23.8	-	-

Table A.5: *The jet differential cross-sections $d\sigma/dE_T$ for trijet events in the Breit frame. The statistical and systematic uncertainties are shown combined in quadrature into a total experimental uncertainty which is shown as a percentage. The subscript Jx indicates if the jet considered was the highest E_T (x = 1), next highest E_T (x = 2), or third highest E_T (x = 3).*

Appendix B

Hadronization in Monte Carlo

The example event shown in the following table was produced by a version of RAPGAP interfaced with the programme JETSET, which uses the Lund string model of hadronization. Column headings and particle numbers have been added for clarity. The products of hadronization are numerous and so this list has been truncated after only five such particles. As we are attempting to simulate the parton level, where these products of hadronization are not required, this list gives all the information that is needed to see how to produce the parton level events. In the table, "Ms" refers to the Mother particles and "Ds" to the Daughter particles, or decay products.

This is a neutral current DIS event. The first two particles (0, 1) are the incoming positron and proton from the HERA beam. The Z^0 (2) is the vector exchange boson in this event. The stable positron (3) is the scattered positron. The documentation particles (4, 5, 6, 7) are to be ignored as they do not feature in the final state. The final state partons are particles 8, 9, 10, 11, 12 and 13, where the di-quark ud1 (13) is the proton remnant. The *string* (14) is the so-called *Lund string*, which enters in the hadronization model. Thus we need to select particles whose Daughters have particle type *string*. Some events will have more than one string, but both daughters will *always* be of type *string* for the pre-hadronisation partons for this hadronisation model. This can easily

be modified for a cluster model, such as that implemented in HERWIG. It is simply a matter of substituting *cluster* for *string*. The Particle Data Group (PDG) numbers for these simulation products are 92 for *string* and 91 for *cluster*. Once the pre-hadronization particles are selected, they can be used for whatever purpose is necessary, e.g. boosted to the Breit frame and passed to the jet finder for clustering into jets as performed in this analysis.

A selection of the steering parameters for the event generator are provided here, to give a clearer picture of the parton level. Parameters for RAPGAP, DJANGO and JETSET take their default values.

- Time-like partons are permitted to shower.
- Soft gluons are resummed and included together with the hard radiation.
- Q^2 values at branches are strictly ordered, increasing towards the hard scattering.
- Width of Gaussian primordial transverse momentum of partons in the proton is 0.44 GeV.
- $\Lambda_{QCD} = 0.25$ GeV.
- The momentum cuttoff for both initial and final state parton showers was set to 1 GeV.

No	Particle	Status	Ms	Ds	Px	Py	Pz	E	Mass
0	e+	beam	-1 -1	-1 -1	0.0000	0.0000	-27.6000	27.6000	0.0005
1	proton	beam	-1 -1	-1 -1	0.0000	0.000092	0.0000	920.0005	0.9383
2	Z0	doc	0 -1	-1 -1	-4.9886	-6.8245	-15.9294	13.1895	91.1870
3	e+	stable	0 -1	-1 -1	4.9886	6.8245	-11.6706	14.4105	0.0005
4	u	doc	1 -1	-1 -1	0.2302	0.3465	4.9110	4.9101	0.3300
5	u	doc	4 -1	-1 -1	-0.7483	1.4998	3.4764	2.3390	0.3300
6	u	doc	2 -1	-1 -1	-1.8607	-3.1742	-8.9569	9.6832	0.3300
7	g	doc	2 -1	-1 -1	-3.8731	-2.1463	-3.4894	5.8338	0.0000
8	u	decayed	6 -1	14 14	-1.7631	-1.1335	-6.8909	7.2026	0.3300
9	g	decayed	6 -1	14 14	-1.5244	-2.9740	-3.8360	5.0876	0.0000
10	g	decayed	6 -1	14 14	-2.4464	-1.2130	-1.7194	3.2268	0.0000
11	g	decayed	-1 -1	14 14	0.6871	-0.9957	0.2933	1.2448	0.0000
12	g	decayed	-1 -1	14 14	0.4836	-0.5416	1.1898	1.3938	0.0000
13	ud1	decayed	1 -1	14 14	-0.4255	0.0332	915.0339	915.0344	0.7713
14	string	decayed	8 13	15 30	-4.9886	-6.8245	904.0705	933.1900	0.0000
15	omega	decayed	14 -1	31 33	-2.1541	-2.7216	-5.5019	6.5528	0.7819
16	pi0	decayed	14 -1	34 35	-0.3444	0.3282	-1.3733	1.4596	0.1350
17	K*+	decayed	14 -1	36 37	-0.6983	-0.3765	-1.1380	1.7010	0.8916
18	K*-	decayed	14 -1	38 39	-0.5662	-1.0228	-2.1721	2.6135	0.8916
19	pi0	decayed	14 -1	40 41	-0.3201	-0.0952	-0.1083	0.3762	0.1350

Appendix C

Charge Screening in QED

According to quantum field theory, an electron can be considered to be constantly emitting photons that in turn annihilate into electron positron pairs, such that the electron can be considered to be surrounded by a cloud of these pairs. Due to the Coulomb force between opposite charges, these pairs will possess a kind of polarisation with the positrons tending to be closer to the parent (or *bare*) charge. This appears similar to the situation of a charge in a dielectric, but the effect occurs for different reasons. In the language of quantum field theory, this idea requires higher order processes. If we measure the electric charge via a scattering experiment[1] then the determined value will depend upon how close to the bare charge the incident particle can penetrate. In the case of very large momentum transfer, (q), or in other words, a small impact parameter, the incident charge will interact with the bare charge with little screening and the measured charge will increase with q. As $q \to \infty$ then so too does the measured value of the charge. However, this divergence can be handled by the use of a *renormalized* charge e defined at an arbitrary value $Q^2 = \mu^2$ (recall $Q^2 = -q^2$). This then allows the charge variation to be calculated in tems of Q^2. The standard way of expressing this is in terms of a running coupling $\alpha(Q^2)$. This gives

[1]This effect must not be considered to be process dependent.

$$\alpha(Q^2) \simeq \frac{\alpha(\mu^2)}{1 - \frac{\alpha(\mu^2)}{3\pi}\log(\frac{Q^2}{\mu^2})} \quad , \tag{C.1}$$

where this approximate expression is best at high Q^2. The electromagnetic coupling, otherwise known as the *fine structure constant*, increases fairly slowly with Q^2.

Appendix D

Reconstruction Methods

The measurements of the products of NC DIS events at H1 allow different methods of reconstruction of the kinematic variables that define the event. These methods differ in resolution for each variable due to the different precision with which each component quantity can be measured. There is redundancy between the methods that allows methods to be combined in order to obtain the best resolutions for as many variables as possible.

D.1 The Electron Method

The kinematics describing a DIS event may be described using information from the scattered electron alone[64]. If the beam energy of the incident electron, E, the scattered electron energy, E′, and the polar angle of the scattered electron, θ, are known, for example in a well measured neutral current DIS event, the kinematics may be defined as follows:

$$Q_e^2 = 4EE'\cos(\frac{\theta^2}{2}) \qquad y_e = 1 - \frac{E'}{2E}(1-\cos\theta) \qquad x_e = \frac{Q_e^2}{sy_e} \qquad \text{(D.1)}$$

The Electron Method gives excellent resolution for the variable Q^2 but the resolution of y decreases at low values of y.

D.2 The Double Angle Method

The Double Angle (DA) Method[64] utilises the angles of the scattered electron and the hadronic final state to reconstruct the kinematic variables, as follows:

$$\Upsilon Q^2_{DA} = 4E^2 \sin\gamma(1+\cos\theta) \qquad \Upsilon y_{DA} = \sin\theta(1-\cos\gamma) \qquad x_{DA} = \frac{Q^2_{DA}}{s y_{DA}} \tag{D.2}$$

where γ is the polar angle of the hadronic system and $\Upsilon = \sin\gamma + \sin\theta - \sin(\theta+\gamma)$. This method is insensitive to the absolute calorimeter energy calibration, but sensitive to the relative calibration between different sections of the detector. The Double Angle Method is not employed in this work except as a means of calibrating the electromagnetic and hadronic energy scales of the calorimeters.

D.3 The Sigma Method

The Sigma Method[65] uses information from both the hadronic final state and the scattered electron to reconstruct the kinematics as follows:

$$y_\Sigma = \frac{\Sigma}{E - P_Z} \qquad Q^2_\Sigma = \frac{(E'\sin\theta)^2}{1-y_\Sigma} \qquad x_\Sigma = \frac{Q^2_\Sigma}{s y_\Sigma} \tag{D.3}$$

where $\Sigma = \Sigma_{i\neq e} E_i - P_{Z,i}$ and $E - P_Z = \Sigma_i E_i - P_{Z,i}$. The former sum is over the entire hadronic final state, excluding the scattered electron, e. This method has reduced sensitivity to QED radiation from the incoming electron as the initial beam energy does not feature in the definition. It is best suited for determination of the value x.

D.4 The Electron-Sigma Method

The Electron-Sigma Method[66] combines the excellent Q^2 resolution of the Electron Method with the precision x determination from the Sigma Method. It is defined as follows:

$$Q^2_{e\Sigma} = Q^2_e \qquad x_{e\Sigma} = x_\Sigma \qquad y_{e\Sigma} = \frac{Q^2}{s x_{e\Sigma}} \tag{D.4}$$

The Electron-Sigma Method is utilised for the kinematic reconstruction throughout this work.

Appendix E

Example Events

The following are examples taken from the H1 event display. The date of each event is shown, and many are for illustrative purposes only in that they were not taken during the run period considered in this work. Example dijet and trijet events from the 1999-2000 run period that is used for this work are also shown. Several of these example event pictures were selected by J. Meyer as part of the H1 event tutorial available at the H1 experiment world wide web page (http://www-h1.desy.de/). It should be noted that the events shown are in the laboratory frame and there is no direct correlation between jets in this frame and the Breit frame where the analysis is conducted. However, clearly separated, high E_T jets in the laboratory frame are likely to change little when found in the Breit frame. Jet events shown in this section pass all selection criteria in the Breit frame and illustrate the jet-like nature of the hadronic final state. It is also worth mentioning that although the jets within events may appear obvious to the eye, jets must be precisely defined and found by the $k_\perp$ algorithm as described elsewhere in this work.

Figure E.1 shows an example of the CJC in $r - \Phi$ view. The image on the left shows the raw hits in the detector, where each black dot represents a *hit* on a wire within the chamber caused by the passing of a charged particle. The image on the right shows the output of the track fitting algorithm that

links the individual hits into tracks using statistical methods. It is interesting to note that, to the eye, the tracks from the hits appear obvious. However, the track fitting algorithm is by no means trivial. This is one example of the tasks that the brain is very good at, but that prove difficult for computers to replicate.

Figure E.2 shows a closer view of raw hits in CJC1 and CJC2. In this event, the high voltage (HV) supply to the sense wires was being ramped up with the result that CJC1 was at 90% and CJC2 at 95% of the nominal HV values. The effect of this reduced voltage can be seen by the absence of hits in some regions of the chambers.

Figure E.3 shows an example background event, where several cosmic muons passed through the H1 detector at once. Cosmic rays that occur at a time that is inconsistent with a bunch crossing will be excluded from the data sample by the CJC T0 requirement. Events that have cosmics occuring during an otherwise regular event will be rejected as the quantity $E - P_Z$ will be too large.

Figure E.4 shows an example event where the scattered electron has fallen into one of the $r-\Phi$ cracks in the H1 detector. The electron, distinguished from the hadronic final state by its single track nature, can be seen to have deposited its energy into the hadronic calorimeter after passing through the crack in the electromagnetic calorimeter. These events can be misidentified as jets and as such are removed from the data sample.

Figure E.5 shows a neutral current event that also includes a beam halo muon, the track seen passing through the muon chambers and hadronic calorimeter at the top of H1. Beam halo muons occur when a proton from the proton beam interacts with the beampipe prior to the primary interaction vertex producing

pions which subsequently decay into muons. These events are excluded from the data sample using a series of topological background finders.

Figure E.6 shows a compton scattering background event, which involves the scattering of an electron off a photon. The event contains two charged particle tracks travelling in the negative x direction which have arisen as the scattered photon has converted into an electron-positron pair in the material of the silicon trackers. This can be seen in the closer view of the CJC, with the disparate charges bending in opposite directions in the H1 magnetic field.

Figure E.7 shows a neutral current scattered electron with final state QED radiation. The scattered electron radiates a photon which subsequently converts to an e^+e^- pair in the detector material. This will have the effect of altering the determined Q^2 of the scattered electron, due to a shift in its position within the detector if the electron and photon are detected as a single object and due to a shift in both the energy and position if not. The effect of final state QED radiation is accurately accounted for in this work by the precise determination of its effect on simulated events.

Figure E.8 shows a high Q^2 jet event that occured whilst all the HV for the central and forward trackers was off. It is a requirement for the data sample considered in this work that at least the central trackers must feature in the event in order to ensure that the z vertex position and hence the event kinematics are well reconstructed.

Figure E.9 shows the classic single "pencil" jet, in neutral current DIS. The hadronic final state is nearly entirely contained within the tightly collimated single jet.

Figure E.10 shows a dijet event from the data sample considered in this work.

It can be seen that the HV in the forward track detector (FTD) was off during this event, but as this is not a requirement for a precise reconstruction of the event kinematics, this event was included. Tracks from each jet and the scattered electron can be seen in the central trackers, with large energy deposits in the calorimeters.

Figure E.11 shows the tracks from a dijet event from the data sample considered in this work. The forward and central trackers are shown. It can be seen that almost the entire hadronic final state is contained in the two jets. The scattered electron is clearly visible as an isolated single track.

Figure E.12 shows a neutral current trijet event from the data sample considered in this work. Three distinct jets are clearly visible in the central and forward trackers, as well as the hadronic calorimeter. The scattered electron is towards the rear of the detector in the BBE section of the electromagnetic calorimeter.

Figure E.13 shows the tracks from a neutral current trijet event from the data sample considered in this work. The tracks from the jets are clearly separated and the scattered electron shown as a well isolated single track. Again, almost the entire hadronic final state is included within the three jets.

Figure E.14 shows a higher jet multiplicity event, with four jets found in the Breit frame. The four jets are also visible in the laboratory frame, with the lowest E_T jet featuring towards the bottom of the detector.

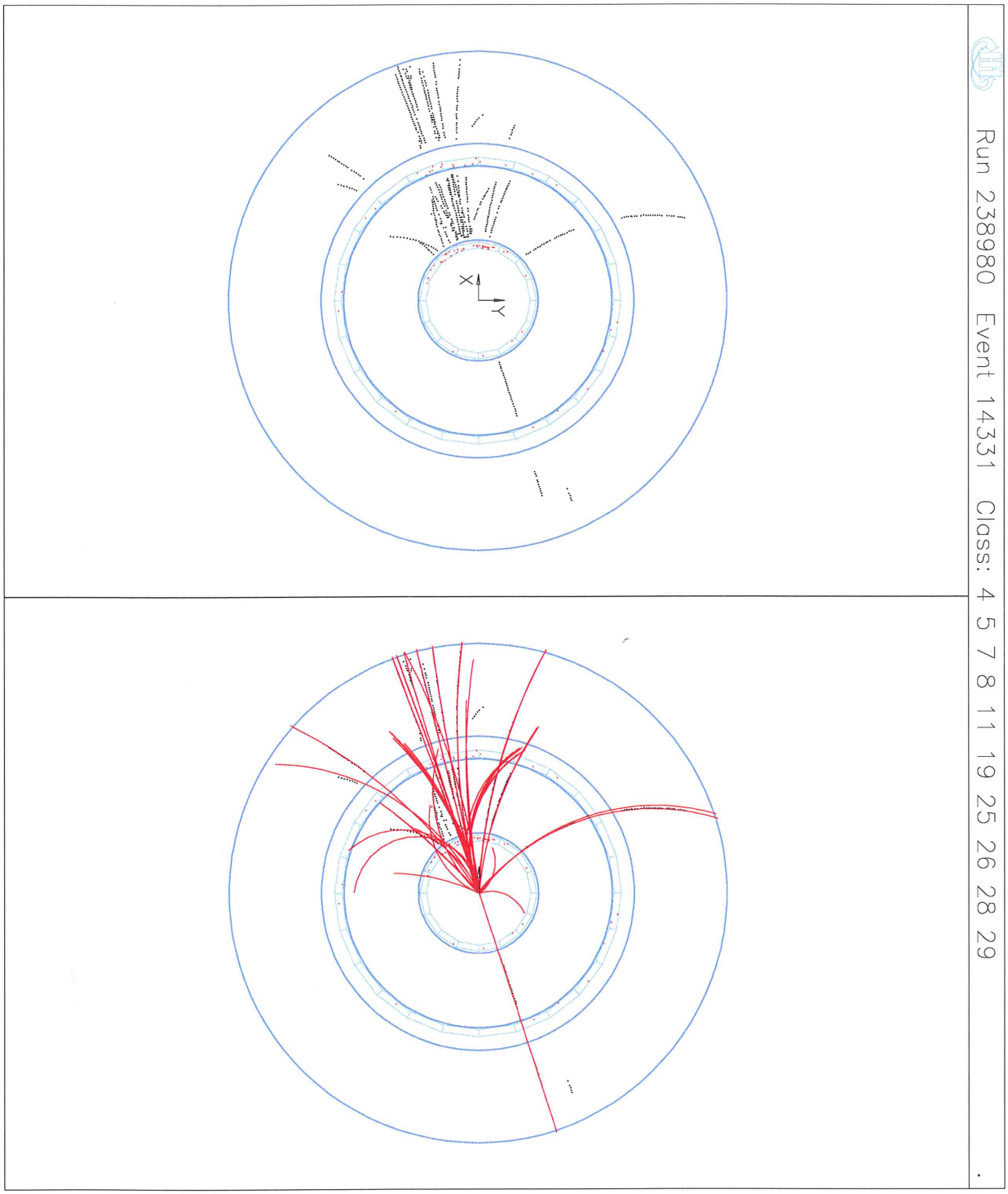

Figure E.1: *Tracks in the CJC: raw hits (left) and fitted tracks (right).*

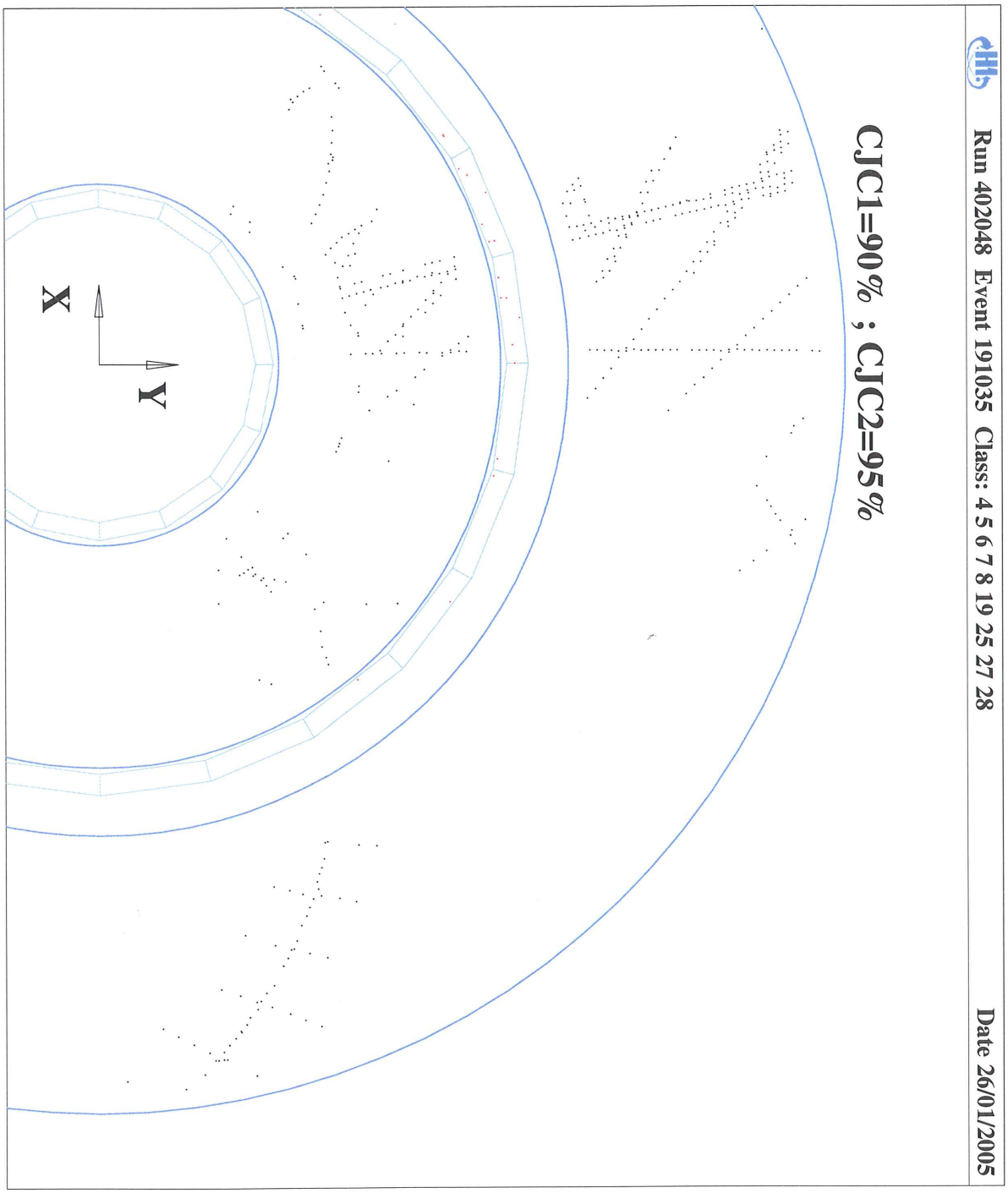

Figure E.2: *Raw hits in CJC1 and CJC2.*

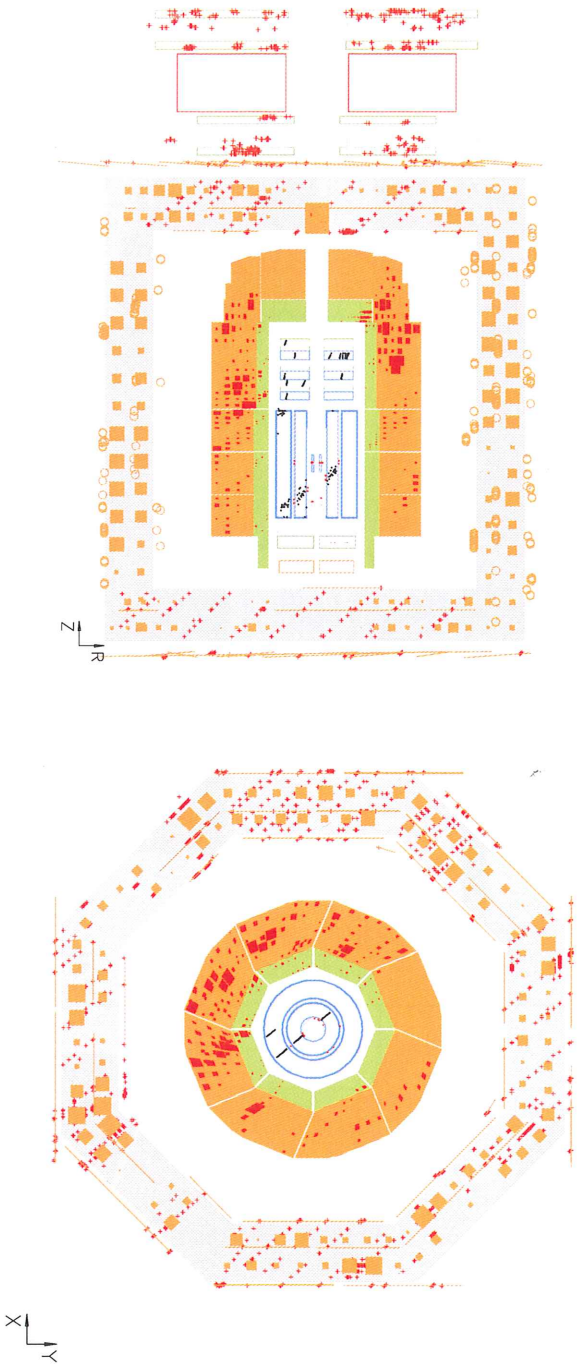

Figure E.3: *Cosmic ray shower.*

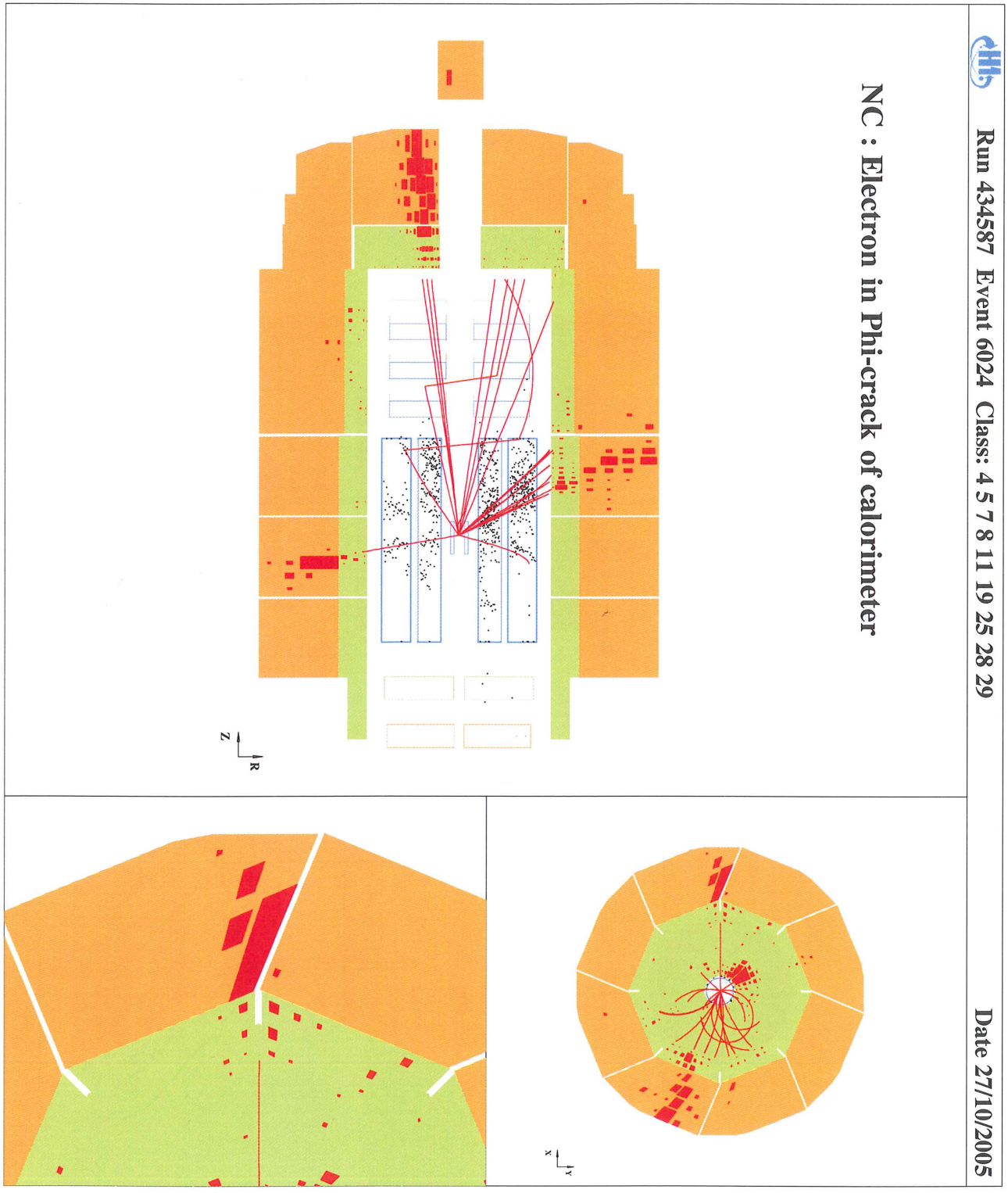

Figure E.4: *Neutral current event with electron in phi crack.*

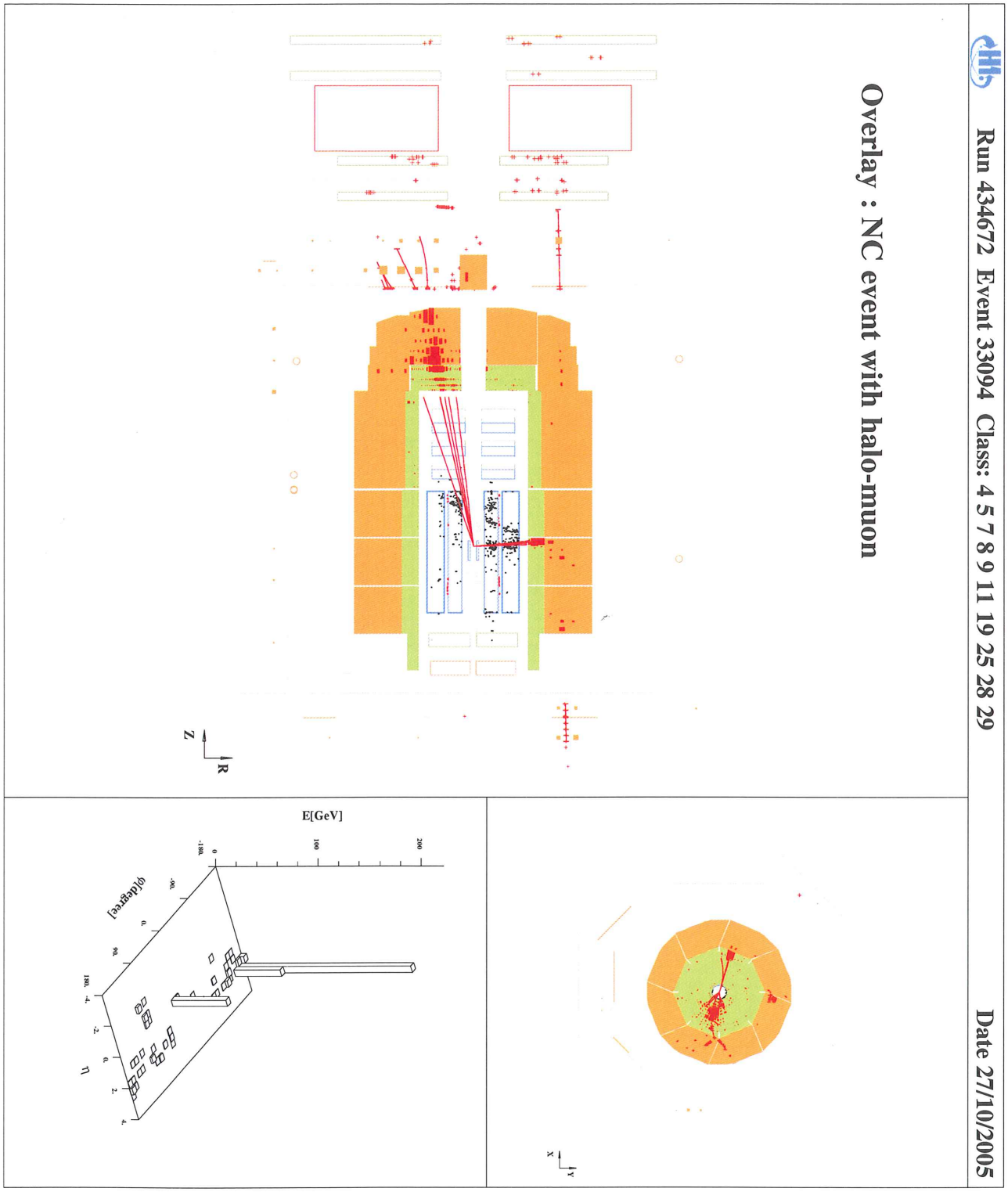

Figure E.5: *Neutral current event with beam halo muon.*

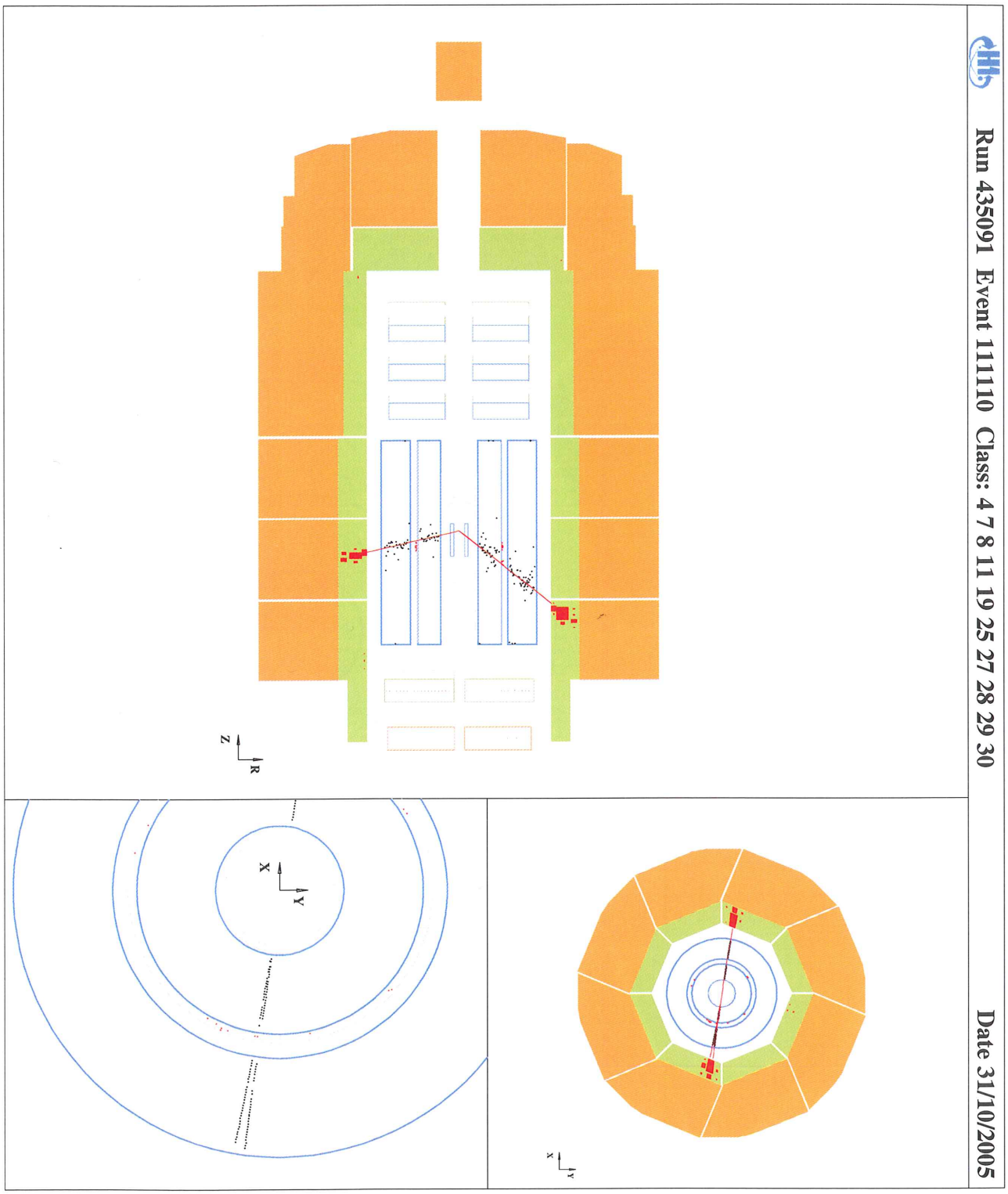

Figure E.6: *Compton scattering with photon conversion to e^+e^- pair.*

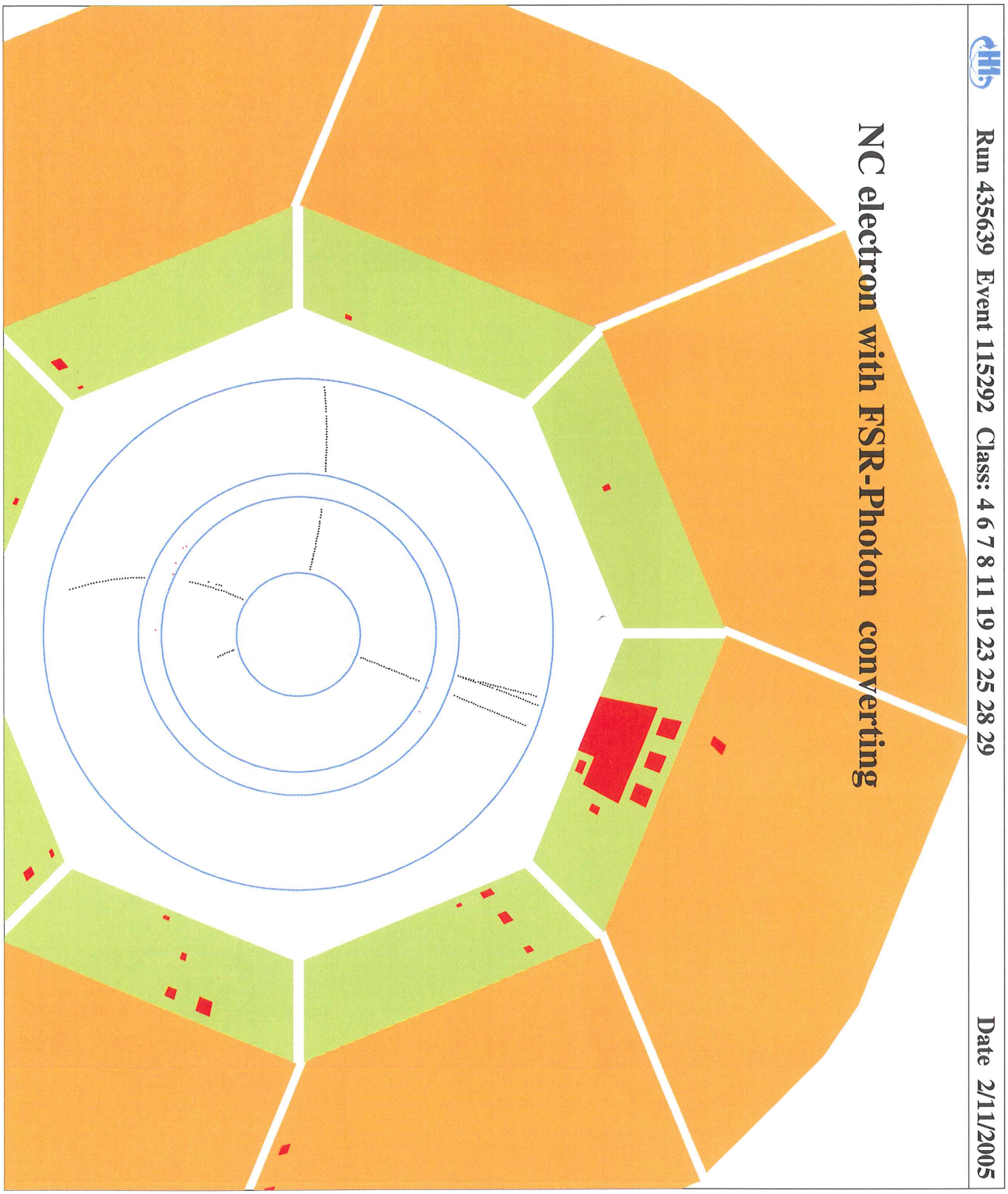

Figure E.7: *Neutral current scattered electron with final state QED radiation.*

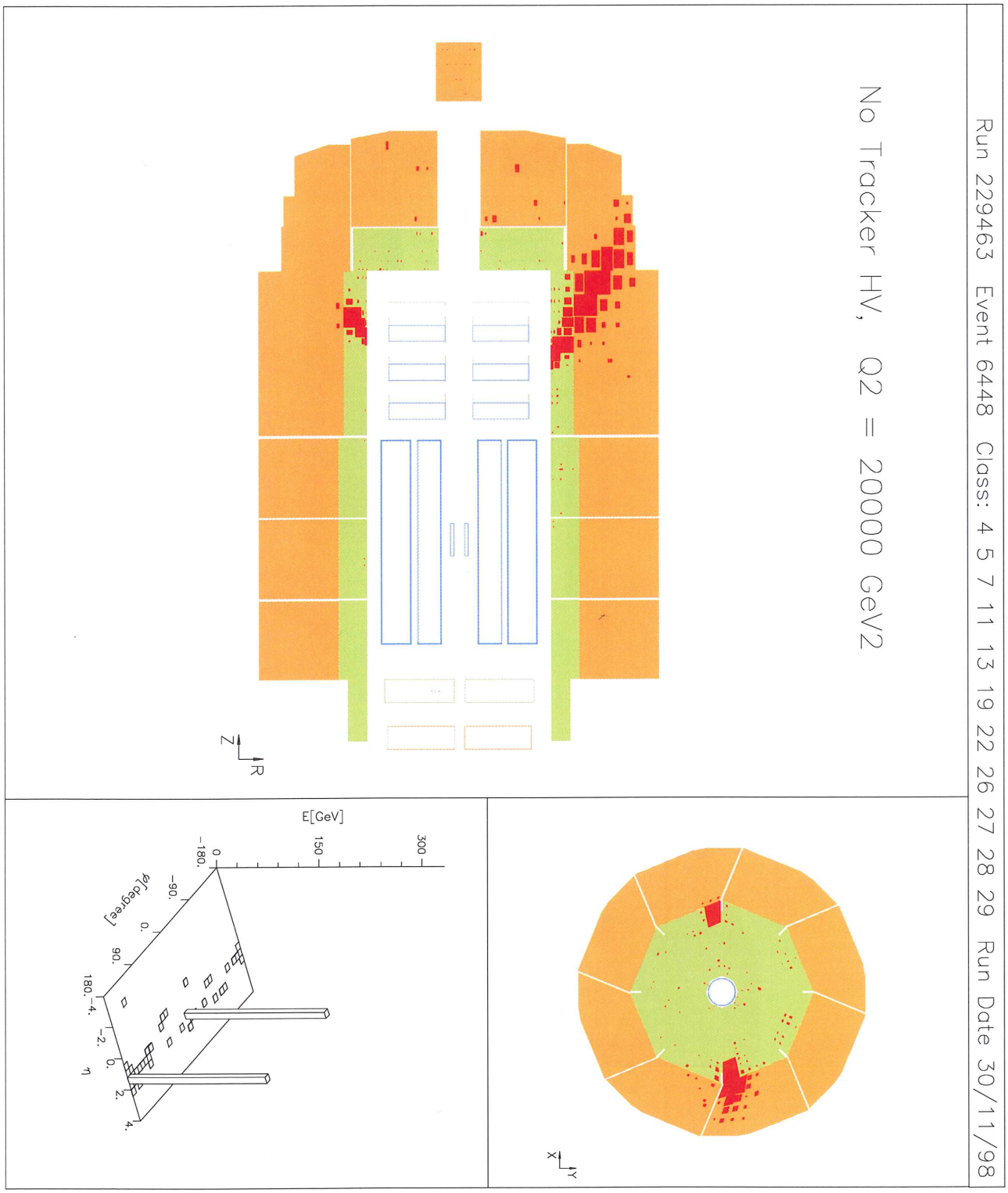

Figure E.8: *Neutral current event with all tracker HV off.*

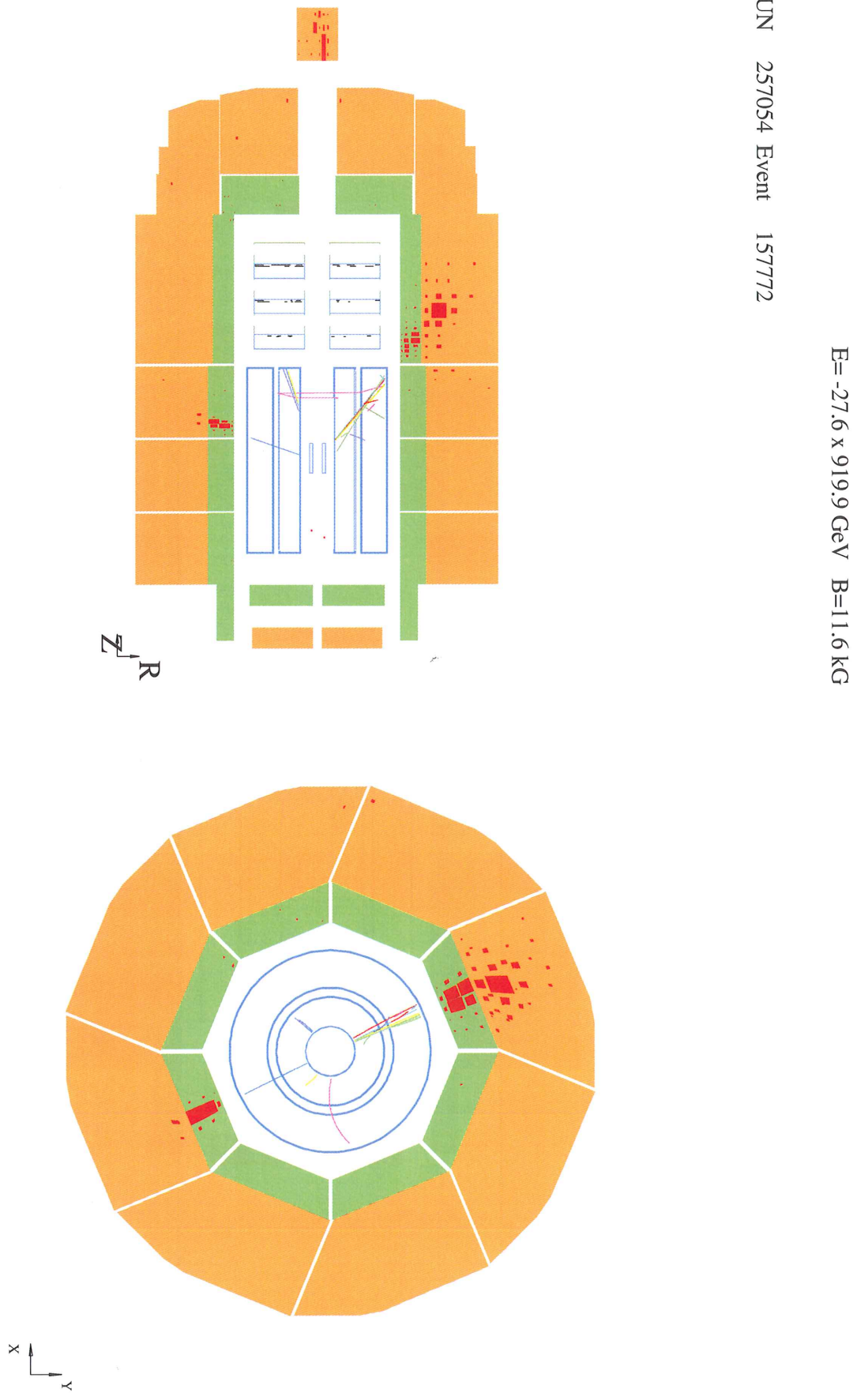

Figure E.9: *Neutral current single jet event.*

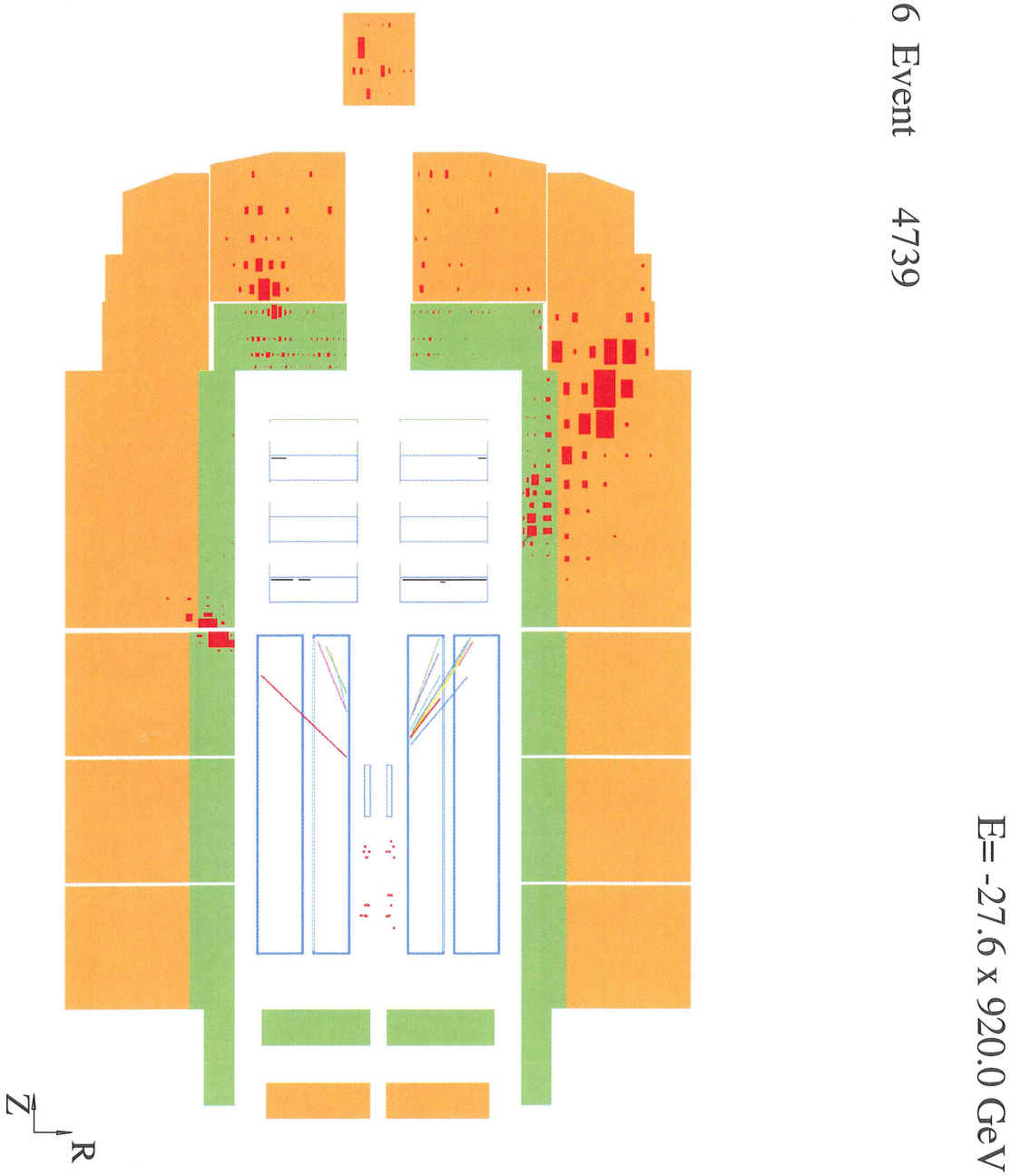

Figure E.10: *Neutral current dijet event, with no FTD HV.*

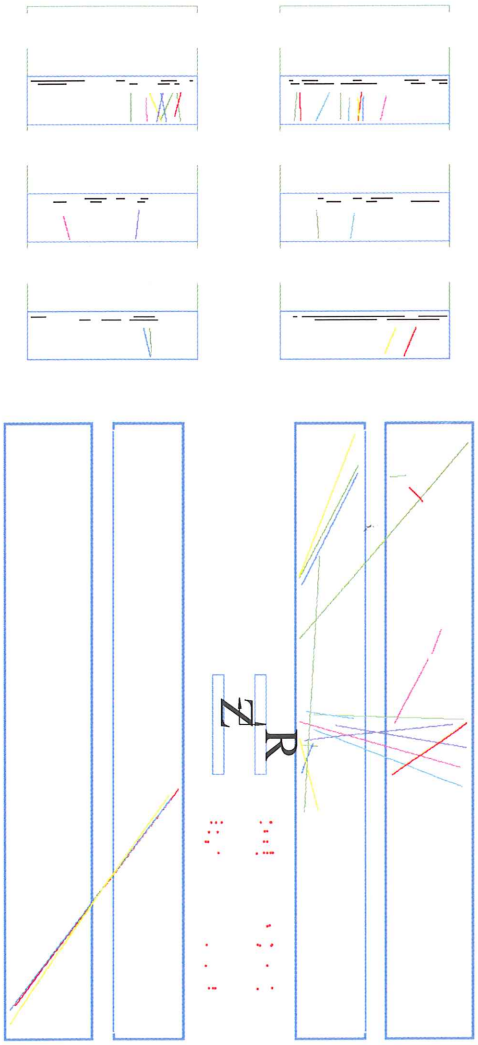

Figure E.11: *Neutral current dijet event, trackers only.*

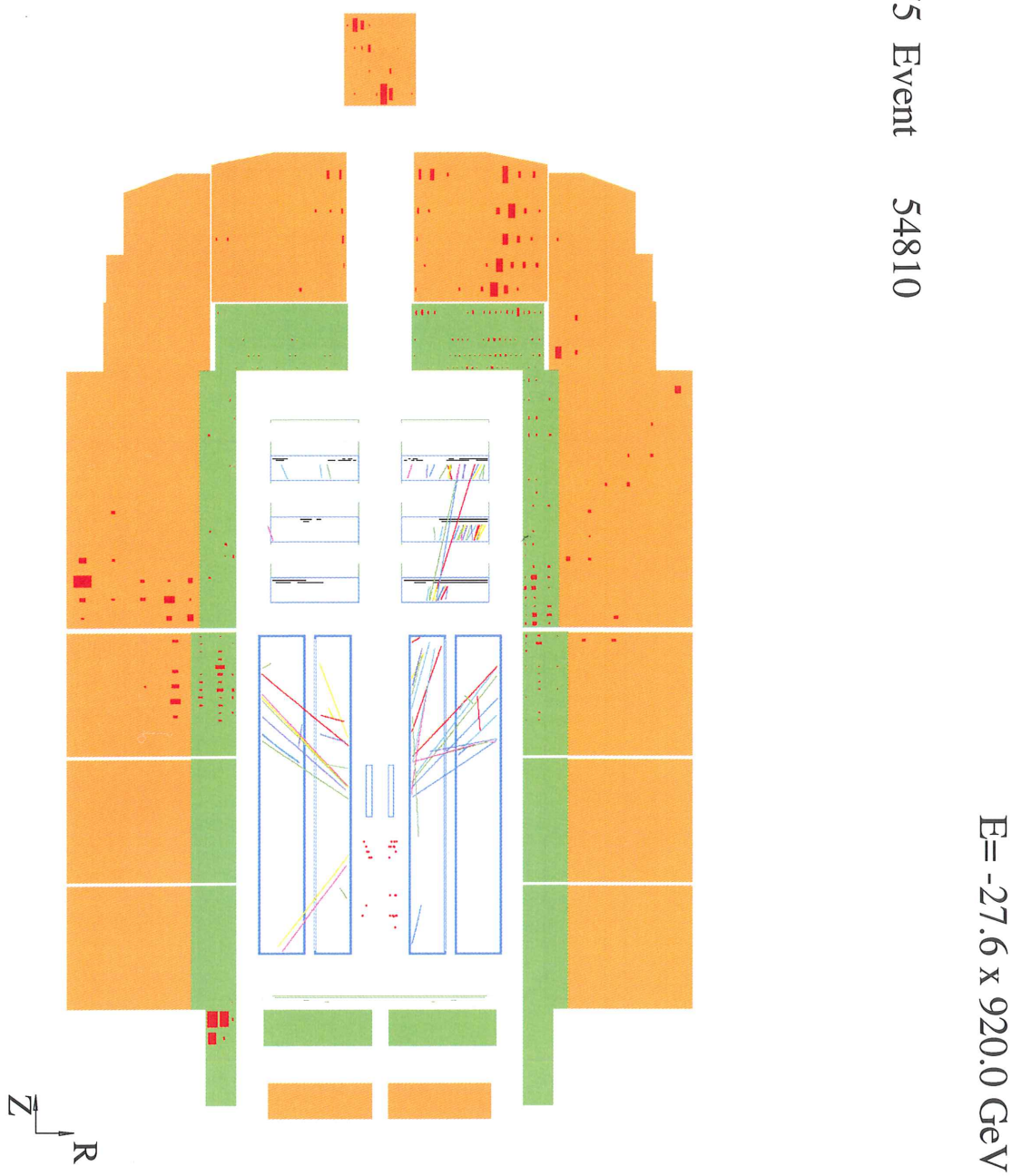

Figure E.12: *Neutral current trijet event.*

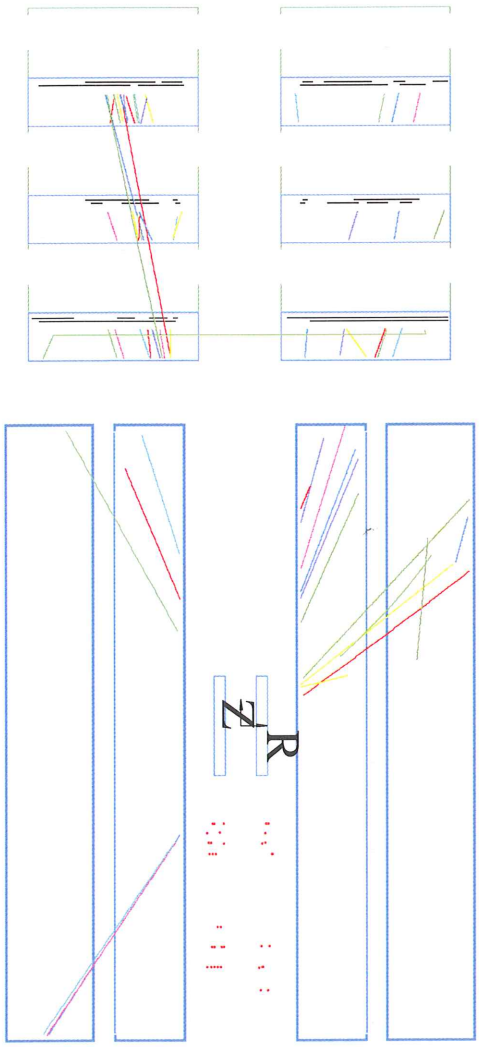

Figure E.13: *Neutral current trijet event, trackers only.*

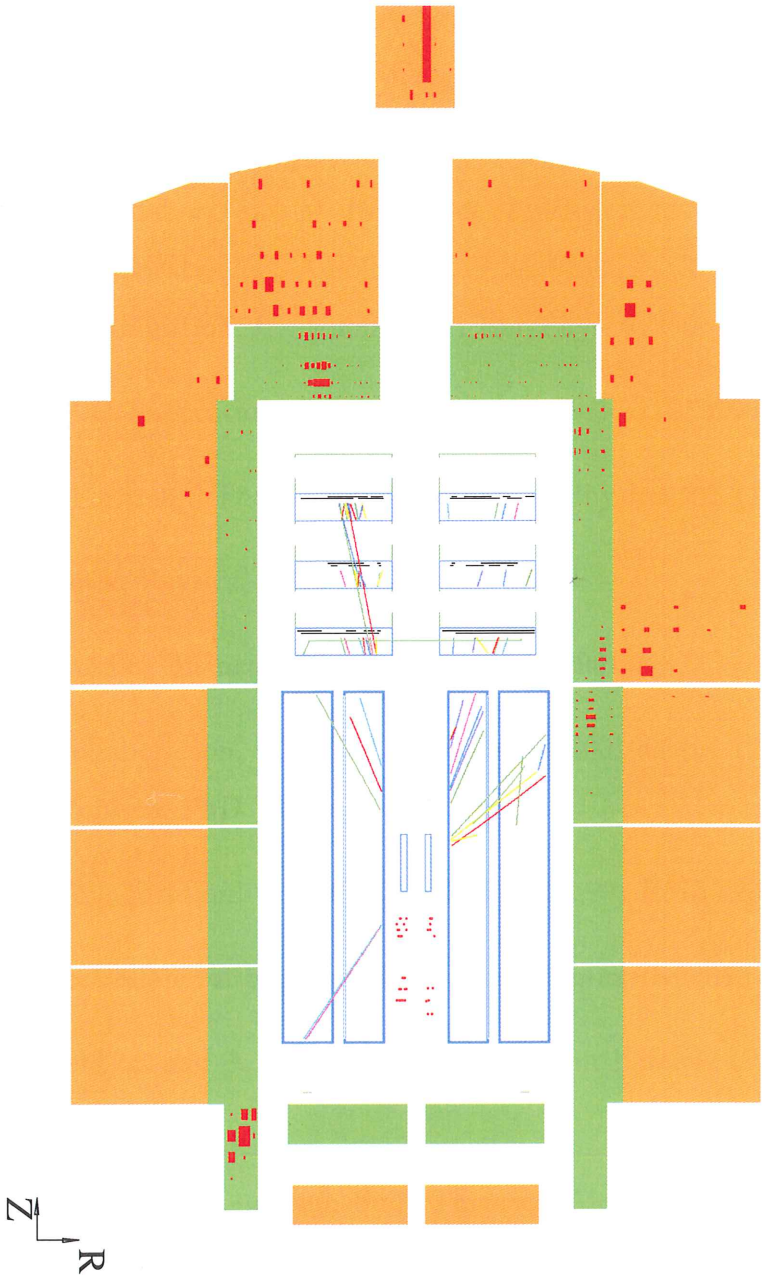

Figure E.14: *Neutral current four jet event.*

References

[1] H1 Collaboration, S. Aid *et al.*, Nucl. Phys. B 449 (1995) 3;
ZEUS Collaboration, M. Derrick *et al.*, Phys. Lett. B 363 (1995) 201;
H1 Collaboration, C. Adloff *et al.*, Eur. Phys. J. C5 (1998) 625;
H1 Collaboration, C. Adloff *et al.*, Eur Phys. J. C6 (1999) 575.

[2] ZEUS Collaboration, S. Chekanov *et al.*, hep-ex/0502007 (2005).

[3] R.P. Feynman, The Feynman lectures in Physics, 2-1 (1963).

[4] Aristotle, Physics, c.330 B.C.

[5] F. Mandle, Quantum Mechanics, Wiley (2001).

[6] H1 Collaboration, C. Adloff *et al.*, hep-ex/0010054v1 (2000);
M. Wobisch, PhD Thesis, DESY.

[7] H1 Collaboration, C. Adloff *et al.*, Phys. Lett. B515 (2001) 17-29.

[8] ZEUS Collaboration, J. Breiweg *et al.*, hep-ex/0102042 (2001).

[9] I.Aitchison and A.Hey, "Gauge Theories in Particle Physics" [IoP Publishing(2001)].

[10] Michio Kaku, "Quantum Field Theory, a Modern Introduction" (1993).

[11] D. Griffiths, "Introduction to Elementary Particles"[Addison and Wesley(1989)].

[12] Particle Data Group, "Particle Physics Booklet" (2002).

[13] M. Gell-Mann, Phys. Rev. 125, 1067 (1962).

[14] I.S. Hughes, Elementary Particles 2nd Edition [Cambridge University Press (1985)].

[15] R.G. Roberts, The Structure of the Proton - Deep-Inelastic Scattering, [Cambridge University Press (1990)].

[16] The Strong Interaction, from Hadrons to Partons, Proceedings of the XXIV SLAC Summer Institute on Particle Physics (1996).

[17] F. Halzen and A.D. Martin, Quarks and Leptons: An Introductory Course in Modern Particle Physics, Wiley (1984) 396.

[18] M. Breidenbach *et al.*, Phys. Rev. Lett. 23 (1969) 935;
J.I. Freidman and H.W. Kendall, Ann. Rev. Nucl. Part. Sci. 22 (1972) 203.

[19] C.G. Callan and D.Gross, Phys. Rev. Lett. 22, 156 (1969).

[20] A. Bodek *et al.*, Phys. Rev. D20, 1471 (1979).

[21] A. Manohar, Proceedings of the Tenth Lake Louise Winter Institute: Quarks and Colliders, (1995).

[22] O.W. Greenberg, Phys. Rev. Lett. 13 (1964) 598.

[23] J.C. Collins and D.E. Soper, Nucl. Phys. B 193 (1981) 381.

[24] D.E. Soper, Basics of QCD Perturbation Theory, SLAC-R-508 (1996).

[25] J.C. Collins, Renormalization [Cambridge University Press (1984)].

[26] P. Buckley and F.D. Peat, A Question of Physics [University of Toronto Press (1979)], 39.

[27] J.C. Sprott, Chaos and Time-Series Analysis, Oxford University Press (2003).

[28] T. Laštovička, Preprint DESY 02-036, DESY (2002).

[29] H.D. Politzer, Phys. Rev. Lett. 30 (1973) 1346;
D.J. Gross and F. Wilczek, Phys. Rev. Lett. 30 (1973) 1343;
W.A. Caswell, Phys. Rev. Lett. 33 (1974) 244.

[30] O.V. Tarasov, A.A. Vladirmirov and A.Yu. Zharkov, Phys. Lett. B 93 (1980) 429;
S.A. Larin and J.A.M. Vermaseren, Phys. Lett. B 303 (1993) 334;
T. van Ritbergen, J.A.M. Vermaseren and S.A. Larin, Phys. Lett. B 400 (1997) 379.

[31] R.P. Feynman, "Photon-Hadron Interactions" [Benjamin, NY (1972)];
K.H.Streng, T.F.Walsh, P.M. Zerwas, Z. Phys. C 2, 237 (1979).

[32] B.R. Webber, J. Phys. G19 (1993) 1567.

[33] S. Burke *et al*, Nuc. Instrum. Meth. A373, (1996) 227-260.

[34] J. Burger *et al*, Nuc. Instrum. Meth. A279 (1989) 217-222.

[35] J. Andruszków *et al.*, Preprint DESY-92-066, DESY (1992).

[36] B. Andrieu *et al*, Nuc. Instrum. Meth. A344 (1994) 492-506.

[37] H1 Collaboration, S. Aid *et al*, H1 Internal Report (1995).

[38] B. Heinemann, Dissertation, Fachbereich Physik der Universität Hamburg (1999)

[39] H1 Collaboration, C. Adloff *et al.* Eur. Phys. J. C13 (2000) 609

[40] S.D. Ellis and D.E. Soper, Phys. Rev. D 48 (1993) 3160;
S. Catani, Yu.L. Dokshitzer, M.H. Seymour and B.R. Webber, Nucl. Phys. B 406 (1993) 187.

[41] S. Frixione and G. Ridolfi, Nucl. Phys. B 507 (1997) 315.

[42] S. Catani and M.H. Seymour, Nucl. Phys. B 485 (1997) 291, Erratum-ibid. B 510 (1997) 503.

[43] C. Duprel, Th. Hadig, N. Kauer and M. Wobisch, Proceedings of the HERA Monte Carlo Workshop, eds. G. Grindhammer, G. Ingelman, H. Jung, T. Doyle, DESY-PROC-02-1999 (1999) 142.

[44] H. Jung, Comp. Phys. Comm. 86 (1995) 147.

[45] H. Jung, http://www-h1.desy.de/ jung/rapgap.html.

[46] G. Marchesini *et al.*, Comp. Phys. Comm. 67 (1992) 465.

[47] G. Ingelman, A. Edin and J. Rathsman, Comp Phys. Comm, 101 (1997) 108.

[48] L. Lönnblad, Comp. Phys. Comm. 71 (1992) 15.

[49] B. Andersson *et al.*, Phys. Rep 97 (1983) 31.

[50] K. Charchula, G. Schuler and H. Spiesberger, Comp. Phys. Comm. 81 (1994) 381.

[51] A. Kwiatkowski, H. Spiesberger and H-J. Möhring, Comp. Phys. Comm. 69, 155 (1992).

[52] T. Sjöstrand, Comp. Phys. Comm.82 (1994) 74.

[53] H1 Collaboration, I. Abt *et al.*, Nucl. Instr. Meth. A 386 (1997) 310 and 348.

[54] H1 Collaboration, C. Adloff *et al.*, Eur. Phys. J. C 13 (2000) 609.

[55] U. Bassler and G. Bernardi, Nucl. Instr. Meth. A 426 (1999) 583.

[56] T. Sjöstrand and M. Bengtsson, Comp. Phys. Comm. 43 (1987) 74.

[57] R. Engel and J. Ranft, Phys. Rev. D 54 (1996) 4244.

[58] CERN, GEANT, detector description and simulation tool, CERN Program Library Long Writeup W 5013 (1994).

[59] H1 Collaboration, C. Adloff *et al.*, Nucl. Phys. B 545 (1999) 3.

[60] Z. Nagy and Z. Trocsanyi, Phys. Rev. Lett. 87, 082001 (2001).

[61] H.L. Lai *et al.*, Phys. Rev. D. 55, 1280 (1997).

[62] D.E. Soper, Les Rencontres de Moriond, Les Arc, France (1997) hep-ph/9706320;
M.H. Seymour, Nucl. Phys. B 513 (1998) 269.

[63] N. Brown and W.J. Stirling, Z. Phys. C 53 629 (1992) 629.

[64] S. Bentvelsen, J. Engelen and P. Kooijman, Proceedings of the Workshop "Physics at HERA", vol. 1, DESY, (1991) 23.

[65] U. Bassler and G. Bernardi, Nuc. Instrum. Meth. A361 (1995) 197.

[66] U. Bassler and G. Bernardi, Nuc. Instrum. Meth. A426 (1998) 583.

[67] H1 Collaboration, C. Adloff *et al.*, hep-ex/9908059, DESY-99-107 (1999).

[68] C. Glasman, Precision Measurements of α_s at HERA, XIII International Workshop on Deep-Inelastic Scattering (2005).